

# Roll-to-Roll Advanced Materials Manufacturing DOE Laboratory Collaboration - FY 2018 Final Report

ORNL/SPR-2019/1066

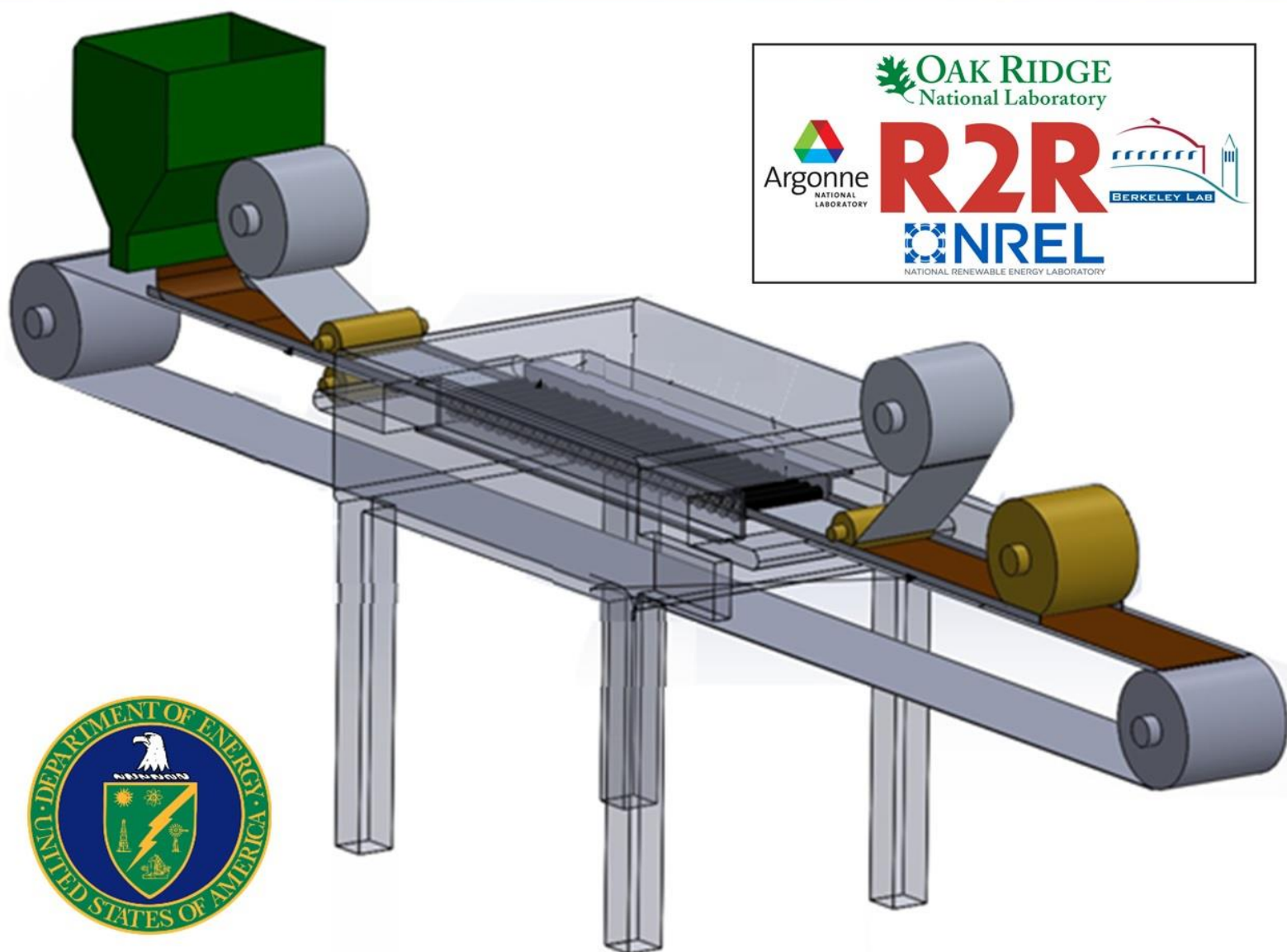
January 2019

Funding provided by:

U.S. Department of Energy

Office of Energy Efficiency and Renewable Energy

Advance Manufacturing Office



Approved for public release. Distribution is unlimited.

## Disclaimer

This report was prepared as an account of work sponsored by an agency of the United States government. Neither the United States government nor any agency thereof, nor any of their employees, makes any warranty, express or implied, or assumes any legal liability or responsibility for the accuracy, completeness, or usefulness of any information, apparatus, product, or process disclosed or represents that its use would not infringe privately owned rights. Reference herein to any specific commercial product, process, or service by trade name, trademark, manufacturer, or otherwise does not necessarily constitute or imply its endorsement, recommendation, or favoring by the United States government or any agency thereof. The views and opinions of authors expressed herein do not necessarily state or reflect those of the United States government or any agency thereof.

### DOCUMENT AVAILABILITY

Reports produced after January 1, 1996, are generally available free via US Department of Energy (DOE) SciTech Connect.

**Website** <http://www.osti.gov/scitech/>

Reports Produced before January 1, 1996, may be purchased by members of the public from the following source:

National Technical Information Service  
5285 Port Royal Road  
Springfield, VA 22161  
**Telephone** 703-605-6000 (1-800-553-6847)  
**TDD** 703-487-4639  
**Fax** 703-605-6900  
**E-mail** [info@ntis.gov](mailto:info@ntis.gov)  
**Website** <http://www.ntis.gov/help/ordermethods.aspx>

Reports are available to DOE employees, DOE contractors, Energy Technology Data Exchange representatives, and International Nuclear Information System representatives from the following source:

Office of Science and Technical Information  
PO Box 62  
Oak Ridge, TN 37831  
**Telephone** 865-576-8401  
**Fax** 865-576-5728  
**Email** [reports2osti.gov](mailto:reports2osti.gov)  
**Website** <http://www.osti.gov/contact.html>

## Foreword

Oak Ridge National Laboratory (ORNL), Argonne National Laboratory (ANL), Lawrence Berkeley National Laboratory (LBNL), and the National Renewable Energy Laboratory (NREL) in collaboration with Kodak's Eastman Business Park (EBP) formed Roll-to-Roll Advanced Materials Manufacturing (R2R AMM) Department of Energy (DOE) Laboratory Consortium in April 2016 to broadly disseminate materials, process science, and advanced technologies to industry in R2R manufacturing. This multi-laboratory and industry partnership enable advanced R2R manufacturing research and development to demonstrate a materials genomic approach to optimization of process parameters for finding new transformational improvements in manufacturing technologies enabling clean energy applications. The first project for demonstration was to develop a novel cathode material for lithium-ion battery (LIB) manufacturing followed by development of a matching anode. For fiscal year (FY) 2018, efforts completed for the cathode-anode matching, a continuous semi-automated assembly line for water membrane wafers, and computational modeling of functional materials synthesis with some efforts in fuel cell development transitioning. Three Cooperative Research and Development Agreement (CRADA) projects were also initiated. This consortium creates a critical team of national experts covering all needed aspects from materials synthesis modeling and simulation through materials development, slurry formulation, scale-up, pilot deposition, process development, non-destructive evaluation (NDE) during processing, big data analytics and validation to full scale production of rolled goods. These efforts will enable an order of magnitude shorter process development cycles bringing them from 20 years down to a few years with the pathway for initial commercialization within months of pilot scale demonstrations.

DOE cost targets for advanced energy storage and conversion applications will not be met without significant and timely advancements in R2R manufacturing. Required R2R advances include adaptation of existing processing methods and development of novel methods that have the potential to significantly impact U.S. manufacturing sector recovery, environmental security, energy security, and sustainable transportation adoption. Economies of scale through increased manufacturing volumes based on traditional assembly and processing methods will not suffice. For example, current baseline technology cell costs in the LIB industry are about 2.5× the \$100/kWh ultimate target of DOE Vehicle Technologies Office (VTO). [1] To increase the capacity from 250 Wh/kg to 1000 Wh/kg for anode materials, novel R2R processing technologies will be required. Furthermore, polymer electrolyte membrane fuel cell (PEMC) stacks currently cost almost 10× in low volumes compared to the ultimate cost of the DOE Fuel Cells Technology Office (FCTO) target of \$20/kW by the year 2020. [2] Water consumption for renewable energy technologies can be as high as a medium value 4,500 gallons/MWh and more than 44,000 gallons/MWh for non-renewable energy applications. [3] New technologies are needed to increase the capacity of these systems to meet future needs. Other examples of the Energy Efficiency and Renewable Energy (EERE) Office funded technologies that have a similar cost-target issue are chemical-process industry membranes, window films, photovoltaic (PV) films, and electronic films. The EERE Advanced Manufacturing Office (AMO) is poised to assist in reaching the low dollars per unit costs of these various critical energy related applications through addressing R2R manufacturing problems common to each application.

## Preface

The following report provides a description of the program structure and technical accomplishments made during FY 2018 to overcome challenges for expanding use of R2R technologies and processing for clean energy applications. The processing technologies developed will enable enhanced manufacturing of battery electrodes, fuel cells and water separation membranes that take advantage of advancements in new functional materials. Data mining, visualization, modeling and simulation for these layered materials, energy storage technologies and continuous manufacturing processes being developed allow for improvements in R2R manufacturing applications. This report documents the research conducted by four DOE national laboratories as a collaborative group with participation from industry partnerships. The approach is to develop advanced and novel materials, methods and techniques for multi-layer coatings and depositions that can be used for R2R processes that are applicable to enhancing the performance of renewable energy technologies and systems. This effort supports building the foundation of technologies, processes and a United States (U.S.) manufacturing base that will enable an order of magnitude in shorter process development cycles with the pathway for initial commercialization within months instead of years.



## Acknowledgements

First and foremost, the following scientists, investigators and technical support who are working diligently to realize their innovative ideas and technological developments in R2R processing and their desire to deploy them broadly for energy storage applications are acknowledged for their contributions:

**ANL:** Andrew Jansen, Gerald Jeka, Alison Dunlop, Steve Trask, Bryant Polzin, Phillip Ridley, Dennis Dees, Yupo Lin, Steve Barry, Deborah Myers, Jaehyung Park, Rajesh Ahluwalia, and C. Firat Cetinbas, Venkat Srinivasan, Pallab Barai, Albert Lipson, Donna Brunner

**ORNL:** *Structured Lithium-Ion Battery Anode and Cathode Tasks:* Marissa Wood, T. J. Christensen, Jianlin Li, Yangping Sheng, Zhijia Du; *Thickness Feedback Loop and Process Controls Task:* Alex Melin, Kofi Korsah, Yarom Polsky, Marissa Wood, T. J. Christensen; *Fuel Cell Gas Diffusion Electrode Coating Task:* Anand Parejiya, T. J. Christensen, Jianlin Li, Marissa Wood

**NREL:** Peter Rupnowski, Brian Green, Scott Mauger, KC Neyerlin, Ami Neyerlin, Sunil Khandavalli, Jason Pfeilsticker, Min Wang, Maikel van Hest, Bertrand Tremolet deVillers, Rob Tenent, Jason Woods

**LBNL:** Fuduo Ma, Dula Parkinson, Harold Barnard, David Trebotich, Steve Ferreira, Gerd Ceder, Vince Battaglia, Olga Kononova, Kenny Higa

**DOE EERE AMO:** David Hardy (Technical Project and Program Management)

We would like to acknowledge Matt Fronk and Daniel Ocorr at Kodak Eastman Business Park, Rochester, NY, for their participation in the R2R AMM DOE Laboratory Collaboration program and their insights for improving technologies and processes for R2R manufacturing. Their inputs were of great value to the DOE team for building a technical portfolio and defining R2R problems.

Finally, we would also like to acknowledge the contributions of Fred Crowson, Energetics, for his project management assistance and involvement in preparing and publishing this report.

The research at

- Oak Ridge National Laboratory, managed by UT Battelle, LLC for the U.S. Department of Energy, under contract DE-AC05-00OR22725
- Argonne National Laboratory, managed by University of Chicago Argonne, LLC for the U.S. Department of Energy, under contract DE-AC02-06CH11357
- Lawrence Berkeley National Laboratory, managed by University of California for the U.S. Department of Energy, under contract DE-AC02-05CH11231
- National Renewable Energy Laboratory, managed by Alliance for Sustainable Energy, LLC for the U.S. Department of Energy, under contract DE-AC36-08GO28308

was sponsored by EERE AMO (Rob Ivester and David Hardy).

## Acronyms and Abbreviations

(Definitions for terminology used in this report are in the Glossary section at the end of this report)

°C	degrees Centigrade
μm or μ	micrometers or microns
\$/kW	dollars per kilowatt
\$/m <sup>2</sup>	dollars per square meter
1C, 2C etc.	a charge current of 1, 2, etc. time the rated capacity
A	amp
A/cm <sup>2</sup>	amps per centimeter squared
Ah	amp-hour
AMM	Advanced Materials Manufacturing
AMO	Advanced Manufacturing Office
ANL	Argonne National Laboratory
APS	Advanced Photon Source
C	chemical symbol for carbon
CA	California
CB	carbon black
CCL	cathode catalyst layer
CCM	catalyst-coated membrane
cm <sup>2</sup>	centimeter squared
Co	chemical symbol for cobalt
CO	Colorado
CRADA	Cooperative Research and Development Agreement
CSTR	continuous stirred tank reactor
CT	computed tomography
CV	cyclic voltammetry
D10, D50, D90	the value of the particle diameter at 10%, 50% and 90% in the cumulative distribution for a group of particles
D <sub>f</sub>	fractal dimension
DARVAN C-N	an ammonium polymethacrylate solution used mainly in the electronic and specialty ceramics fields low foaming that produces slurries with unusually low viscosity
DC	District of Columbia
DOE	U.S. Department of Energy (when referring to the agency)
DOE	diffractive optical element (when referring to laser scribing)
DOL	diffractive optics-based laser
DP	dual pass; to process a coating on one side of a substrate on a single pass through a process and then coat the substrate on the back side of the substrate in a second pass
EBP	Eastman Business Park
EC:EMC	ethylene carbonate (EC)–ethyl methyl carbonate (EMC) electrolyte
ECS	Electrochemical Society
EERE	Energy Efficiency and Renewable Energy
e.g.	abbreviation meaning “for example”; a Latin phrase, “exempli gratia” meaning “for the sake of example”
EIS	electrochemical impedance spectroscopy
etc.	abbreviation for the Latin phrase “et cetera” which means “and so forth”

F1	in statistical analysis of binary classification, the F1 score (also F-score or F-measure) is a measure of a test's accuracy and considers both the precision and the recall of the test to compute the score.
FCTO	Fuel Cell Technologies Office
FTIR	Fourier transform infrared
FY	fiscal year
g	gram or grams
G'	storage modulus
G''	loss modulus
GDE	gas diffusion electrode
GDL	gas diffusion layer
gpm	gallons per minute
h or hr	hour
H <sub>2</sub> O <sub>2</sub>	hydrogen peroxide
Hg	chemical symbol mercury
HPPC	hybrid pulse-power capability (or characterization)
HSC	high surface carbon
I/C or I:C	ionomer-to-carbon ratio
IL	Illinois
InSb	indium antimonide
IR	infrared
IRS	ionomer-rich surface
kg	kilogram
kW	kilowatt
kWh	kilowatt hour(s)
kWh/m <sup>3</sup>	kilowatt hours per cubic meter
L	polymer brush length when referring to slurry mixtures
LBNL	Lawrence Berkeley National Laboratory
Li	chemical symbol for lithium
LIB	lithium-ion battery
LLZO	Li <sub>7</sub> La <sub>3</sub> Zr <sub>2</sub> O <sub>12</sub> , a promising solid electrolyte for Li-based batteries due to its high Li-ion conductivity and chemical stability with respect to lithium
LSTM	long short-term memory
M	molar
mAh	milliamp-hour
mAh/cm <sup>2</sup>	milliamp-hour per square centimeter
mAh/g	milliamp-hour per gram
MEA	membrane electrode assembly
MERF	Materials Engineering Research Facility
mg/cm <sup>2</sup>	milligram per square centimeter
min(s)	minute(s)
mm	millimeters
Mn	chemical symbol for manganese
MPL	microporous layer
MW	molecular weight
MWh	megawatt-hour
NCM or NMC	nickel-manganese-cobalt
NDE	non-destructive evaluation
Ni	chemical symbol for nickel

nm	nanometer
NMC	nickel-manganese-cobalt
NMP	N-Methyl-2-pyrrolidone
NREL	National Renewable Energy Laboratory
ORNL	Oak Ridge National Laboratory
PEM	polymer electrolyte membrane
PEMFC	polymer electrolyte membrane fuel cell
pH	the negative logarithm of the effective hydrogen-ion concentration or hydrogen-ion activity in gram equivalents per liter of the solution
Pt	chemical symbol for platinum
PV	photovoltaic
PVDF	polyvinylidene fluoride
QC	quality control
R&D	research and development
R2R	roll-to-roll
RW-EDI	resin wafer electro-deionization
s	second(s)
SAAL	semi-automated assembly line
SAXS	small-angle x-ray scattering
SEM	scanning electron microscope (or microscopy)
SLC	designation by Superior Graphite for a natural graphite surface treated with an amorphous carbon coating
SP	single pass
STEM	scanning transmission electron microscopy
TEM	transmission electron microscopy
TGA	thermogravimetric analysis
TN	Tennessee
TODA	TODA America, Inc.
U.S.	United States
USAXS	ultra-small angle x-ray scattering
V	volt
Vu	Vulcan
vs.	versus
VTO	Vehicle Technologies Office
WAXS	wide-angle x-ray scattering
Wh/kg	watt-hour per kilogram
wt%	percent by weight
XCT	x-ray computed tomography
XPS	x-ray photoelectron spectroscopy

# Table of Contents

Disclaimer.....	i
Foreword.....	ii
Preface.....	iii
Acknowledgements.....	iv
Acronyms and Abbreviations.....	v
Table of Contents.....	viii
List of Figures.....	x
List of Tables.....	xv
Executive Summary.....	1
Accomplishments.....	2
Technology Assessment.....	5
Roll-to-Roll Advanced Materials Manufacturing DOE Laboratory Consortium Project.....	7
Consortium Contacts.....	7
Annual Operating Plan Title and Corporate Planning System (CPS) Agreement Numbers.....	8
Project Introduction.....	9
Objectives.....	9
Approach.....	9
Core Program.....	9
FY 2019 Plans.....	11
Technology Transfer Paths.....	12
Results.....	12
Structured Anode Study.....	12
Argonne National Laboratory.....	13
Oak Ridge National Laboratory.....	19
National Renewable Energy Laboratory.....	26
Fuel Cell Study.....	28
National Renewable Energy Laboratory.....	28
Argonne National Laboratory.....	37
Oak Ridge National Laboratory.....	48



Modeling and Simulation.....	58
R2R Functional Materials.....	64
R2R Water Project.....	71
Collaboration/Coordination/Outreach/CRADA Projects.....	82
Core Program.....	82
CRADA Projects.....	83
Fisker, Inc.....	83
Navitas Systems, LLC.....	91
SolarWindow Technologies, Inc.....	98
Proton Onsite.....	101
Workforce Development/Educational Outreach.....	101
Challenges/Contingencies.....	101
Risks and Risk Handling/Project.....	102
Project Ratings.....	102
Conclusions.....	104
Key Publications.....	105
References.....	106
Glossary.....	107

## List of Figures

Figure 1. (a) Micrograph of the pristine anodes fabricated at ANL and (b) structured combinations made at ORNL.....	13
Figure 2. Discharge capacity in mAh of cathode active material from representative coin cells of FY 2018 cell sets.....	16
Figure 3. Glove box photo of the negative electrode from a coin cell set. Source: ANL.....	17
Figure 4. Post-test analysis (a) Particles present on the anode surface and (b) Optical image of anode electrode delamination.....	18
Figure 5. Cathode and anode compositions for pouch cell testing.....	19
Figure 6. Comparison of the discharge rate performance of single-layer pouch cells made with the best and worst anode/cathode combinations.....	20
Figure 7. Comparison of the discharge rate performance of single-layer pouch cells made with the following two-layer anode and cathode configurations or small particles on bottom/large particles on top (represented by the yellow lines) and large particles on bottom/small particles on top (represented by the blue lines): (a) all cells with two-layer anodes and (b) all cells with two-layer cathodes.....	21
Figure 8. Structured cathode/anode combinations chosen for pouch cell cycle life testing.....	22
Figure 9. Cycle life performance of single-layer pouch cells made with selected anode/cathode combinations. Charge C/2, discharge 2C for (a) 1000 cycles and (b) last 100 cycles shown for clarity.....	24
Figure 10. Cycle life performance of single-layer pouch cells made with selected anode/cathode combinations at a charge C/2 and discharge C/2.....	26
Figure 11. Emissivity measurements for cathode and anode made via FTIR, showing fairly constant emissivity within the spectral ranges of the two IR cameras (InSb in the mid-IR range and microbolometer in the far-IR range).....	27
Figure 12. Thermal response from structured anodes using the microbolometer camera showing a dependence on the particle size in the top layer of the electrode.....	27
Figure 13. Diffuse reflectance intensity signal for battery cathode samples fabricated at ORNL showing confounded dependence on date of coating and size of particles on top surface of coating.....	28
Figure 14. Sonication results: (a) MEA mass activity for tip+bath and bath-only sonicated inks, (b) H <sub>2</sub> /air polarization for tip+bath MEAs and c) bath-only MEAs.....	30
Figure 15. Effects of sonication on (a) non-Fickian oxygen transport resistance and (b) EIS of MEAs made with electrode inks of various sonication.....	31
Figure 16. Electron microscopy for (a) the 10s tip + 20 min bath case and (b) the 1 min bath case.....	31
Figure 17. Rheology of water-alcohol blends.....	32
Figure 18. Kelvin probe measurements of selected GDE samples. 8A: 1,2-butanediol-water, alcohol rich; 8B: 1,2-butanediol-water, water rich; 9A 1,2-pentanediol-water, alcohol rich; 8B: 1,2-pentanediol-water, water rich.....	33

Figure 19. In situ mass activity measurements for 1,2-pentanediol-water mixtures of different ratio.....	33
Figure 20. Kelvin Probe measurements of four R2R-coated GDEs for contact potential difference (CPD) versus the ionomer to carbon (I:C) ratio.....	34
Figure 21. Kelvin Probe calibration data for three catalyst systems showing similar slope but different intercept for each catalyst.....	34
Figure 22. In situ testing results of fabricated MEAs with R2R-coated GDEs: (a) hydrogen/air polarization curves and (b) mass activity as a function of catalyst layer protonic resistance.....	35
Figure 23. R2R-coated GDEs: (a) mass activity and (b) specific activity (high current density) as a function of contact potential difference compared to the sprayed baseline (using the same legend as shown in Figure 22 (a)).....	35
Figure 24. Polarization curves comparing MEAs fabricated from R2R-coated IRS GDEs on diffusion media with differing MPL roughness (note that GDEs on H23C8 diffusion media with 1 and 2 loops of overspray had identical performance).....	37
Figure 25. USAXS-SAXS scattering of (a) Vu and (b) HSC-based inks plotted on log-log scales. The intensity data sets have been offset to overlap at $q=0.02 \text{ \AA}^{-1}$ on the y-axis for clarity.....	38
Figure 26. USAXS profiles for catalyst (a) Pt/Vu and (b) Pt/HSC-ionomer-solvent inks with the Turrax mixer as a function of homogenization time.....	40
Figure 27. USAXS profiles for Pt/Vu-ionomer-solvent inks as a function of sonication time for (a) horn, (b) horn/bath and (c) bath sonication methods.....	41
Figure 28. WAXS profiles for Pt/Vu-ionomer-solvent inks as a function of sonication time for (a) horn, (b) horn/bath and (c) bath sonication methods.....	42
Figure 29. Scattering intensity in (a) aggregate, (b) agglomerate, and (c) wide-angle scattering regions for Pt/Vu as a function of sonication step.....	43
Figure 30. Analysis of GDEs for (a) pore size and solid size distributions of three NREL GDEs with I:C ratios of 1.6, 1.2, 0.9, with (b) the shortest path tortuosity of the GDEs, and for (c) ionomer volume fraction through the thickness of the GDEs (0 thickness is at the membrane interface and 1 is at the GDL interface).....	45
Figure 31. Reconstruction of the electrode layers with different solvent content.....	45
Figure 32. Ionomer distribution of the electrode layers with different solvent content.....	46
Figure 33. Tomography data for (a) agglomerate size distribution and (b) pore size distribution of electrode layers dried at different temperatures.....	46
Figure 34. Ionomer distribution of the electrode layers with different drying temperature.....	47
Figure 35. Reconstruction of the nano-CT data for electrode layers with different I:C ratios of (a) 1.6 and (b) 0.9 and different solvent evaporation temperatures of (a) 80°C and (b) room temperature.....	47
Figure 36. Effect of CCL-membrane contact area.....	48
Figure 37. Nafion (D2020 dispersion)/CB Vu XC-72R coating on SGL Group GDL 29BC substrate: (a) wet and (b) dry.....	50
Figure 38. Analysis of the linear viscosity region using a rheometer.....	51

Figure 39. Shear thinning behavior of the baseline slurry.....	51
Figure 40. Analytical data for (a) the effect of pre-shear time and (b) the resting time for the slurry to regain its initial structure.....	52
Figure 41. Shear thinning behavior of slurries for (a) 4.8% solids loading, (b) 9.1% solids loading and (c) comparing the three solid loadings.....	53
Figure 42. Agglomerate size analysis by Hegman gauge.....	54
Figure 43. Shear thinning behavior of inks with varying solid loading.....	55
Figure 44. Effect of ink composition on (a) storage and loss modulus and (b) $\tan \delta$ as a function of solid loadings.....	55
Figure 45. Ink coatings on GDL at various doctor blade heights.....	56
Figure 46. Agglomerate size analysis using a Hegman gauge for constant solvent and different solids loading .....	57
Figure 47. Effect of solvent proportion on shear thinning of inks for (a) constant 1-propanol and (b) increased solids loading.....	57
Figure 48. Effect of solvent proportion on storage and loss modulus of inks (a) without and (b) with constant 1-propanol.....	58
Figure 49. Experimental and modeling rheology of carbon black slurries with polymer binders of different molecular weights: (a) KF9300 (MW: 1 million), (b) KF1700 (MW: 0.5 million), and (c) KF1100 (MW: 0.28 million).....	59
Figure 50. Proposed assembly structures for CB with polymers of different molecular weights (a) as $D_f$ increases and (b) the relationship of increased viscosity with decreasing $D_f$ .....	59
Figure 51. Optical and SEM images of dried CB particles with PVDF of three binders with different molecular weights.....	60
Figure 52. Modeling results of anode slurries with polymer binders of different molecular weights: (a) KF9300, (b) KF1700 and (c) KF1100.....	60
Figure 53. Material effects for (a) steady-state viscosity data and model predictions and (b) diagram of whole anode slurry organization with the SEM image of the anode material.....	61
Figure 54. Fits of selected mathematical forms to fuel cell ink viscosity data for (a) high viscosity and (b) low viscosity inks.....	62
Figure 55. Least-squares fits of battery model form to fuel cell ink data (provided by NREL), showing poor agreement at higher shear rates and suggesting that hydrodynamic sub-model should be revised.....	62
Figure 56. Schematic representation of the algorithm based on bi-directional recurrent neural network with LSTM units to classify materials entries in synthesis paragraphs.....	63
Figure 57. (a) Variation in secondary particle diameter with ammonia content within the reacting solution and (b) decrease in secondary particle size with increasing solution pH.....	65
Figure 58. Phase map between solution pH and ammonia content showing the average particle sizes and their first standard deviation under the assumption of Gaussian particle size distributions.....	66

Figure 59. Area of the diffraction peaks obtained by analyzing the WAXS data during operation at pH 10.6 (solid symbols) and 11.4 (open symbols).....	67
Figure 60. (a) Growth of primary particles with time and SEM image of the coprecipitated particles are shown as inset. (b) Evolution of secondary particles with time.....	67
Figure 61. Evolution of secondary particle morphology with time (a) without the movement of secondary particle aggregates and (b) incorporating the movement of secondary particle.....	69
Figure 62. Variation in secondary particle diameter with increasing surface charge strength of the primary particles.....	69
Figure 63. Breakage of secondary particles within the aggregation model. (a) Presence of large and small eddies in a turbulent flow. (b) Modeling particle rupture under the influence of fluid shear induced force. (c) Phase map between particle length and aspect ratio demonstrating the stability limit beyond which the breakage of secondary particles should occur under a stirring speed of 1000rpm. (d) Comparison between the particle size with and without rupture.....	70
Figure 64. Coalescence of two particles as predicted by the phase-field based sintering model. (a) Initial (top) and final (bottom) shapes of the two adjacent particles as obtained after sintering with low (left-bottom) and high (right-bottom) diffusivity. (b) Decrease in size of the smaller particle with respect to time.....	71
Figure 65. (a) Industrial blender equipment and (b) the particle mixtures from a laboratory blender and the industrial blender.....	72
Figure 66. (a) IR oven and (b) the temperature profile measured in the oven.....	73
Figure 67. (a) Resin wafers fabricated using the IR oven and (b) the ionic conductivity for different processes .....	73
Figure 68. Schematic of the components for the SAAL design.....	74
Figure 69. (a) Aligned equipment comprising the SAAL and (b) location of the IR oven.....	74
Figure 70. Various stages (a) through (h) of the operational testing of the individual components of the SAAL.....	76
Figure 71. (a) A resin wafer made using the SAAL and (b) the characterization system to determine ionic conductivity of the wafer material.....	76
Figure 72. Specific conductivity for SAAL wafers compared to the benchmark wafer made with a hot-pressed method.....	77
Figure 73. (a) Wafer made with an ionomer binder, (b) same wafer soaking in water and (c) wafer disintegrated .....	78
Figure 74. The resin wafer made with ionomer-bound resin beads (a) dry and (b) wet.....	78
Figure 75. The ionic conductivity of a resin wafer made from a sulfonated poly-ether ether ketone.....	79
Figure 76. Conceptual design of a fully automatic assembly line for R2R manufacture of resin wafers.....	79
Figure 77. Comparison of manufacturing time and labor cost needed to manufacture resin wafer material for a small-scale cooling water system.....	81
Figure 78. Comparison of manufacture time and labor cost needed to manufacture resin wafer material for a large-scale cooling water system.....	81



Figure 79. Comparison of cost of operation to produce resin wafer material.....	82
Figure 80. (a) Typical LLZO green tape. (b) SEM fracture surface image of sintered LLZO film.....	83
Figure 81. (a) Freeze tape cast 7.5 vol.% LLZO slurry. (b) Freeze tape cast 10 vol.% LLZO slurry. (c) Top surface (top) and bottom surface (bottom) of freeze tape cast 10 vol.% LLZO slurry . ....	84
Figure 82. Two SEM fracture surface images (a) with low magnification and (b) high magnification of NMC622/carbon black/PVDF infiltrated dense/porous LLZO bilayer.....	85
Figure 83. Rate performance of the hybrid coin cell.....	86
Figure 84. Cycle life test of the hybrid coin cell.....	86
Figure 85. Voltage profiles.....	87
Figure 86. EIS profiles.....	87
Figure 87. Morphology of a proprietary Li foil stored in a dry room at time intervals up to 240 mins.....	88
Figure 88. Steps 1 through 3 shows cathode slurry infiltration into porous LLZO scaffolds via drop casting. Steps 4 and 5 shows attachment of the aluminum current collector. Step 6 is final assembly after drying.....	89
Figure 89. Rate performance of a hybrid pouch cell cycled between 2.5 – 4.35 V with a 2 hour hold at upper cut-off voltage.....	89
Figure 90. Photographs of the hybrid pouch cell components after the rate performance test. (a-c) show the cycled cathode-LLZO assembly, and (d-f) show the cycled proprietary Li foil.....	90
Figure 91. Rate performance of a coin cell containing a cycled cathode-LLZO piece, paired with a fresh regular Li metal disc, fresh liquid electrolyte and a Celgard separator.....	90
Figure 92. Cyclic voltammetry curves of NMC 622 half coin cells with various separators: (a) and (b) Celgard 2325, (c) and (d) Entek and (e) Teijin.....	92
Figure 93. Rate performance of a coin cell containing a cycled cathode-LLZO piece, paired with a fresh regular Li metal disc, fresh liquid electrolyte and a Celgard separator.....	93
Figure 94. SEM images of (a) Entek and (b)Teijin separators.....	93
Figure 95. SEM images of (a) Entek and (b)Teijin separators.....	94
Figure 96. XPS results for (a) Teijin and (b) Entek separators.....	95
Figure 97. Energy-dispersive x-ray spectroscopy results on the powder left from TGA experiments to determine ceramic composition for (a) Entek and (b) Teijin.....	96
Figure 98. Binder was determined to be PVDF by FTIR.....	96
Figure 99. Contact angles (a) with water and (b) with Gen II electrolyte for Entek and Teijin.....	97
Figure 100. Electrolyte uptake of EnTek and Teijin separators with Gen II electrolyte and one-hour exposure .....	98
Figure 101. Figure 101. Dimension changes of the separators over temperatures for (a) Entek-Teijin comparison and (b) Teijin at 160°C.....	98
Figure 102. NREL R2R metrology line with planned location for the laser system.....	99

## List of Tables

Table I. R2R AMM Coin Cell Testing Matrix.....	14
Table II. Capacities for Cell Sets Developed in FY 2017.....	15
Table III. Number of Cycles to Average 80% Discharge Capacity Retention.....	17
Table IV. Cells Chosen for Post-Test Analysis.....	18
Table V. Comparison of ORNL Single-Layer Pouch Cell Rate Performance Results and ANL Coin Cell, Cycle Life Test Results.....	23
Table VI. Comparison of Cycle Life and Rate Performance Results for the 16 Selected Anode/Cathode Combinations.....	25
Table VII. Summary of In Situ Data Exploring Tip and Bath Sonication Impact on MEA Performance.....	30
Table VIII. Calculated Non-Fickian O <sub>2</sub> Transport Resistance in R2R-Coated GDEs.....	36
Table IX. Power-Law Fitting of Slopes of USAXS Data in the Low Q Region ( $<0.002 \text{ \AA}^{-1}$ ).....	39
Table X. CB/Water Ink Quality at Nine Different Solids Loadings of CB with Constant Mixing Speed of 3500 rpm .....	49
Table XI. Improvement in GDE Ink Quality at 7 wt% Solids Loading with the Addition of Nafion D2020 Dispersion Containing 1-Propanol. I:C is 0.9 and Nafion D2020 Contained 20 wt% Ionomer.....	49
Table XII. Preliminary Slurry Formulations.....	52
Table XIII. Nafion D2020 Composition.....	53
Table XIV. Results of Slurry Coatings with a Doctor Blade on the GDL.....	54
Table XV. Compositions of Ink Formulations Investigated for Effect on Viscosity.....	56
Table XVI. Steps in Synthesis Process and Accuracy of Data Mined.....	64
Table XVII. Comparison of Different Optical Approaches for Beam Splitting.....	100
Table XVIII. R2R AMM Laboratory Consortium Project Ratings.....	103

(This page intentionally left blank)

## Executive Summary

High-value R2R processing is used to support a wide range of products in applications which span many industrial business sectors. The overall R2R process technology can be considered as “mature” as the process methodology and has been in use for decades. This continuous processing technique traditionally involves deposition of material(s) onto moving webs or carriers or other continuous R2R, belt-fed, or conveyor-based processes that enable successive steps to build a final version which serves to support the deposited materials. Current process technologies, which typify “roll to roll”, include tape casting, silk-screen printing, reel-to-reel vacuum deposition/coating and R2R lithography. Products supported by R2R manufacturing include micro-electronics, electro-chromic window films, PVs, fuel cells for energy conversion, battery electrodes for energy storage, and barrier materials. Due to innovation in materials and process equipment, high-quality yet very low-cost multi-layer technologies can be manufactured on a very cost-competitive basis. To move energy-related products from high-cost niche applications to the commercial sector, a means must be available to enable manufacture of these products in a cost-competitive manner that is affordable by the general consumer. Fortunately, products such as fuel cells, thin- and mid-film PVs, batteries, electrochromic and piezoelectric films, water separation membranes, and other energy saving technologies readily lend themselves to manufacture using R2R approaches.

Within the DOE EERE AMO, it was recognized that establishment of a program supported at the DOE National Laboratories, along with their immense design of materials and equipment modelling capabilities enabled with use of high-performance computing, could take advantage of available R2R infrastructure to manufacture new technologies. In FY 2016, a R2R Consortium was established and provided with initial “seed” funding to take an approach that was envisioned to be supportable by advanced manufacturing R2R processes. This collaborative approach was designed to foster identification and development of materials and processes related to R2R for clean-energy product development. Using computational and experimental capabilities by acknowledged subject matter experts within the supported National Laboratory system, this collaborative project would leverage the capabilities and expertise at each of four laboratories to further the development of an enabling high-volume cost-competitive platform technology.

The collaboration team that is comprised of ORNL, ANL, NREL and LBNL, coordinating with EPB and other selected industry partners, was formed in April 2016 to initially address enhancing battery electrode performance and R2R manufacturing challenges. The research efforts were to predict and measure changes and results in electrode morphology and performance based on process condition changes; to evaluate mixed, active, particle size deposition and drying for novel electrode materials; to model various process condition changes and the resulting morphology and electrode performance; and to develop and validate NDE techniques for in-line measurement of battery electrode material properties. These efforts carried through FY 2017 and completed at the end of FY 2018.

The approach was to look at compositions of materials with different particle sizes to make electrode samples using a R2R manufacturing process. The shape, size, and morphology of the materials, the chemistry of the formulation, the nature of slurries, their coating rate, the rate of drying all play a role in determining the final coating architecture, quality, and performance. A commercial cathode material was selected to make a series of cathodes and anodes by single pass, dual pass and slot die methods. Analysis of all the compiled results for this battery electrode development were that the best performing cathodes included: dual-pass electrode with large particles near the foil, mixed small and large particles, and small particles only. Whereas, the best performing anodes were with a mix of small and large graphite particles.

An additional core project was added in FY 2017 to conduct studies of fuel cell materials that can be produced using R2R processes. The goal of this project is to explore, understand and optimize material and process parameters to support increased throughput, increased quality, and reduced cost for high volume production of gas-diffusion electrodes (GDEs) for PEMFCs. Project work in FY 2018 were to use a R2R process to fabricate electrodes without ionomer overlayer that can produce the equivalent mass activity as spray-coated electrodes

with an ionomer overlayer. Oxygen-limiting current measurements were utilized to optimize oxygen mass transport. Alcohol-rich solvents were investigated, and results were that the alcohol and water ratio can be tuned to control ionomer distribution. Water-rich solvents produce a more dispersed ink which results in better high-current density performance.

Two other projects for AMM Functional Materials and the R2R Water Project were added to the R2R portfolio in FY 2017 and completed in FY 2018. The AMM Functional Materials effort aims to enable advanced materials process research and development (R&D), scaleup and synthesis of next generation functional materials; develop several materials, processes, software tools and techniques that support and are potentially compatible with continuous manufacturing process technologies over a range of functional energy-related materials; prototype, characterize and develop a material properties database suitable to support related materials design; and provide uniform, baseline materials to industry for validation and to researchers for further development. Findings for functional materials were that the performance of LIB cathode materials depends significantly on the particle morphology, which is usually determined by the synthesis conditions. By combining experiments with computational models, a detailed framework has been developed that can minimize the cost associated with trials required for optimizing LIB cathode synthesis conditions. The objectives for the R2R Water Project were to remove the material manufacturing hurdle for water membrane materials, evaluate the manufacturing tools to improve material properties for energy and cost savings, and demonstrate the application of advanced manufacturing technology to improve water treatment efficiency and processing cost through development and installation of a semi-automated assembly system. Resin wafer technology is capable of providing greater than 35 % energy efficiency for water desalination compared to 15 % for the current state-of-the-art technologies. Resin wafer electro-deionization (RW-EDI) technology was demonstrated for this project using a prototype continuous process line. Scaling up this process is expected to result in the potential to improve separation energy efficiency and material manufacturing costs (95% for labor and 90% production time) for multiple industrial sectors.

The FY 2018 collaborative effort successfully completed all tasks to develop an enhanced battery material using a R2R manufacturing process and to provide modeling, simulation, processing, and manufacturing techniques that demonstrate the feasibility and potential for scale-up. Technology transfer for these and other technologies applicable to R2R manufacturing was initiated collaboration with industry partners and through the initiation of three CRADA projects with industry. This DOE-industry partnership will result in low manufacturing costs, low energy processes, high volume production, high throughput due to improved materials, and compatibility with many material platforms.

## **Accomplishments**

### **Collaboration and Outreach**

The R2R AMM DOE Laboratory team participated in bi-monthly review meetings with DOE AMO and FCTO Program Managers to ensure information for each project was available on a continuous and regular basis. Team members also presented at the Association of International Metallizers, Coaters and Laminators, TechConnect World Innovation Conference, the 2018 DOE Hydrogen and Fuel Cells Program and Vehicle Technologies Office Annual Merit Review and Peer Evaluation Meeting, the 2018 AMO Peer Review, the 2018 ASME Power and Energy Conference and Exhibition, the 19th International Coating Science and Technology Symposium, Beyond Lithium-Ion XI Symposium, and the Electro Chemical Society 2018 Spring Meeting. As a team, they initiated three CRADA projects that demonstrate all-solid-state batteries based on  $\text{Li}_7\text{La}_3\text{Zr}_2\text{O}_{12}$  (LLZO) separators and cathode scaffolds that will allow scaling a freeze casting process to the pilot level, R2R production of an advanced separator for LIBs, and diffractive multiplexing for high-throughput R2R laser patterning of flexible organic PV modules. A fourth CRADA project to research R2R manufacturing of advanced (low loading, direct coated onto membrane) electrolysis electrodes for low-cost hydrogen production remained in the approval process at the end of FY 2018.



## Structured Anode Study

Experiments and testing by ORNL and ANL achieved a significant improvement for rate capacity, power density, and energy density when structuring both the LIB anode and cathode. When a simple particle-size modification was made and combined with a thick bilayer approach, with an emphasis on materials processing and coating deposition methodology (dual slot-die and dual-pass), substantial improvements were realized in rated capacity at the higher discharge rates. The best long-term performer was a mixed particle cathode with a dual-pass, small-particle bottom layer. The worst performer was the all-large particle cathode paired with a single-pass, large-particle bottom layer. Findings for this technology will enable further development of simultaneous high energy and power density electrodes.

NREL and ORNL jointly developed and demonstrated a real-time in-line measurement for battery electrode porosity. This technique enables critical quality inspection for high performance battery electrode manufacturing. This joint effort also created and validated a transient heat transfer model of the electrode layer that linked porosity with thermal measurement. The model was used to validate measurements on cathodes coated on the ORNL R2R coating line.

## Fuel Cell Study

The NREL-led study confirmed that R2R electrodes show the same trends and achieved equivalent mass activity as electrodes coated onto separate transfer liners and then hot-pressed onto the membrane or directly coated onto the membrane. R2R-fabricated electrodes without an ionomer overlayer produced equivalent mass activity to spray-coated electrodes with ionomer overlayer. Oxygen-limiting current measurements were utilized to further optimize oxygen mass transport. These efforts can be used to further optimize a continuous process for fabrication of multi-layer electrochemical media that has fuel cell application.

ANL x-ray scattering and tomography experiments provided support to NREL in developing catalyst-ionomer-solvent ink compositions and processing techniques for efficient R2R fabrication of GDEs. X-ray scattering was used to study the catalyst-ionomer ink agglomerate-aggregate structure as a function of ionomer content, ink solvent, and ink mixing procedure and time. X-ray tomography i.e., nano-computed tomography (CT) was used to visualize electrode structure and to quantify particle size and pore size distributions, thickness-dependent ionomer distribution, tortuosity, and effective transport properties. The optimum solvent and mixing procedures facilitate break-up of the catalyst support agglomerates into aggregates in the minimum amount of time and with the minimum input of energy while also not dislodging the catalyst nanoparticles from the carbon support. The optimum solvent and mixing procedures also result in an electrode microstructure forming an ionomer-rich layer at the electrode-air interface of the GDE while also having a uniform dispersion of catalyst/carbon, ionomer, and pores throughout the thickness of the electrode. The x-ray scattering results showed that inks with higher water content versus alcohol content lead to greater break-up of agglomerates and that 10 minutes of bath sonication is sufficient to reach the steady-state ink structure. The nano-CT studies showed that solvent has a strong influence on ionomer distribution, with less of an effect on porosity. The water-rich inks resulted in electrodes with a uniform distribution of ionomer through the thickness of the electrode, while the alcohol-rich inks resulted in high volume fractions of ionomer at the membrane and gas diffusion layer (GDL) interfaces. These studies also showed that drying temperature has a strong influence on porosity, but less influence on ionomer distribution. These results guided the NREL-led effort in GDE fabrication to achieve performance comparable to that of catalyst-coated membrane (CCM) electrodes.

## Modeling, Simulation and Data Mining

The LBNL core project continued to focus on the modeling and simulation of electrode materials and data mining of material properties from the open literature for predictive synthesis of new materials. LBNL developed a physics model based on colloidal interactions and this model will be improved for predicting the rheological properties of slurries for electrode materials. Major interactions between particles, such as Van der

Waals, electrostatic, and polymer steric interactions were included for calculating the viscosities. LBNL continued to investigate the properties of slurries, including particle size and zeta potential, particle and polymer mass ratio, and particle volume fractions. The current model well predicts the viscosities of anode slurries and will be modified for other materials including fuel cell materials.

A machine learning algorithm was implemented to identify potential targets and precursors of a synthesis route. The current accuracy estimated by calculation F1 score is: for materials F1 = 84%, for targets F1 = 83%, for precursors F1 = 84%. A Materials Entity Recognition algorithm was also developed and implemented to identify materials mentions in synthesis paragraphs and classify which materials are mentioned in context of starting compounds (precursors) and final products (targets) of the synthesis. The accuracy of the algorithm is ~90%. In significant number of paragraphs, target names are given in the form of an abbreviation, yet other significant fraction of target names contain off-stoichiometric variables. A third algorithm was implemented which obtains sequence of synthesis step from the synthesis paragraphs. The algorithm utilizes a feedforward neural network combined with a grammatical parser to traverse each sentence in the paragraph word by word and classifies them according to the following categories: not operation, start of synthesis, heating operation, mixing operation, drying operation, shaping operation and quenching operation.

## **Functional Materials**

ANL researchers demonstrated the first-known studies for tracking, in situ, particle growth during synthesis and developed the first known model that links process conditions to growth morphology. Control of morphology during particle synthesis is rooted in empirical trial-and-error. This project demonstrated that a science-based approach can be developed to predict the morphology of the particle when changing process conditions. By developing in situ synchrotron-based methods to “watch” growth and combining them with growth models, this project brings science to empiricism and accelerates the time to develop new process conditions.

## **R2R Water Project**

The ANL R2R Water Project completed the design and fabrication of a semi-automated assembly line (SAAL) to demonstrate a continuous process for the manufacture of a resin wafer to be used in industrial separations and desalination applications. The RW-EDI technology will provide a higher capacity and be more energy efficient than current processes and materials for water treatment. The assembly line is designed to increase the fabrication rate by 10x and incorporates industrial equipment which will significantly reduce the curing time by 60x for resin wafer fabrication. Application of this advanced manufacturing technology has the potential to improve separation energy efficiency and material manufacturing costs (95% for labor and 90% production time) for multiple industrial sectors. A new synthesis method of resin wafer has been developed that can reduce several unit operation steps using the SAL. A conceptual design of a full R2R manufacturing assembly line was completed based on the new synthesis method that can further reduce the manufacturing costs and production time.

## **CRADA Projects**

Three CRADA projects were initiated mid-FY 2018. A project with Fisker, Inc. demonstrated the feasibility of a pilot-scale freeze-casting coating line at Montana State University and made initial recommendations to Fisker on how the freeze casting process could be industrially scaled. A project with Navitas Systems Inc. resulted in a down-selection of the separator material to be used in the CRADA project. Navitas also began some trial operations handling the separator in a R2R manner at their product site. A project with SolarWindow Technologies, Inc. selected a diffractive-optical-element-based multiplexing system for R2R laser scribing that will drastically reduce up-front capital and on-going operational costs compared to currently used laser/optics systems and will also increase process speeds over galvanometer step-and-scan systems.

# Technology Assessment

## Structured Anode Study

Substantial improvements can be achieved in rated capacity at 2C discharge rates when a simple particle-size modification is used and combined with a thick bilayer approach, with an emphasis on materials processing and coating deposition methodology using R2R processes (dual slot-die and dual-pass). This technology enables simultaneous high energy and power density along with 82% capacity retention after 950 cycles.

## Fuel Cell Study

R2R fabricated electrodes without ionomer overlayer can produce the equivalent mass activity to spray-coated electrodes with an ionomer overlayer. Oxygen-limiting current measurements can be utilized to optimize oxygen mass transport. The alcohol:water (solvent) ratio can be tuned to control ionomer distribution. Water-rich solvents produce a more dispersed ink which results in better high-current density performance. Lower non-Fickian resistance can improve high current-density performance. These advancements demonstrate the possibility of a single-layer R2R-coated fuel cell electrode with comparable performance to a two-layer lab-coated electrode, increasing process throughput and reducing the number of process steps.

## Modeling, Simulation and Data Mining

Colloidal interactions between particles contribute to the rheological properties of slurries that are used in R2R manufacturing processes. Particle pair interaction potential captures all particle-particle interactions connected to effective slurry viscosity. Both polymer brush length and fractal dimension can be used as fitting parameters for microrheological modeling of a whole slurry. These findings set the framework for future materials design and fabrication.

Machine reading can accurately describe synthesis recipes in open literature publications including the synthesis method, precursors and reagents, the target end material, and physical conditions of the synthesis. A dataset of reactions from the data mining and machine learning effort will be released for public access to benefit other research in electro-chemical synthesis.

## Functional Materials

Research in functional materials showed that the synthesis techniques could significantly affect the properties and performance of the cathode materials used in LIBs. Cathodes for LIBs are manufactured in a two-step process, which involves coprecipitation and calcination. Experimental and computational analysis demonstrate that solution pH, and ammonia concentration, used during the coprecipitation step can alter the size and size-distribution of the synthesized cathode particles. Experiments that were conducted reveal that particles with narrow size distribution and relatively dense structure demonstrate better performance. Two different combinations of solution pH and ammonia concentration have been defined, which would lead to formation of large and small-sized particles, respectively, with very narrow size distributions. Further analysis also revealed that breakage of cathode particles, observed during coprecipitation, is because of fluid-shear induced forces that must also be considered when designing new materials. Formation of dense cathode particles can be attributed to the calcination step where sintering of the secondary particle helps to remove pores. Presence of a few internal pores can be explained from the distribution of primary particles after coprecipitation process. These findings are important when designing advanced cathode materials for next generation LIBs.

## R2R Water Project

Resin wafer technology is capable of providing greater than 35 % energy efficiency for water desalination compared to 15 % for the current state-of-the-art technologies. RW-EDI technology has been demonstrated in a

pilot-scale R2R semi-automated assembly line and scaling up this process is expected to result in the potential to improve separation energy efficiency and processing costs (95% for labor and 90% production time) for multiple industrial sectors.

# Roll-to-Roll Advanced Materials Manufacturing DOE Laboratory Consortium Project

## Consortium Contacts

### **Claus Daniel, Project and Consortium Team Lead**

Oak Ridge National Laboratory (ORNL)  
National Transportation Research Center  
2360 Cherahala Blvd.  
Knoxville, TN 37932  
Phone: 865-946-1544  
Email: [danielc@ornl.gov](mailto:danielc@ornl.gov)

### **David L. Wood III, ORNL Project Team Lead**

Oak Ridge National Laboratory (ORNL)  
National Transportation Research Center  
2360 Cherahala Blvd.  
Knoxville, TN 37932  
Phone: 865-574-1157  
Email: [wooddl@ornl.gov](mailto:wooddl@ornl.gov)

### **Gregory K. Krumdick, ANL Project Team Lead**

Argonne National Laboratory (ANL)  
9700 S. Cass Avenue  
Building 362  
Argonne, IL 60439-4844  
Phone: 630-252-3952  
Email: [gkrumdick@anl.gov](mailto:gkrumdick@anl.gov)

### **Michael Ulsh, NREL Project Team Lead**

National Renewable Energy Laboratory (NREL)  
15013 Denver West Parkway  
Golden, CO 80401  
Phone: 303-275-3842  
Email: [Michael.Ulsh@nrel.gov](mailto:Michael.Ulsh@nrel.gov)

### **Ravi Prasher and Vince Battaglia, LBNL Project Team Leads**

Lawrence Berkeley National Laboratory (LBNL)  
1 Cyclotron Road  
MS 70R 0108B  
Berkeley, CA-94720  
Phone: 510-495-2679  
Email: [rprasher@lbl.gov](mailto:rprasher@lbl.gov) and [vsbattaglia@lbl.gov](mailto:vsbattaglia@lbl.gov)

### **David C. Hardy, DOE Roll-to-Roll Program Manager**

Department of Energy (DOE)  
Energy Efficiency and Renewable Energy (EERE)  
Advanced Manufacturing Office (AMO)  
1000 Independence Ave., S.W., Suite 5F-063



Washington, DC 20585-0121  
Phone: 202-586-8092  
E-mail: [david.hardy@ee.doe.gov](mailto:david.hardy@ee.doe.gov)

**Technical Contacts:**

ORNL: Jianlin Li, Yarom Polsky  
ANL: Andrew Jansen, Bryant Polzin, Yupo Lin, Venkat Srinivasan  
NREL: Scott Mauger, Peter Rupnowski, Maikel Van Hest  
LBNL: Vince Battaglia, Kenny Higa, Gerd Ceder, Olga Kononova

**Industry Partners:**

Kodak Eastman Business Park  
Fisker, Inc.  
Navitas Systems LLC  
SolarWindow Technologies, Inc.  
Proton OnSite

**Annual Operating Plan Title and Corporate Planning System (CPS) Agreement Numbers**

Roll-to-Roll Manufacturing Science and Applications: From Ideal Materials to Real-World Devices/  
ORNL CPS# 97995  
ANL CPS #s 29915, 32553 and 32681  
NREL CPS #97995  
LBNL CPS #31112

## Project Introduction

Modern variants of proven, classical R2R coating technologies, as well as new coating methods, are needed for enabling widespread commercialization of renewable energy storage and conversion technologies. Established coating methods, such as multi-layer slot-die, gravure, reverse comma, tape casting, etc. with homogeneity and uniformity superior to spraying methods need to be further adapted for improving performance of various technologies. Examples of sustainable energy technologies and applications are electrochemical energy storage and conversion such as batteries, electrolytic hydrogen production for fuel cells and water separation, smart flexible sensors for building energy efficiency improvement, flexible displays such as organic light emitting diodes and electronics, and PV panels. The shape, size, and morphology of the materials, the chemistry of the formulation, the nature of slurries, their coating rate, the rate of drying etc. all play a role in determining the final coating architecture, quality, and performance. In addition, NDE of the produced coatings for improving in-line quality control (QC) and identification of defects, prior to down-stream value added steps being performed, is of paramount importance.

The challenges to develop new technologies in these areas brought together expertise from four national laboratories to solve the complex nature of the R2R process and methods to improving existing production capabilities. The project has expanded in the second year to focus on fuel cell materials, water separation and purification, and new functional materials. An effort to get industry more involved was initiated through a CRADA solicitation that has produced interest from the commercial sector.

## Objectives

The objectives of this collaborative effort for R2R AMM is to advance technologies applicable to continuous manufacturing to reduce cost, increase precision, and enable in-line QC and defect detection that will result in expanded use of R2R processing to produce clean energy technologies. Efforts will use modeling and simulation of the materials and processes for the technologies being developed to understand the fundamental physics and particle interactions of those materials as they relate to the manufacturing process. Additionally, a supporting effort is for data mining to create a database of “codified” synthesis recipes extracted from scientific publications by using text data mining and natural language processing techniques. The information gained during the data mining will be used to apply a deep learning methodology to learn synthesis patterns of known battery materials and use this to predict the synthesis routes of novel compounds.

## Approach

### Core Program

#### Structured Anode Study

In FY 2018, ANL focused on completing the testing of coin cells with structured cathodes and matching anodes and provided certain cell sets and their associated pristine electrodes for post-test analysis in an attempt to understand the reasons for the differences in cell performance. The materials that were used to produce these electrodes were a Li metal oxide powder from TODA America, Inc. (TODA) (NMC532) with particle sizes of 6 and 12 micrometers ( $\mu\text{m}$ ) and a graphite powder from Superior Graphite (SLC1506T and SLC1520P) with a particle size of 6  $\mu\text{m}$  and 20  $\mu\text{m}$ . These powders were used as individual powders, blended

mixes and layered structures in the electrodes. The intent was to provide electrode structuring would yield a higher level of electrochemical performance in high loading electrodes.

ORNL prepared graded cathodes and matching anodes and built devices (with emphasis on pouch cells) for testing. Rate performance and cycle life testing of single-layer pouch cells fabricated with the structured anodes and cathodes was performed in FY 2018. The performance of the electrode materials was characterized using scanning electron microscopy (SEM) and Hg porosimetry to identify material structures and properties.

## **Fuel Cell Study**

NREL, as the lead lab for the Fuel Cell Study, addressed an emerging membrane electrode assembly (MEA) construction method – namely GDEs – by identifying processes that can reduce the number of steps (specifically that of coating an ionomer overlayer on the surface of the electrode) in the overall electrode R2R fabrication process. The approach is to understand the fundamental (nano- and micro-scale) interactions in the heterogeneous electrode ink that lead to macro-scale properties determined by rheology, which ultimately impacts coating and drying parameters as well as device performance. NREL tasks include coordination of data informatics on the fabrication, characterization, and in situ testing; development of cutting-edge coatings and deposition science applicable to fuel cells; and fabrication and in situ testing of prototype components and devices. NREL will leverage FCTO investments in QC development for fuel cell electrodes and identify techniques relevant to the GDE construction.

ANL supported the Fuel Cell Study by providing characterization of catalyst-ionomer-solvent inks, studying ink synthesis parameters (such as sonication time and energy), and characterizing the microstructure of electrodes. ANL tasks were to use ultra-small angle x-ray scattering (USAXS) to characterize inks under different ultrasonic and shear mixing conditions and to characterize the structure of electrodes made from these inks using nano-CT.

The ORNL tasks for the Fuel Cell Study were to investigate low-cost methods of MEA manufacturing (slot-die) for coating of electrocatalyst layers onto gas diffusion media to make GDEs, utilize R2R hot-pressing (calendering) of GDEs to polymer electrolyte membranes (PEM) to make “unitized” MEAs, and implement processes for thickness control and metrology for MEA production QC.

LBNL modeling capabilities were leveraged to aid in optimizing ink formulation and process parameters via phase field modeling of the material segregation during drying as well as mechanistic modeling of ink rheology.

## **Modeling, Simulation and Data Mining**

LBNL developed a physics model based on colloidal interactions and this model will be improved for predicting the rheological properties of slurries for electrode materials. Major interactions between particles, such as Van der Waals, electrostatic, and polymer steric interactions were included for calculating the viscosities. LBNL continued to investigate the properties of slurries, including particle size and zeta potential, particle and polymer mass ratio, and particle volume fractions. The current model well predicts the viscosities of anode slurries and will be modified for other materials including fuel cell materials.

A machine learning algorithm was implemented to identify potential targets and precursors of a synthesis route. The algorithm employs bi-directional recurrent neural network architecture with long short-term memory (LSTM) units. The algorithm was trained on ~700 sentences. The current accuracy estimated by calculation F1 score is: for materials F1 = 84%, for targets F1 = 83%, for precursors F1 = 84%. A Materials Entity Recognition algorithm was also developed and implemented to identify materials mentions in synthesis paragraphs and classify which materials are mentioned in context of starting compounds (precursors) and final

products (targets) of the synthesis. The algorithm uses a recurrent neural network model with LSTM units to scan tokens in synthesis paragraph sentences and identify tokens which represent materials entities. The accuracy of the algorithm is ~90%. In significant number of paragraphs, target names are given in the form of an abbreviation, yet other significant fraction of target names contain off-stoichiometric variables.

Another algorithm was implemented which obtains sequence of synthesis step from the synthesis paragraphs. The algorithm utilizes feedforward neural network combined together with Word2Vec model and a grammatical parser to traverse each sentence in the paragraph word by word and classifies them according to the following categories: not operation, start of synthesis, heating operation, mixing operation, drying operation, shaping operation and quenching operation.

## **Functional Materials**

Detailed in situ and ex situ experiments were conducted at the ANL Advanced Photon Source (APS) to understand the growth dynamics of primary and secondary particles observed during the coprecipitation of nickel-manganese-cobalt (NMC) hydroxide precursors. Solution pH was altered to demonstrate its impact on the size, tap density, and internal porosity of the secondary particles. The precipitated precursors were oxidized and lithiated, through the calcination process, to form realistic cathode materials. These cathode particles were cycled in a coin cell to demonstrate its performance and cycle life against Li metal anodes.

A computational methodology was developed in FY 2017 to elucidate the mechanism behind the formation of primary and secondary active particles during the coprecipitation process. Mass balance relations for the reactants were coupled with the mechanisms of nucleation, growth and aggregation of the primary particles to successfully capture the formation of secondary active particles. In FY 2018, the computational methodology that was developed has been extended to analyze the impact of solution pH and ammonia content on the size and size distribution of the secondary particles. Further extension of the computational model was conducted to analyze the fluid shear induced breakage of the cathode particles during the coprecipitation process. A phase field-based model was also developed to elucidate the impact of sintering on the densification of particles observed during the high temperature calcination. Sintering of two and three particles were analyzed to demonstrate the removal of pores, and fusion of particles, that may occur as part of calcination.

## **R2R Water Project**

ANL continued to investigate materials for water separation and purification using a SAAL prototype system that was assembled in FY 2018. For each material fabricated with a this R2R method, the resin wafers will be characterized for porosity and pore distribution, flow and ionic conductivity. Water desalination performance and energy extraction from concentrated salt brine will be evaluated for each wafer configuration fabricated.

## **FY 2019 Plans**

### **Core Program**

In FY 2018, all tasks in the core program for the R2R AMM DOE Laboratory Consortium that began in FY 2016 were completed. This is the final report detailing the last year of this program's efforts. Further work for some of the specific technologies that were developed in FY 2016 through FY 2018 will be transitioned to a new project titled "Early-Stage Advanced National Multi-Laboratory Roll-to-Roll R&D Collaboration" that was selected for FY 2019 through FY 2021.

### **CRADAS**

Efforts for the CRADA projects with agreements negotiated in FY 2018 will continue into FY 2019 to meet contractual and programmatic requirements. This includes the following three efforts:

- Fisker, Inc. - Fisker, Inc. has partnered with LBNL and ORNL to demonstrate all-solid-state batteries based on LLZO separators and cathode scaffolds that will allow scaling a freeze casting process to the pilot level at ORNL.
- Navitas Systems, Inc. - Navitas Systems, Inc. has partnered with ORNL and NREL to demonstrate R2R production of an advanced separator for LIBs.
- SolarWindow Technologies, Inc. – SolarWindow Technologies, Inc. has partnered with NREL and ANL to demonstrate diffractive multiplexing for high-throughput R2R laser patterning of flexible organic PV modules.

A fourth CRADA project with Proton OnSite was selected to research R2R manufacturing of advanced (low loading, direct coated onto membrane) electrolysis electrodes for low-cost hydrogen production and remains in the approval process at the end of FY 2018. The project is expected to start early to mid-FY 2019. Proton OnSite will partner with NREL, ORNL, and ANL for this project.

## Potential New Projects

AMO released a Laboratory Call L059-1649 Announcement in FY 2018. ORNL coordinated an effort to solicit technical project descriptions (a total of 53 were received) for a coordinated effort involving up to six DOE national laboratories. A proposal to the Laboratory Call was submitted by ORNL on June 19<sup>th</sup>, 2018 titled “Early-Stage Advanced National Multi-Laboratory Roll-to-Roll R&D Collaboration with Industrial CRADA Collaboration, Topic Area 3: Roll-to-Roll Processing”. The FY 2016 through FY 2018 efforts will transition to a new project for FY 2019 through FY 2021.

## Technology Transfer Paths

For the core program tasks, technology will be transferred through collaboration with industry and companies with CRADA contracts and the DOE team will work closely with any companies to ensure technologies are accepted for commercialization. Various aspects of the R2R AMM program was presented at conferences, symposia, peer reviews and during direct contact with industry and the commercial sector. Specific research was reported in technical journals and through patent applications.

The models and simulations will be extended to encompass not only materials discovery, but also to accelerate materials synthesis and fabrication. This effort leverages the R2R processes and technologies at ORNL, the engineering expertise and research facilities such as the APS and the Materials Engineering Research Facility (MERF) at ANL, and the metrology advances and capabilities at NREL in conjunction with the materials design computational efforts of ANL and LBNL.

## Results

### Structured Anode Study

The Structured Anode Study examined 49 cell combinations in a 7x7 matrix with three replicates each for a total of 147 cells. Discharge rate performance testing was completed during FY 2018 for seven new anodes and seven cathode structures developed in FY 2016 that had loadings of 4 mAh/cm<sup>2</sup>. Long-term coin cell cycling was conducted by ANL. Pouch cell rate performance and long-term pouch cell cycling at high

discharge rates of C/2:2C and low discharge rates of C/2:C/2 were conducted at ORNL. Other analyses included SEM and Hg porosimetry characterization of some samples. NREL conducted metrology and QC studies on the anode materials. Samples were run on the NREL web-line using the porosity diagnostic equipment setup previously used for cathodes. Data was taken with both mid-infrared (IR) and far-IR cameras to understand potential differences due to surface structure/emissivity.

## Argonne National Laboratory

### Completion of the FY 2017 Coin Cell Matrix Testing

Testing was completed for the cells that were on test during the last quarter of FY 2017 and for the remaining cells in the cathode-anode electrode matrix. The pristine anodes/cathodes and the cathode and anode combinations that comprised the coin cells were as follows:

- All small particles
- All large particles
- Mixed small/large particles
- Small particles top / large particles bottom (dual-pass)
- Small particles top / large particles bottom (single-pass)
- Large particles top / small particles bottom (dual-pass)
- Large particles top / small particles bottom (single-pass)
- Cathode and matching anode combinations listed in Table 1

Figure 1 (a) shows micrographs for the pristine baseline anodes made at ANL and Figure 1 (b) shows some of the structured combinations made using a dual pass (DP) and single pass (SP) process at ORNL.

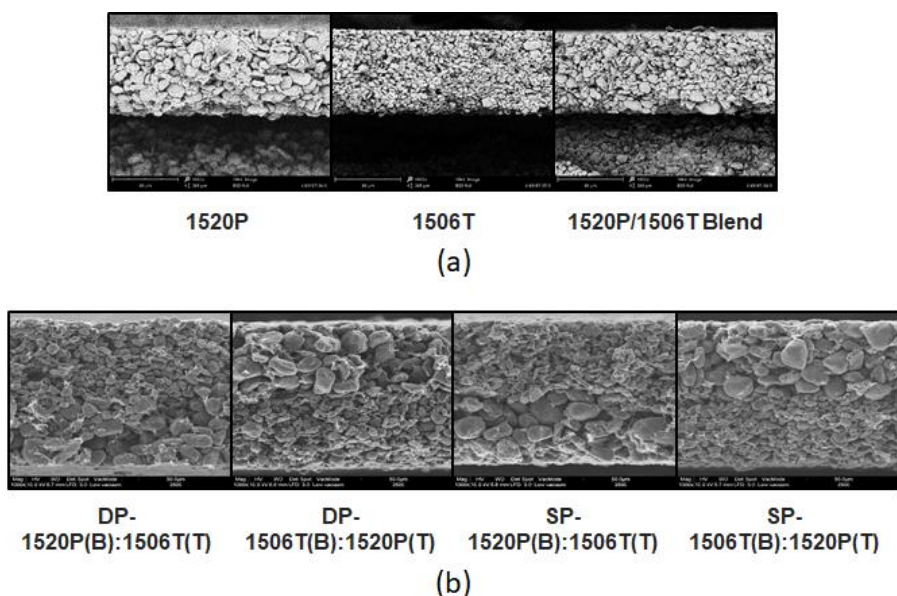


Figure 1. (a) Micrograph of the pristine anodes fabricated at ANL and (b) structured combinations made at ORNL.  
Source: ANL and ORNL

Table I shows the coin cell testing matrix for the sequence of testing of all cell sets from FY 2016 through FY 2018.

**Table I. R2R AMM Coin Cell Testing Matrix**

Anodes							
FY 2016 Cathodes	SLC1520P	SLC1506T	SLC1520: SLC1506T Blend	Dual Pass 1520PB: 1506TT	Dual Pass 1506TB: 1520PT	Single Pass 1520PB: 1506TT	Single Pass 1506TB: 1520PT
Low Loading	LN3107-31-3	LN3107-32-2	LN3107-33-2	—	—	—	—
6 $\mu$ m Baseline	FY 2017	FY 2017	FY 2017	Not Applicable	Not Applicable	Not Applicable	Not Applicable
High Loading	LN3107-36-3	LN3107-37-3	LN3107-38-3	LN2486-68	LN2486-69	LN2486-70	LN2486-71
6 $\mu$ m	FY 2016/ FY 2017	FY 2017	FY 2017	FY 2017	FY 2017	FY 2017	FY 2017
6 $\mu$ m/12 $\mu$ m Blend	FY 2016	FY 2018	FY 2018	FY 2018	FY 2018	FY 2018	FY 2018
Dual Pass – 6B:12T	FY 2016	FY 2017	FY 2017	FY 2018	FY 2018	FY 2018	FY 2018
Dual Pass – 12B:6T	FY 2016	FY 2017	FY 2017	FY 2017	FY 2017	FY 2017	FY 2017
Single Pass - 12B:6T	FY 2016	FY 2018	FY 2018	FY 2018	FY 2018	Not Applicable	Not Applicable
Single Pass – 6B:12T	FY 2016	FY 2017	FY 2017	FY 2017	FY 2017	FY 2017	FY 2017
12 $\mu$ m	FY 2018	FY 2018	FY 2018	FY 2018	FY 2018	FY 2018	FY 2017

A total of 50 coin cell sets were tested in this matrix for initial capacity, rate, hybrid pulse-power capability (HPPC), and life cycle test. Each coin cell set represented one electrode combination in the matrix, and each set had four replicate coin cells for better accuracy. Two cell sets ([SP-12(bottom (B)):6(top (T)) NMC532 versus SP-1520P(B):1506T(T)] and [SP-12(B):6(T) NMC532 versus SP-1506T(B):1520P(T)]) were deleted from the full test matrix. Previous coin cell sets that used these single-pass anodes typically reached 80 % capacity retention early, usually within 150 cycles.

The life cycle testing protocol was to expose each cell to 3.0 V to 4.2 V charging at 30°C with 47 charge and discharge cycles at C/2 and one cycle at C/20. This protocol repeated until there was <80% discharge capacity retention. The HPPC consisted of a 2.25C charge and a 3C discharge pulses. The charge/discharge cycles and the HPPC test were looped five times or until less than 80% capacity retention was reached. The total test time was 3 to 5 months per cell set. Typically, 48 test channels were available at one time. The number of full cells tested were as follows: 6 sets in FY 2016, 24 sets in FY 2017 and 21 sets in FY 2018.

The representative data for the top coin cell performers at the end of FY 2017, highlighted in yellow in Table II, were the baseline (low loading) 6 $\mu$ m NMC532 cathode paired with all three low loading anodes (1520P, 1506T, and a 50/50 mix of 1520P and 1506T (Superior Graphite)); DP-12(B):6(T) NMC532 cathode paired with 1520P and with 50/50 mix of 1520P and 1506T; and high loading 6  $\mu$ m NMC532 cathode paired with 1520P, with 1506T, and with DP-1506T:1520PT. Data analysis was performed on all finished cells.

At the beginning of FY 2018, the representative data for the cells that finished cycling are identified with a red font in Table II. From these eight cell sets, only one set performed well enough to be included in the top performer's list. This cell set was the 6 $\mu$ m (high load) versus the DP with small particles in the bottom layer and large particles in the top layer (DP-1506T(B):1520P(T)). These cells went through formation, rate study,



HPPC, and cycle life testing protocols. Data analysis was performed on the cell sets and the data was added to the compiled cell analysis file.

**Table II. Capacities for Cell Sets Developed in FY 2017**

NMC 532 Electrode (particle sizes in μm)	Superior Graphite Elcetrode	Total Number of Cycles Tested on Cells	Discharge Capacity Retention (%)	Cycle at 80% Discharge Capacity Retention (Cycles into Cycle Life)
Baseline: 6 μm Low Loading	1520P	522	79.6 %	491
	1506T	522	78.0 %	441
	1520P/1506T mix (50/50)	522	79.8%	496
Dual Pass – 12B:6T	1520P	522	77.2 %	385
	1506T	522	63.6 %	185
	1520P/1506T mix (50/50)	772	71.9 %	472
	DP – 1520P(B):1506T(T)	522	70.7 %	124
	DP – 1506T(B):1520P(T)	272	69.0 %	124
	SP – 1520P(B):1506T(T)	272	63.9 %	13
	SP – 1506T(B):1520P(T)	272	47.2 %	15
6 μm	1520P	522	77.0 %	386
	1506T	522	78.9 %	474
	1520P/1506T mix (50/50)	522	70.0 %	235
	DP – 1520P(B):1506T(T)	272	77.9 %	185
	DP – 1506T(B):1520P(T)	522	74.1 %	370
	SP – 1520P(B):1506T(T)	522	68.0 %	309
	SP – 1506T(B):1520P(T)	272	69.3 %	81
Single Pass – 6B:12T	1520P	522	75.1 %	288
	1506T	522	68.4 %	275
	1520P/1506T mix (50/50)	522	70.7 %	320
	DP – 1520P(B):1506T(T)	522	71.9 %	272
	DP – 1506T(B):1520P(T)	522	68.5 %	138
	SP – 1520P(B):1506T(T)	272	78.7 %	231
	SP – 1506T(B):1520P(T)	272	66.2 %	75
Dual Pass –6B:12T	1520P	522	74.7 %	295
	1506T	522	69.1 %	229
	1520P/1506T mix (50/50)	522	67.4 %	244

The discharge capacity data for all representative coin cell sets tested in FY 2018 is shown in Figure 2. A summary for the number of cycles for the electrode pairs to reach an average 80% discharge capacity retention for the completed full coin cell test matrix is shown in Table III. Based on the coin cell data, it appears that the best anodes include: the blend of small and large graphite particles; and large graphite particles, while the best cathodes include: small NMC particles; blend of small and large NMC particles; and dual pass with large NMC particles on the bottom.



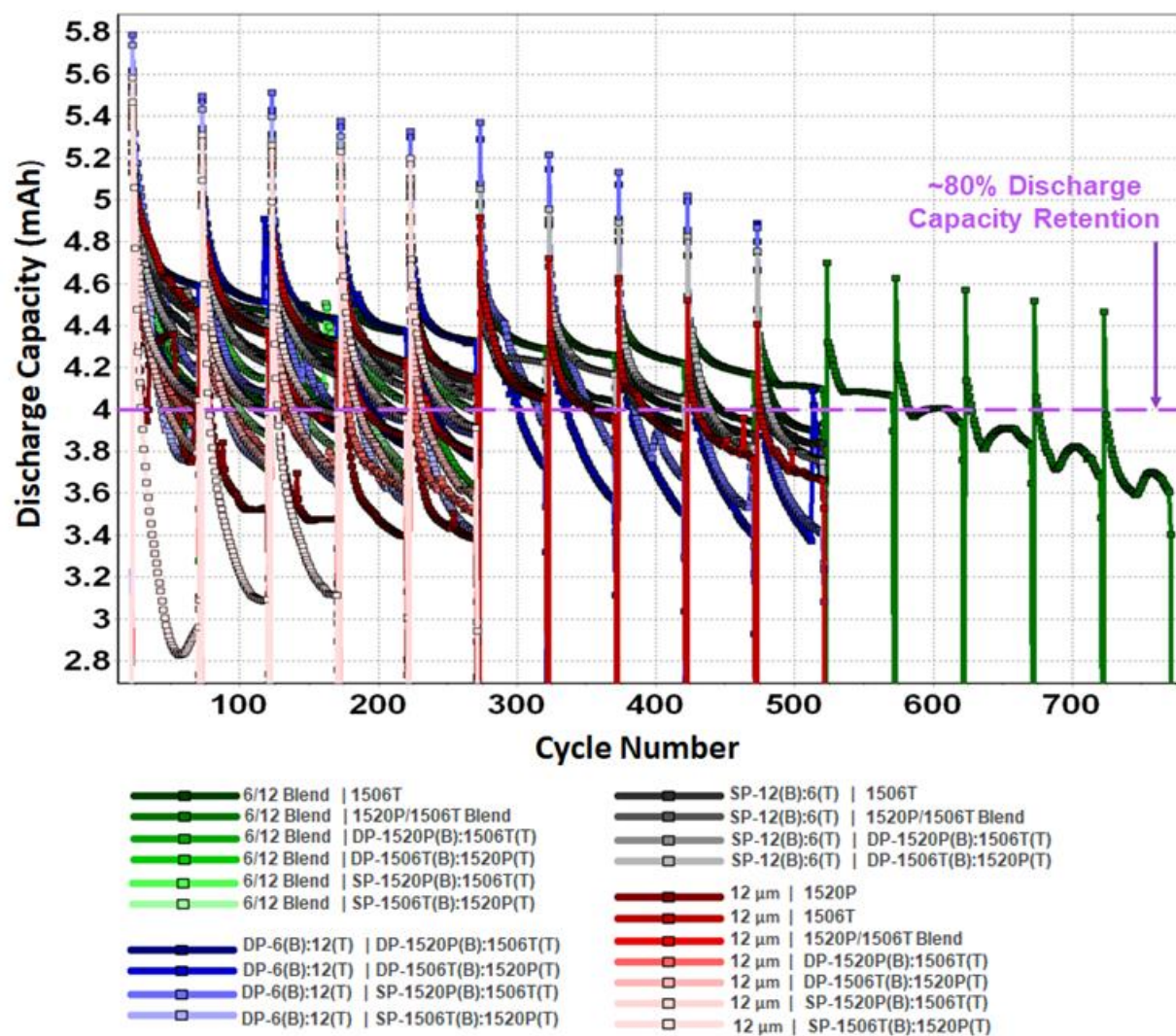


Figure 2. Discharge capacity in mAh of cathode active material from representative coin cells of FY 2018 cell sets. Source: ANL

Table III. Number of Cycles to Average 80% Discharge Capacity Retention

High Loading Anodes							
High Loading Cathode	SLC1520P	SLC1506T	SLC1520P/ SLC1506T Blend	DP - 1520P(B):1506T(T)	DP - 1506T(B):1520P(T)	SP - 1520P(B):1506T(T)	SP - 1506T(B):1520P(T)
6 $\mu\text{m}$	498 (22.9, 24.6) Rate : 148 / 134	427 (22.1, 23.6) Rate : 154 / 139	291 (21.9, 23.1) Rate : 152 / 136	144 (24.9, 26.4) Rate : 158 / 136	277 (25.2, 25.9) Rate : 159 / 139	222 (25.5, 26.2) Rate : 158 / 141	77 (27.3, 32.0) Rate : 159 / 131
6 $\mu\text{m}$ /12 $\mu\text{m}$	327 (28.7, 30.3) Rate : 149 / 130	437 (25.9, 28.0) Rate : 157 / 139	591 (26.6, 28.4) Rate : 153 / 137	90 (24.3, 27.8) Rate : 159 / 120	28 (24.6, 29.9) Rate : 160 / 128	239 (26.1, 29.2) Rate : 161 / 124	39 (24.5, 28.7) Rate : 159 / 132
DP - 6B:12T	237 (27.2, 29.6) Rate : 153 / 131	225 (32.2, 36.7) Rate : 155 / 136	244 (40.1, 42.1) Rate : 157 / 138	179 (31.2, 36.0) Rate : 159 / 126	282 (31.5, 33.1) Rate : 159 / 143	235 (28.6, 33.0) Rate : 160 / 133	24 (31.1, 36.2) Rate : 161 / 128
DP - 12B:6T	498 (24.9, 26.1) Rate : 152 / 136	134 (30.0, 31.6) Rate : 155 / 136	528 (29.9, 32.0) Rate : 153 / 138	191 (27.6, 32.3) Rate : 157 / 132	84 (27.9, 31.9) Rate : 156 / 135	12 (29.4, 39.4) Rate : 157 / 112	29 (28.9, 34.7) Rate : 156 / 128
SP - 12B:6T	97 (32.1, 35.2) Rate : 149 / 129	334 (19.8, 22.4) Rate : 157 / 140	277 (20.9, 23.2)* Rate : 152 / 137	144 (-, -)* Rate : 159 / 131	391 (17.1, 21.2)* Rate : 159 / 137	-	-
SP - 6B:12T	433 (31.6, 33.9) Rate : 151 / 128	275 (30.0, 32.8) Rate : 156 / 136	319 (31.8, 34.3) Rate : 154 / 136	278 (29.0, 32.9) Rate : 159 / 133	141 (29.8, 34.0) Rate : 159 / 133	147 (31.4, 35.4) Rate : 158 / 127	30 (34.9, 40.5) Rate : 158 / 128
12 $\mu\text{m}$	74 (20.4, 22.8) Rate : 155 / 127	373 (-, -)* Rate : 156 / 139	239 (20.0, 23.0) Rate : 153 / 129	30 (19.7, 24.7) Rate : 158 / 112	38 (19.7, 24.8) Rate : 159 / 126	245 (19.0, 23.9) Rate : 159 / 111	11 (20.2, 30.3) Rate : 158 / 109

Within Each Paired Electrode Square in Table

- ◆ Top Line + Outside Parenthesis = Cycle Number @ Average 80% Discharge Capacity Retention
- ◆ Top Line + Inside Parenthesis = Average Discharge ASI @ 50% SOC during ... ( Initial HPPC, 2nd HPPC)  $\Omega \cdot \text{cm}^2$
- ◆ Rate : 0.1C / 1C (in mAh/g) Average Specific Discharge Capacity at C/10 and 1C rate from Rate Test

Not Tested =	-
--------------	---

\* means that only some (or none) of the cells were able to finish pulses. The number in the parenthesis is the average of the cells that did complete.

## Post-Test Analysis

In order to understand the reasons for the differences in cell performance, certain cell sets were sent for post-test analysis as were the cell's associated pristine electrodes. A test sample is shown in Figure 3.



Figure 3. Glove box photo of the negative electrode from a coin cell set. Source: ANL

The chosen cells and electrodes are shown in Table IV. The pristine cathodes consisted of 6  $\mu\text{m}$  (low loading) which was the baseline, 6  $\mu\text{m}$  (high loading) and DP-12(B):6(T) (high loading). The pristine anodes consisted of 1506T (low loading), 1506T (high loading), 1520P/1506T - 50/50 mix (high loading) and SP-1520P(B):1506(T) (high loading).

**Table IV. Cells Chosen for Post-Test Analysis**

Chosen Cells			
NMC 532 Cathode ( $\mu\text{m}$ )	Superior Graphite Anode	Cycle at 80% Discharge Capacity Retention (Cycles into Cycle Life)	Reason for Choice
Baseline 6 $\mu\text{m}$	1506T	441	Low Loading, 6 $\mu\text{m}$ Good Performance
6 $\mu\text{m}$	1506T	474	High Loading, 6 $\mu\text{m}$ Good Performance High Loading,
Dual Pass – 12 $\mu\text{m}$ (B):6 $\mu\text{m}$ (T)	1520P/1506T (50/50) mix	472	High Loading, Structured Cells, Good Performance
	Single Pass – 1520P(B):1506T(T)	13	High Loading, Structured Cells, Poor Performance

Optical microscopy was used initially on the electrodes, but the results were indecipherable because the depth of field was not large enough. The Post Test Facility conducted surface and cross-sectional microscopy on the electrodes. As cells were disassembled and images were taken of the electrodes, neither Li plating or delamination was initially seen on the anode.

After the cells were disassembled, SEM images were taken of the electrodes. The graphite particles were covered in small particles, as seen at location 1 in Figure 4 (a), which were relatively high in fluorine and phosphorus. One of the more noticeable differences is that the cells with poor performance have a weak bond with the current collector. The laminate fell off during handling as seen in Figure 4 (b). Further studies of the cycled and pristine electrodes are planned.

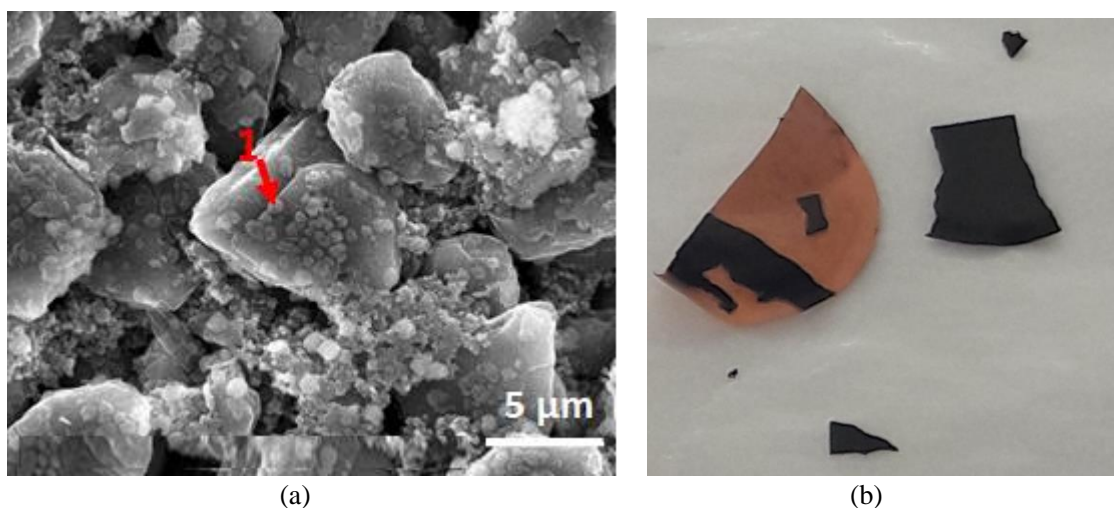


Figure 4. Post-test analysis: (a) particles present on the anode surface and (b) optical image of anode electrode delamination. Source: ANL



## Oak Ridge National Laboratory

### Rate Performance of Single-Layer Pouch Cells with Structured Anodes and Cathodes

ORNL conducted rate performance testing of single-layer pouch cells with all forty-nine combinations of structured anodes and cathodes. Figure 5 is an illustration of the structured cathodes and anodes showing the particle compositions for the pouch cell testing and the matching sequence.

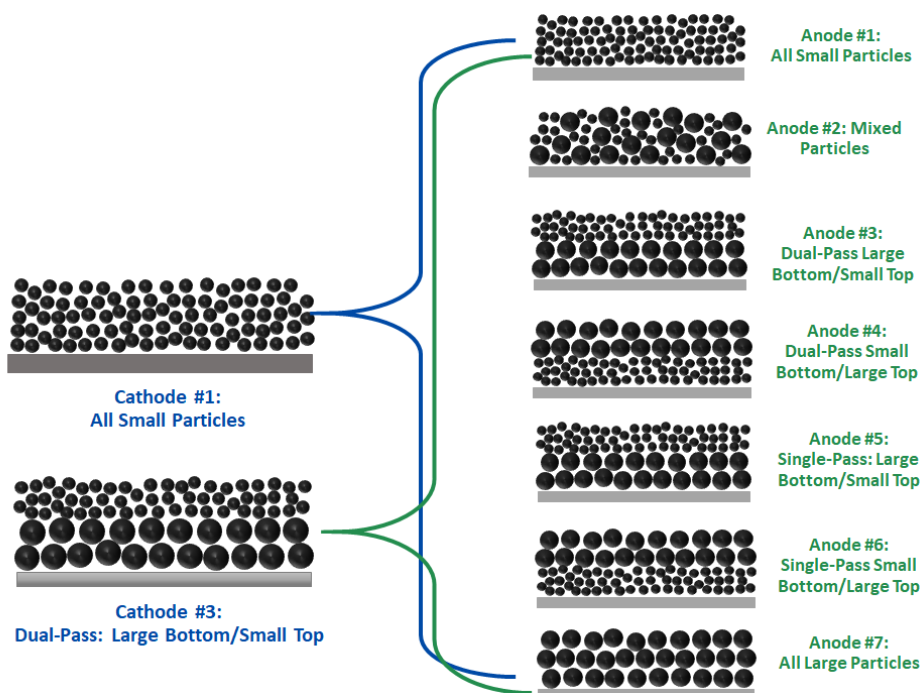


Figure 5: Cathode and anode compositions for pouch cell testing. Source: ORNL

The results for the best and worst anode/cathode combinations are shown in Figure 6. Each data point is an average of three pouch cells, with the initial capacity taken as the capacity at a discharge rate of  $C/10$ . The error bars represent the standard deviation at each  $C$  rate. All cells were filled with 1.2 M LiPF<sub>6</sub> in 3:7 wt% EC/EMC electrolyte. These two groups begin to separate at 1C and show significant capacity differences at 2C and 3C, with the best anode/cathode combination (dual-pass cathode with large particles on bottom/dual-pass anode with small particles on bottom) reaching 59% of original capacity at 2C and the worst anode/cathode combination (all large particle cathode/single-pass anode with large particles on bottom) only reaching 25%. These results demonstrated that the rate performance at high  $C$  rates can be substantially improved by pairing specific structured anodes and cathodes together. While it was difficult to determine a distinct pattern for the anodes among these two groups, a clear trend can be observed for the cathodes. The best performing cathodes are #1 (all small particles) and #3 (dual-pass with large particles on bottom), while the worst performing cathodes are #7 (all large particles), #4 (dual-pass with small particles on bottom), and #6 (single-pass with small particles on bottom).

Although the rate performance seemed to be more dependent on the cathode than the anode, the choice of anode for a particular cathode is still very important. For example, cells made with cathode #3 (dual-pass with large particles on bottom) and anode #4 (dual-pass with small particles on bottom) achieved 59% of their original capacity at 2C, whereas cells made with cathode #3 and anode #5 (single-pass with large particles on bottom) reached only 44% of their original capacity at 2C.

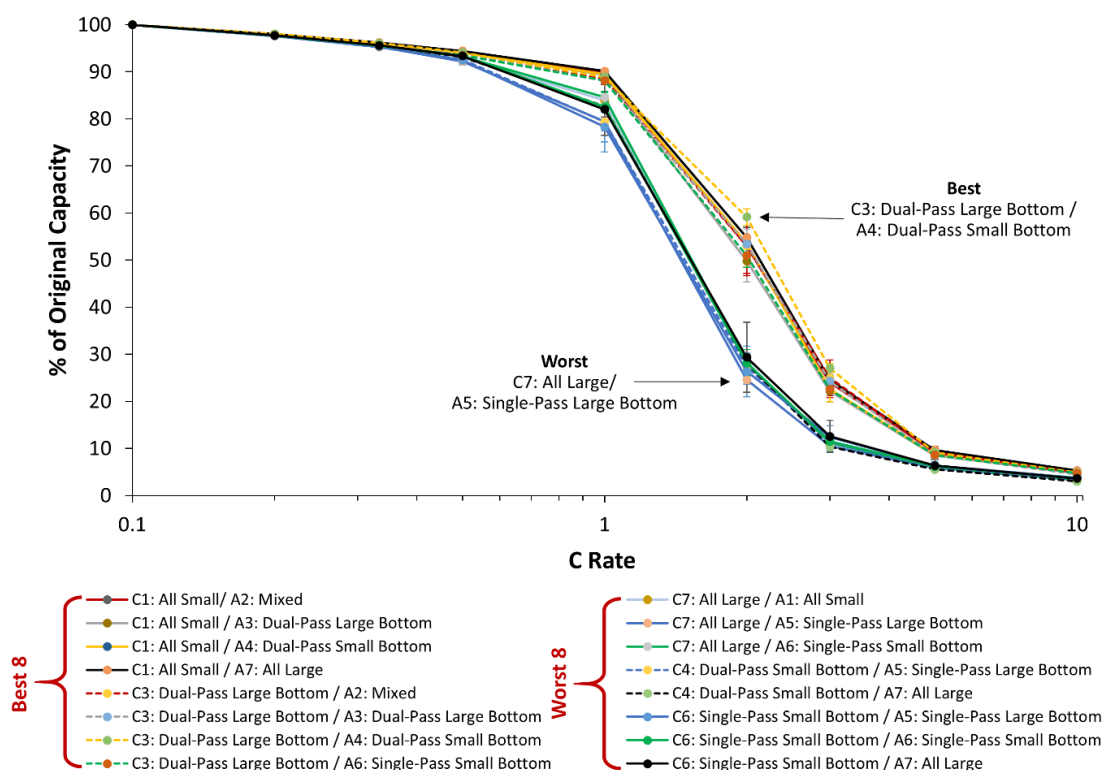


Figure 6. Comparison of the discharge rate performance of single-layer pouch cells made with the best and worst anode/cathode combinations. Source: ORNL

In order to more clearly display the differences between cells made with different two-layer anode and cathode configurations, the rate performance of all cells with two-layer anodes is plotted in Figure 7 (a), while the rate performance of all cells with two-layer cathodes is plotted in Figure 7 (b). Each data point is an average of three pouch cells, with the initial capacity taken as the capacity at a discharge rate of  $C/10$ . The error bars represent the standard deviation at each C rate. All cells were filled with 1.2 M LiPF<sub>6</sub> in 3:7 wt% EC/EMC electrolyte. Again, there was no clear trend observed in the 2C rate performance of cells made with different two-layer anodes. Conversely, cells made with two-layer cathodes containing large particles on the bottom performed significantly better (as a group) than those made with two-layer cathodes containing small particles on the bottom. This reinforces observations from Figure 6 where the best cathodes included one two-layer coating with large particles on the bottom (#3), while the worst cathodes include both two-layer coatings with small particles on the bottom (#4 and #6).

Overall, these results demonstrate that the performance at high C rates can be substantially improved by structuring the cathode and anode. While the cathode seems to have more of an impact on overall cell performance, the choice of anode is also critical.

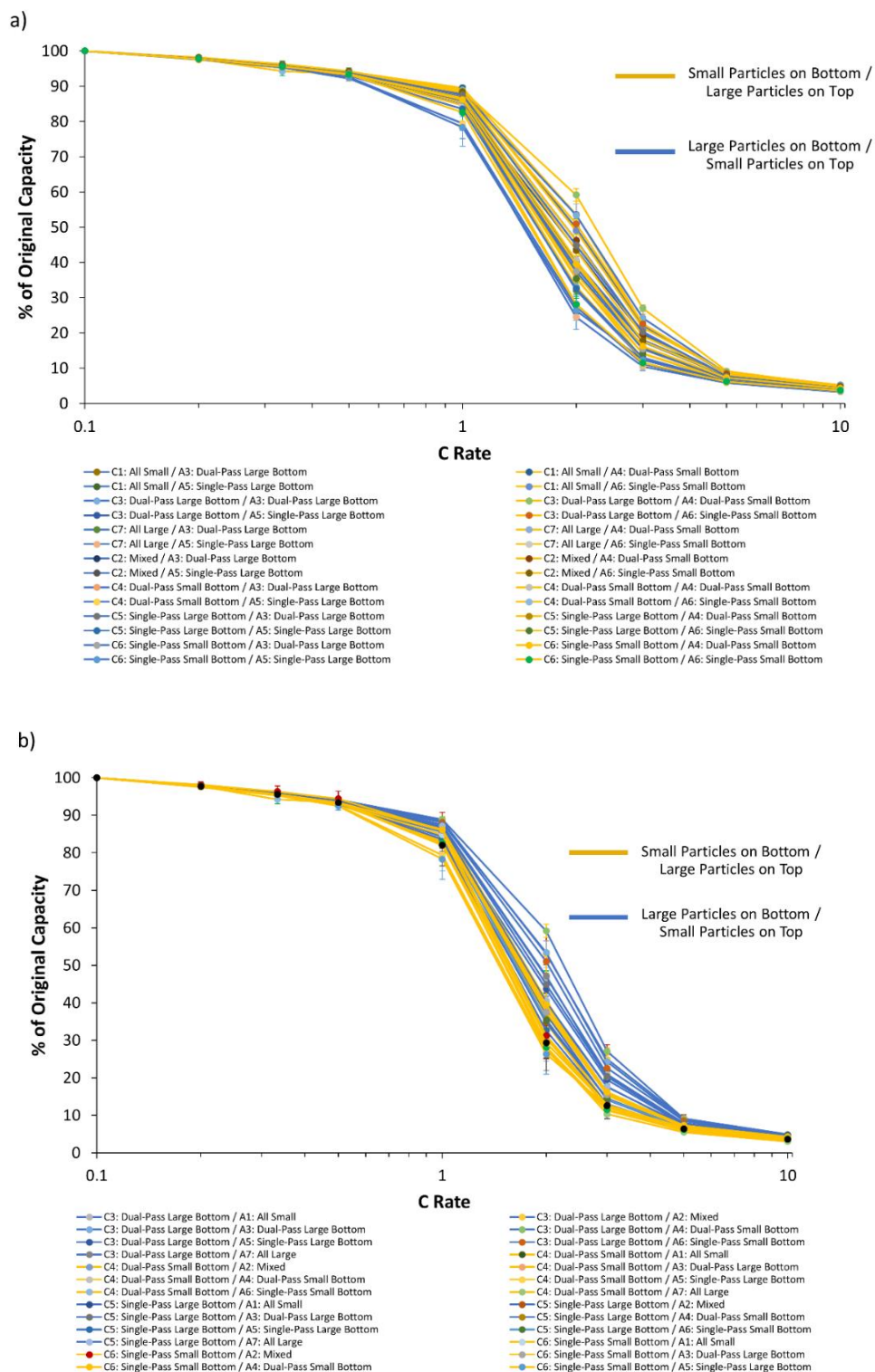


Figure 7. Comparison of the discharge rate performance of single-layer pouch cells made with the following two-layer anode and cathode configurations or small particles on bottom/large particles on top (represented by the yellow lines) and large particles on bottom/small particles on top (represented by the blue lines): (a) all cells with two-layer anodes and (b) all cells with two-layer cathodes. Source: ORNL

## Cycle Life Testing of Single-Layer Pouch Cells Made with Structured Electrodes

ORNL also conducted cycle life testing of selected top-performing single-layer pouch cells made from the structured electrodes. A total of sixteen pouch cells were selected based on the results summarized in Table V for the coin cell cycle life data (Column 2, ANL) and the pouch cell capacity retention at the 2C rate (Column 5, ORNL) available at the time (FY 2017). Cells are ranked according to their capacity retention at 2C. The rate performance and cycle life results were not expected to necessarily agree, since structures that are good for rate performance may not be good for cycle life and vice-versa. The sixteen structured anode and cathode combinations chosen for cycle life testing in single-layer pouch cells at ORNL are shown in Figure 8.

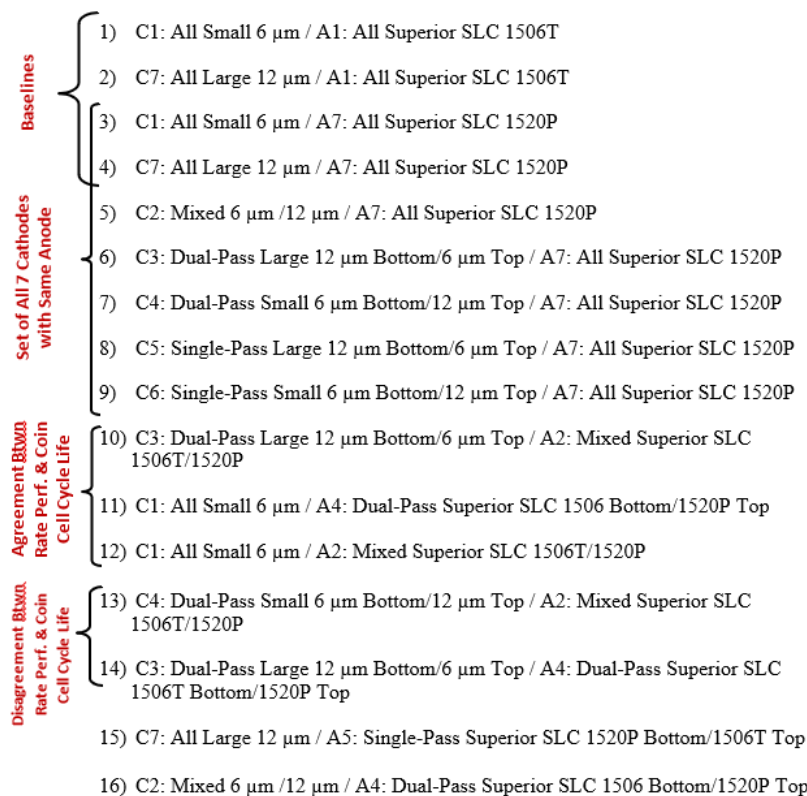


Figure 8. Structured cathode/anode combinations chosen for pouch cell cycle life testing. Source: ORNL

Combinations were selected based on both agreement and disagreement between the two data sets to cover a wide range of conditions (all forty-nine could not be tested due to limited channel availability). In addition, all four baseline combinations were included, and since the cathode structuring was found to have a more significant impact on rate performance than the anode, a complete set of all seven cathodes with the same baseline anode was also included for direct comparison. Six single-layer pouch cells were made for each cathode/anode combination. Initially, three were cycled at C/2 charge, C/2 discharge, while the other three were cycled at C/2 charge/2C discharge, since the latter is the capacity where we begin to see significant differences in the rate performance results.

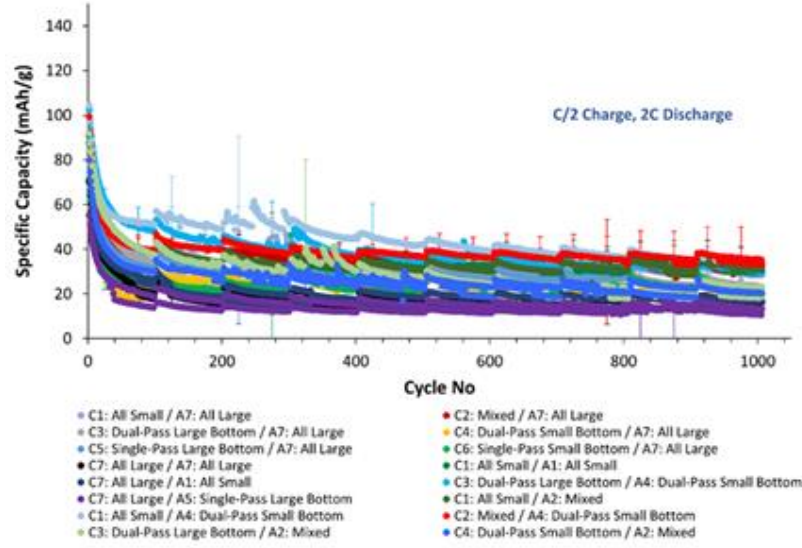
**Table V. Comparison of ORNL Single-Layer Pouch Cell Rate Performance Results and ANL Coin Cell Cycle Life Test Results**

Rank (Best to Worst Based on 2C Capacity)	Rep Cycle @ 80% Discharge Cap. Retention	NMC 532 Cathode	Superior Graphite Anode	% of Original Capacity at 2C	Short Label
1	124	DP-12(B):6(T)	DP-1506T(B):1520P(T)	59%	C3/A4
2	386	6	1520P	55%	C1/A7
3	370	6	DP-1506T(B):1520P(T)	54%	C1/A4
4	472	DP-12(B):6(T)	1520P/1506T Mix	53%	C3/A2
5	235	6	1520P/1506T Mix	53%	C1/A2
6	124	DP-12(B):6(T)	DP-1520P(B):1506T(T)	53%	C3/A3
7	15	DP-12(B):6(T)	SP-1506T(B):1520P(T)	51%	C3/A6
8	185	6	DP-1520P(B):1506T(T)	50%	C1/A3
9	81	6	SP-1506T(B):1520P(T)	49%	C1/A6
10	385	DP-12(B):6(T)	1520P	47%	C3/A7
11	185	DP-12(B):6(T)	1506T	47%	C3/A1
12	Not Yet Made	6/12 blend	DP-1520P(B):1506T(T)	46%	C2/A3
13	Not Yet Made	6/12 blend	DP-1506T(B):1520P(T)	46%	C2/A4
14	Not Yet Made	SP-12(B):6(T)	DP-1520P(B):1506T(T)	45%	C5/A3
15	13	DP-12(B):6(T)	SP-1520P(B):1506T(T)	44%	C3/A5
16	On Test: @ Cycle 46 - 92.4%	6/12 blend	1520P/1506T Mix	43%	C2/A2
17	Not Yet Made	6/12 blend	SP-1506T(B):1520P(T)	43%	C2/A6
18	226	6/12 blend	1520P	41%	C2/A7
19	On Test: @ Cycle 46 - 91.8%	DP-6(B):12(T)	DP-1506T(B):1520P(T)	41%	C4/A4
20	474	6	1506T	40%	C1/A1
21	309	6	SP-1520P(B):1506T(T)	40%	C1/A5
22	138	SP-6(B):12(T)	DP-1506T(B):1520P(T)	40%	C6/A4
23	131	SP-12(B):6(T)	1520P	40%	C5/A7
24	Not Yet Made	SP-12(B):6(T)	1506T	40%	C5/A1
25	On Test: @ Cycle 47 - 86.7%	DP-6(B):12(T)	DP-1520P(B):1506T(T)	39%	C4/A3
26	Not Yet Made	6/12 blend	SP-1520P(B):1506T(T)	39%	C2/A5
27	272	SP-6(B):12(T)	DP-1520P(B):1506T(T)	38%	C6/A3
28	On Test: @ Cycle 45 - 93.7%	6/12 blend	1506T	38%	C2/A1
29	Not Yet Made	SP-12(B):6(T)	DP-1506T(B):1520P(T)	37%	C5/A4
30	On Test: 25 - already hit 80%	DP-6(B):12(T)	SP-1506T(B):1520P(T)	36%	C4/A6
31	229	DP-6(B):12(T)	1506T	35%	C4/A1
32	Not Yet Made	SP-12(B):6(T)	1520P/1506T Mix	35%	C5/A2
33	Not Yet Made	SP-12(B):6(T)	SP-1506T(B):1520P(T)	35%	C5/A6
34	Not Yet Made	SP-12(B):6(T)	SP-1520P(B):1506T(T)	33%	C5/A5
35		12	DP-1506T(B):1520P(T)	33%	C7/A4
36		12	DP-1520P(B):1506T(T)	32%	C7/A3
37	320	SP-6(B):12(T)	1520P/1506T Mix	31%	C6/A2
38	275	SP-6(B):12(T)	1506T	31%	C6/A1
39		12	1520P/1506T Mix	31%	C7/A2
40	244	DP-6(B):12(T)	1520P/1506T Mix	30%	C4/A2
41		12	1520P	30%	C7/A7
42	288	SP-6(B):12(T)	1520P	29%	C6/A7
43	295	DP-6(B):12(T)	1520P	28%	C4/A7
44	38	SP-6(B):12(T)	SP-1506T(B):1520P(T)	28%	C6/A6
45		12	1506T	28%	C7/A1
46		12	SP-1506T(B):1520P(T)	28%	C7/A6
47	On Test: @ Cycle 48 - 85.3%	DP-6(B):12(T)	SP-1520P(B):1506T(T)	27%	C4/A5
48	231	SP-6(B):12(T)	SP-1520P(B):1506T(T)	26%	C6/A5
49		12	SP-1520P(B):1506T(T)	25%	C7/A5

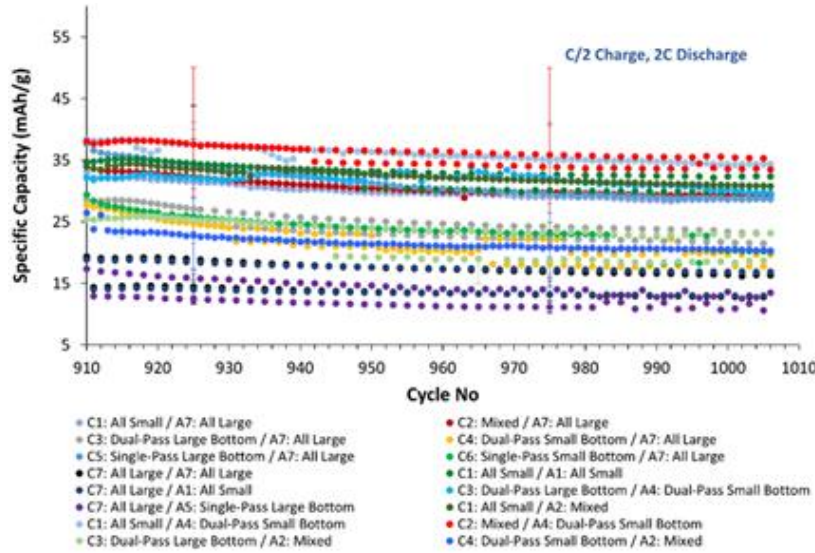
Pouch cells cycled at C/2 charge, 2C discharge completed 1000 cycles of testing, and the results are shown below in Figure 9 (a) with an expanded scale for the last 100 cycles shown in Figure 9 (b) for clarity. HPPC was performed every 100 cycles. Data is an average of three cells for each combination, and each error bar is an average of the standard deviation for those 50 cycles. All of the cells showed significant capacity loss in the first 100 cycles, but after this point the capacity fade is relatively minor. Table VI lists the final capacities (averaged over the last 50 cycles) for each cell combination in order of best to worst. The capacities range



from 35 mAh/g for the C2: Mixed / C4: Dual-Pass Small Bottom combination down to 12 mAh/g for the C7: All large / A5: Single-Pass Large Bottom combination. The rate performance results for these cell combinations are also listed in Table VI for comparison. Combinations that are good for rate performance were not necessarily expected to be good for cycle life, but the same trends generally hold for both data sets. Cells made with small particle cathodes (C1) or two-layer cathodes with large particles on the bottom (C3) generally perform better, while cells made with large particle cathodes (C7) or two-layer cathodes with small particles on the bottom (C4 and C6) generally perform worse. However, a notable difference between the two data sets comes from cells made with the mixed particle cathode (C2). When paired with the appropriate anode (A4 dual-pass with small particles on bottom), this combination has the highest capacity after 1000 cycles at 2C (~35% retention). However, the 2C capacity retention from the rate performance tests (46%) was not one of the best. It is important to note that even though this top cell combination only reaches 35 mAh/g after 1000 cycles (there is definite room for improvement), these results demonstrate that particle size and cell architecture do make a difference for high-rate cycle life performance.



(a)



(b)

Figure 9. Cycle life performance of single-layer pouch cells made with selected anode/cathode combinations. Charge C/2, discharge 2C for (a) 1000 cycles and (b) last 100 cycles shown for clarity. Source: ORNL

Table VI. Comparison of Cycle Life and Rate Performance Results for the 16 Selected Anode/Cathode Combinations

Cycle Life (2C Discharge)			Rate Performance (2C Discharge)	
Cell Combinations	Final Capacity (Avg of Last 50 Cycles) (mAh/g)	Final Capacity Retention (Avg of Last 50 Cycles)	Cell Combination	Capacity Retention at 2C
C2 / A4	35	35%	C2 / A4	90%
C1 / A4	35	34%	C1 / A4	88%
C1 / A2	31	34%	C1 / A2	84%
C1 / A1	31	36%	C3 / A2	83%
C3 / A4	31	30%	C1 / A4	83%
C2 / A7	30	33%	C3 / A4	80%
C5 / A7	29	32%	C3 / A4	76%
C1 / A7	29	29%	C2 / A4	71%
C3 / A7	23	22%	C1 / A4	69%
C6 / A7	22	31%	C5 / A4	66%
C3 / A2	21	23%	C4 / A4	63%
C4 / A2	21	26%	C3 / A4	60%
C4 / A7	20	28%	C6 / A4	59%
C7 / A1	15	23%	C4 / A4	58%
C7 / A7	15	21%	C7 / A4	58%
C7 / A5	12	22%	C7 / A4	56%

**Note:** Results are listed in order of best to worst performance. **Blue:** The final capacity of each cell combination is an average of the last 50 cycles of the 1000 cycle test. **Green:** The capacity retention at 2C is taken from the rate performance results.

The same trends were observed in slower cycling (C/2 charge, C/2 discharge) data as in the faster 2C cycling data. Again, the best-performing cells are generally those made with small particle cathodes (C1) or two-layer cathodes with large particles on the bottom (C3), while the worst-performing cells are generally made with large particle cathodes (C7) or two-layer cathodes with small particles on the bottom (C4 and C6). As with the high-rate cycling data, cells made with a mixed particle cathode (C2) and a two-layer anode with small particles on the bottom (A4) show the best capacity retention (~90%) after 300 cycles. Conversely, cells made with a large particle cathode (C7) and a small particle anode (A1) show the worst capacity retention after 400 cycles (~35%) (although the cell-to-cell variation for this combination is quite high). Overall, many of the cell combinations demonstrate excellent capacity retention after 300-500 cycles, but there are clear differences between them, confirming that particle size and electrode structure can be tuned to improve cycle life. Particle size and porosity grading both make a substantial difference in capacity retention at 2C discharge rates. The best long-term performer was a mixed particle cathode with a dual-pass, small-particle bottom layer. The worst performer was the all-large particle cathode paired with a single-pass, large-particle bottom layer.

Figure 10 shows the long-term cycle life (C/2 charge, C/2 discharge) of single-layer pouch cells made with structured cathodes and anodes. Data is an average of 3 cells for each combination, and each error bar is an average of the standard deviation for those 50 cycles. HPPC was performed every 100 cycles. The general trends appear to be similar to those observed in the rate performance testing, with the all small particle cathode baseline (Cathode #1) and the dual-pass cathode containing large particles on the bottom (Cathode #3) performing well and the all large particle baseline (Cathode #7) and the dual-pass cathode containing small particles on the bottom (Cathode #4) performing worse. The best overall combination was the all small particle baseline cathode (Cathode #1) with the mixed particle anode (Anode #2), which showed 82% capacity retention after 950 cycles. Interestingly, the mixed particle cathode (Cathode #2) paired with the dual-pass

anode containing small particles on the bottom (Anode #4) also showed very good capacity retention (83% after 830 cycles), even though it was not one of the top performing combinations in the rate performance testing.

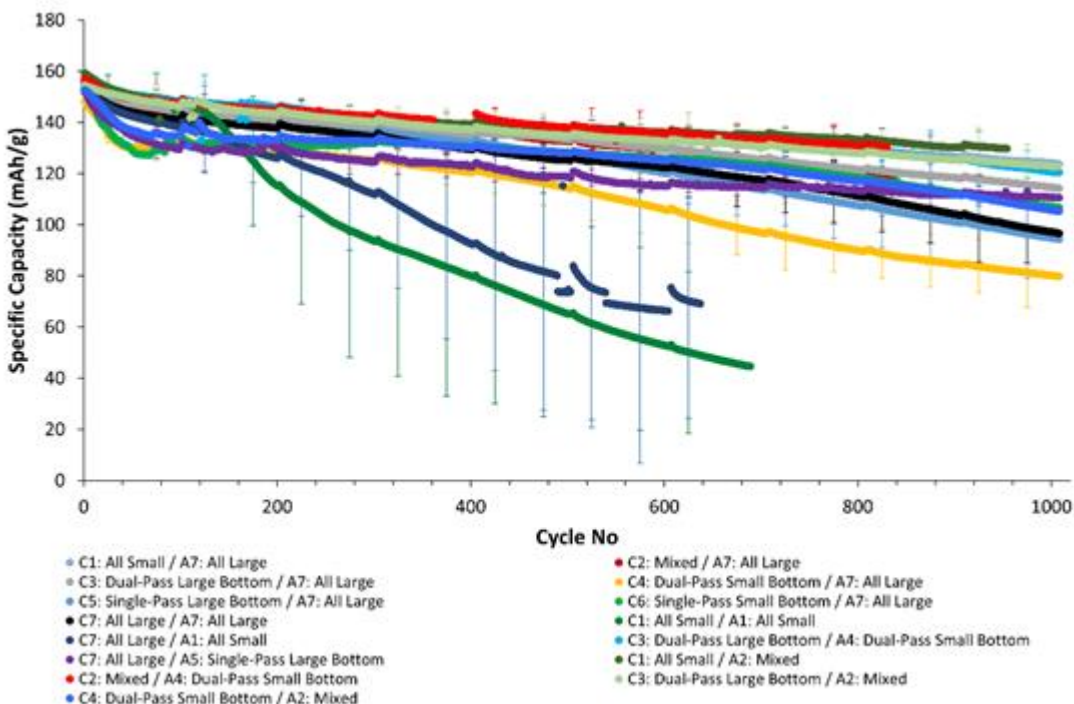


Figure 10. Cycle life performance of single-layer pouch cells made with selected anode/cathode combinations at a charge C/2 and discharge C/2. Source: ORNL

## National Renewable Energy Laboratory

### Metrology and Quality Control

NREL received structured anode sheet samples from ORNL and created a continuous web from these sheet samples. The samples were run on the NREL web-line using the porosity diagnostic equipment setup previously used for cathodes. Data was taken with both mid-IR and far-IR cameras to understand potential differences due to surface structure/emissivity. Replicate runs were made to understand repeatability. Data analysis of this experiment was initiated and continued throughout FY 2018. Also, an initial assessment of the suitability of the current material model to the structured anodes was made. It was determined that the current model should be suitable.

Previous studies measured the emissivity and thermal conductivity of battery electrodes, based on our observations of the surfaces and spectral response differences of two IR cameras of different wavelength range. The measurements were expected to help understand the differences in measured thermal response and to be an input to the thermal model used as part of the in-line porosity diagnostic. Feasibility studies for both measurements were made. For thermal conductivity, a pulsed light source method was explored, using a system that is used at NREL for other battery materials. In the end, measurement results were two orders of magnitude different than the expected values, and it was determined that the method is likely not valid for the very thin electrode materials of interest. For emissivity, a Nicolet Fourier Transform Infrared (FTIR) apparatus with a Pike integrating sphere was used. These measurements were successful, and provided repeatable quantification of expected results, i.e. cathodes showed higher emissivity than anodes. Figure 11 shows the results for three repeated measurements of a cathode sample (616AMO4) and an anode sample (A12). The

results also showed that the emissivities were relatively constant within the wavelength ranges of the two IR cameras used for the in-line porosity measurements.

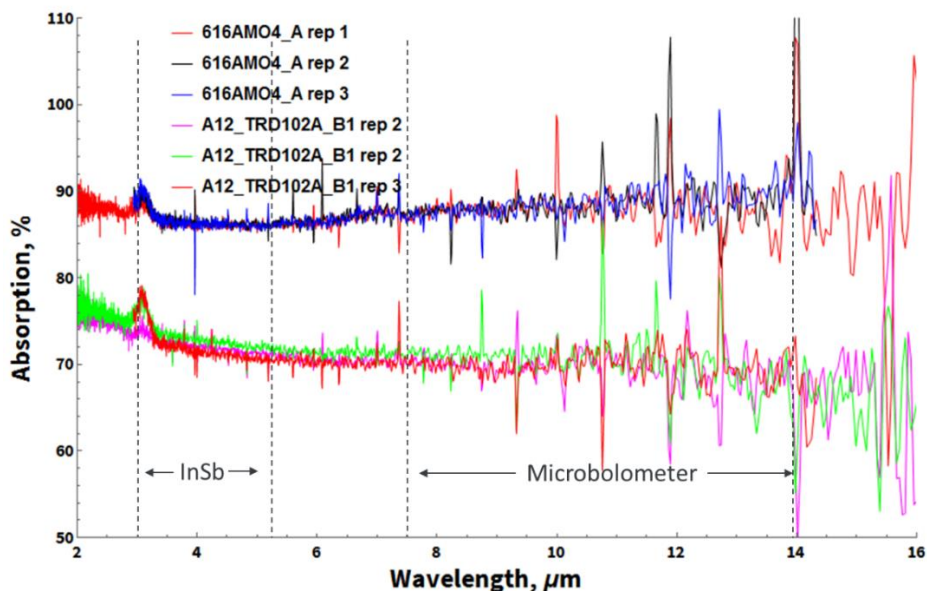


Figure 11. Emissivity measurements for cathode and anode made via FTIR, showing fairly constant emissivity within the spectral ranges of the two IR cameras (InSb in the mid-IR range and microbolometer in the far-IR range). Source: NREL

In addition, analysis was completed on the in-line porosity data taken on the NREL web-line of the structured anode samples coated and provided by ORNL. The analysis methodology from past studies was augmented by the evaluation of the entire thermal profile in the down-web direction (not just the peak temperature). By this method, differences were seen between the indium antimonide (InSb) (3-5  $\mu\text{m}$  wavelength) and microbolometer (7-13  $\mu\text{m}$  wavelength) IR cameras used. Interestingly, it was observed that the response using the microbolometer camera appeared to be correlated with the size of the particles in the top layer of the structured electrode as shown in Figure 12. This could be a novel capability for the industry. While the provided series of samples did not actually have a designed variation of porosity (and thus the main measurement response across the sample set was about the same), the new analysis did identify possible additional useful measurements for a future study. The thermal model was also evaluated for these samples and was largely consistent with the measured data.

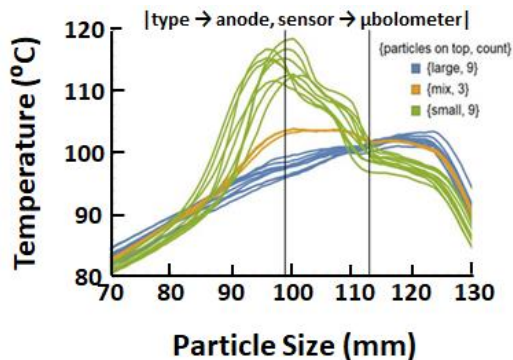


Figure 12. Thermal response from structured anodes using the microbolometer camera showing a dependence on the particle size in the top layer of the electrode. Source: NREL



In addition to the battery-electrode porosity diagnostic described above, an experimental study was performed to understand if there is a correlation between optical-wavelength diffuse reflectance and electrode loading. We used a professional desktop scanner for this scoping study. The specimen set included 18 LIB cathodes fabricated at ORNL. The cathode set consisted of coatings made using single pass, two sequential passes, and two simultaneous (dual slot) coatings. Most cathode coatings had small (standard) particles on the coating surface. In case of two cathodes (616AMO3 and 716AMO5) large particles were present on the coating surface. Each sample was scanned two times. The images were processed using a two-step automatic script developed in Wolfram Mathematica. First a mask was defined to localize an electrode within an image, then a calculation of mean intensity was performed. Regarding experimental noise, it was found that, on average, the difference between two reflectance intensity measurements on the same sample was 0.5%. Moreover, we also noticed that six samples of NMC- N-Methyl-2-pyrrolidone (NMP) 2764 electrodes, which were tested a total of 12 times, yielded results with a standard deviation of 0.6%. These noise metrics indicate that the measurement method was very reproducible. The intensity results from all cathode images is shown in Figure 13 below and were grouped based on cathode age (old and new), and size of top layer particles (small and large). It was found that the old and large-surface-particle groups are significantly darker than the new cathodes with small particles. The difference is about 9.3%, which is significantly larger than the error estimates given above. The old cathodes are the ones fabricated before October 2016. NREL and ORNL will further explore the causes of this apparent correlation. With regard to the original intent of the effort, however, no statistically significant correlations could be observed between the diffuse reflectance signal and the sample loading for these particular materials.

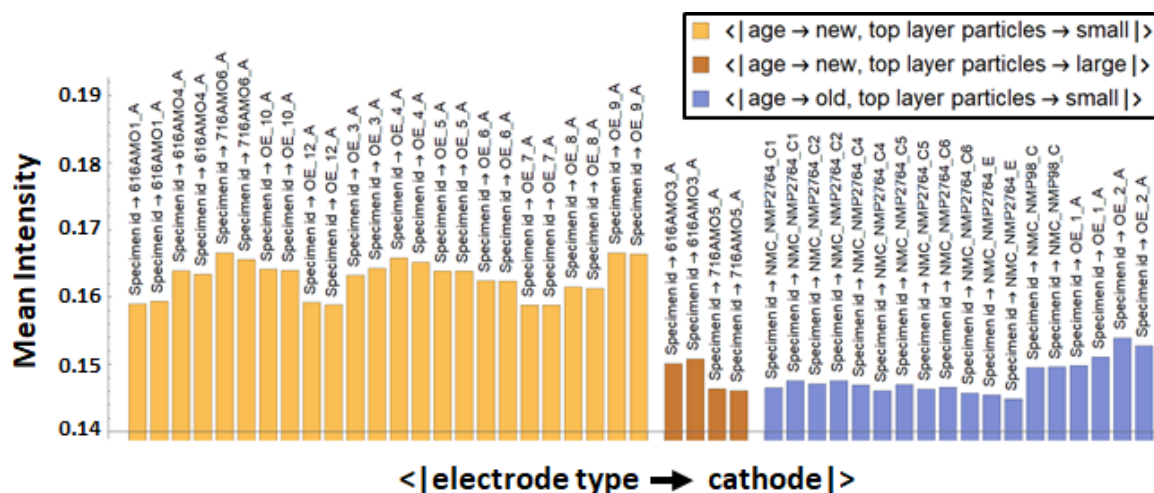


Figure 13. Diffuse reflectance intensity signal for battery cathode samples fabricated at ORNL showing confounded dependence on date of coating and size of particles on top surface of coating. Source: NREL

## Fuel Cell Study

### National Renewable Energy Laboratory

NREL is the lead laboratory for the Fuel Cell Study effort. The objective of the study is to explore phase-separation and other single-coating-layer methodologies to achieve GDEs with an ionomer-rich surface (IRS). To meet this objective, NREL will study and characterize relevant electrode ink parameters, study the impact of coating parameters and types on GDE morphology, fabricate MEAs from coated GDEs, test the MEAs performance, interact with ORNL on ink studies, dual-slot coating and high-resolution electron microscopy, interact with ANL for the USAXS and x-ray computed tomography (XCT) advanced characterizations, and interact with LBNL to initiate the development of a mechanistic fuel-cell-electrode ink rheology model.

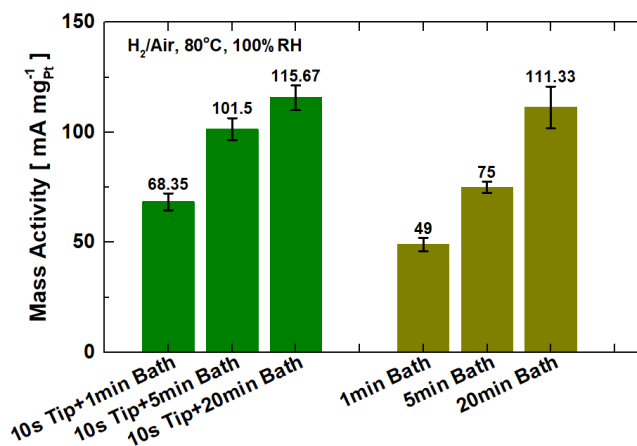
## Data Informatics

This task includes coordination of data for fabrication, characterization, and in situ testing from initial hand- and R2R-coated samples of the IRS GDE study. Specific information was shared with project partners on fuel cell ink formulation, electrode fabrication, and in situ testing.

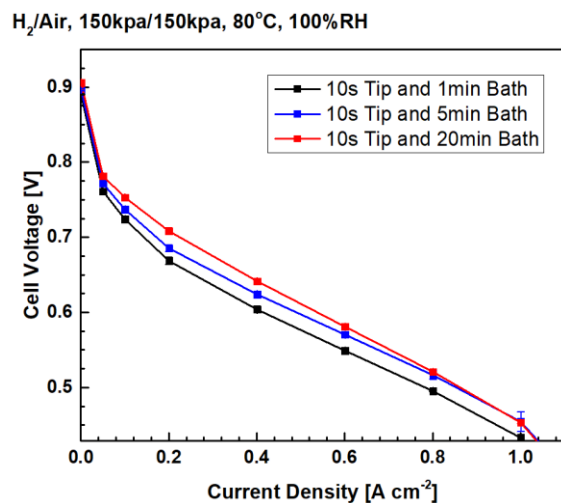
### Studies Involving Cutting Edge Coating and Deposition Science and Fabrication, and In Situ Testing of Prototype Components and Devices

#### Studies Exploring the Impact of Ink Dispersing Method and Duration

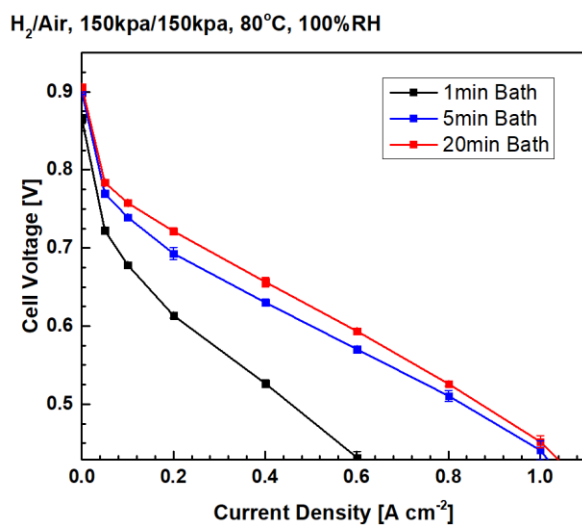
In situ testing of MEAs was performed to correlate with the USAXS ink measurements made by ANL at the APS as a function of dispersing conditions (i.e. tip and/or bath sonication). The in situ testing results showed that insufficient sonication could not effectively break down the initially large agglomerates, leading to poor three-phase boundaries and poor mass activity. Figure 14 (a) shows the results for mass activity, where mass activity increases as the bath time increases from 1 min to 20 min, both with and without a 10s tip sonication. Figure 14 (b) and Figure 14 (c) show similar trends via polarization data for tip+bath and bath sonication, respectively. As sonication times increase, the cell potential increases, especially at higher current densities. Appropriate tip sonication can break down large agglomerates (see Figure 14 (a) for e.g. 20 min bath and 10s tip + 20 min bath), but excessive sonication can decrease electrochemical surface area as detailed in Table VII (e.g. 5 min and 20 min tip).



(a)



(b)



(c)

Figure 14. Sonication results: (a) MEA mass activity for tip+bath and bath-only sonicated inks, (b) H<sub>2</sub>/air polarization for tip+bath MEAs and c) bath-only MEAs. Source: NREL

Table VII. Summary of In Situ Data Exploring Tip and Bath Sonication Impact on MEA Performance

Ink Processing Condition	Loading (mg Pt/cm <sup>2</sup> )	Electrochemical Surface Activity (m <sup>2</sup> /g Pt)	Mass Activity (A/g Pt)	Specific Activity (μA/cm <sup>2</sup> Pt)	Tafel Slope (mV/dec)
10s Tip & 1 min Bath	0.0357	48.52	68.35	140.84	64.7
10s Tip & 5 min Bath	0.0363	49.01	101.5	207.05	66
10s Tip & 20 min Bath	0.0367	49.08	115.67	235.27	65.9
1 min Bath	0.0383	47.9	49	102.04	72
5 min Bath	0.0373	48.49	75	155.3	64.6
20 min Bath	0.037	42.76	111.33	225/35	61.4
1 min Tip	0.035	48.48	75.33	155.45	66.7
5 min Tip	0.0367	44.19	61.67	139.22	72.5
20 min Tip	0.0383	42.76	75	175.09	65.4

To further explore the impact of dispersion parameters, a unique NREL-developed limiting current analysis and electrochemical impedance spectroscopy (EIS) were performed to understand the oxygen transport (non-Fickian) resistance and bulk catalyst layer resistances in these MEAs. Figure 15 (a) shows that the optimal case has a lower resistance than a comparator (1 min bath) case, which experienced ineffective dispersion and thus had larger catalyst agglomerates. Similarly, the EIS measurements given in Figure 15 (b) showed that the 10s tip + 20 min bath and 20 min bath cases had the least resistance (highest slope at low frequency), whereas the 20 min tip sonication showed higher resistance due to excessive sonication which detached Pt from the carbon support. The 1 min bath had the highest resistance, as noted previously, due to insufficient dispersion. We also received corresponding electron microscopy from our collaborators at the Colorado School of Mines. As shown in Figure 16 (a), the best-case 10s tip + 20 min bath had a well dispersed catalyst, whereas the 1 min bath case (Figure 16 (b)) showed highly agglomerated catalyst particles. The USAXS and in situ data was shared and evaluated with ANL.

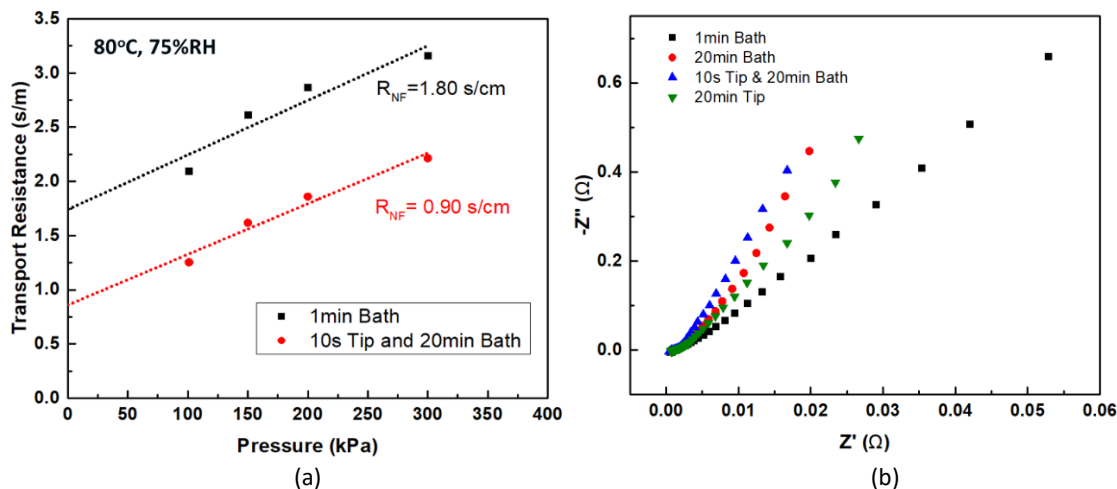


Figure 15. Effects of sonication on (a) non-Fickian oxygen transport resistance and (b) EIS of MEAs made with electrode inks of various sonication. Source: NREL

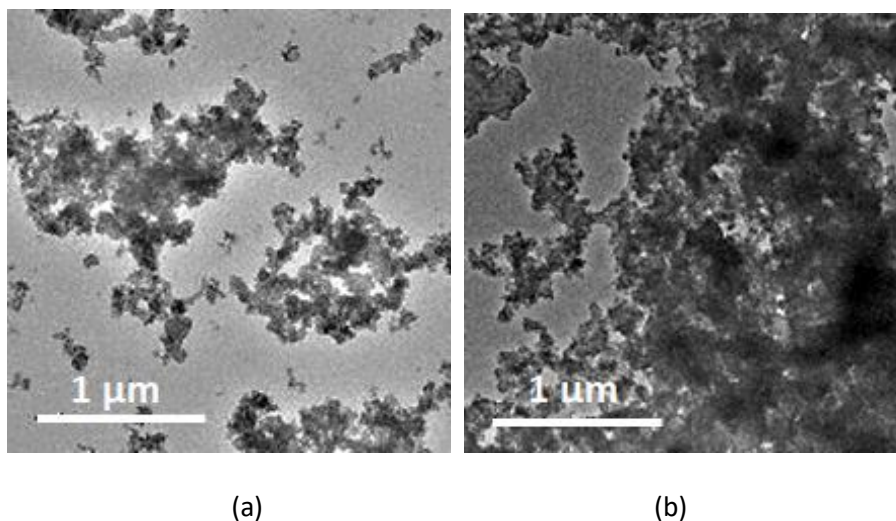


Figure 16. Electron microscopy for (a) the 10s tip + 20 min bath case and (b) the 1 min bath case. Source: Colorado School of Mines



## Studies of Solvent Blends with Water

A rheology study was performed motivated by the observed differences in surface ionomer content (as measured by Kelvin Probe), XCT profiles of ionomer distribution at ANL, and in situ performance between rod- and R2R-coated electrodes with water-rich versus 1-propanol-rich inks. Regardless of solvent formulation, the catalyst particles show agglomeration when there is no ionomer in the dispersion. In a 1-propanol-rich solvent, the addition of ionomer causes an increase in viscosity. In contrast, in a water-rich solvent the addition of ionomer decreases the viscosity and there is a transition from shear-thinning to Newtonian. This implies that in the case of the water-rich solvent the ionomer adsorbs to the surface the catalyst particles and stabilizes them against agglomeration. Conversely, in the 1-propanol-rich solvent, the ionomer does not adsorb to the catalyst but is dispersed in the solvent, so agglomeration of the catalyst is not decreased. These disparate behaviors are reflected in the distribution of ionomer in the resulting catalyst layers as measured by XCT. The electrode cast from the water-rich solvent has a more uniform distribution because the ionomer associated with the catalyst particle is not mobile during the drying of the electrode. In the electrode cast from the 1-propanol-rich dispersion the ionomer is not associated with the catalyst, so it is more mobile and can redistribute itself within the electrode as it dries.

In a second study, several alcohol-water solvent blends were explored to determine the impact on controlling the ionomer distribution in the catalyst layer. The best solvents for dispersing the ionomer, as determined by observing the Tyndall Effect using a red laser, were those with the OH group on one end (e.g. 1-propanol) or opposing ends (e.g. 1,4-butanol) of the molecule, as opposed to in the center (e.g. tert-butanol). We also performed rheology measurements on these ionomer dispersions to understand the impact of the different blends on agglomeration and coatability. As shown in Figure 17, a fairly wide range of viscosity was observed in the different dispersions. This could suggest the use of other more complex blends to modify rheology as desired. Using the solvent blends with the best dispersing properties, we coated GDEs. The Kelvin Probe method was used to compare the amount of surface ionomer, as shown in Figure 18, and differences were observed. However, none of the alternate-solvent GDEs had improved performance over the original materials (a 1-propanol-water mixture). Based on our studies, exploration of higher drying temperatures, higher ionomer content, and intermediate-evaporation-temperature alcohols is warranted to seek further improvements in ionomer distribution and performance.

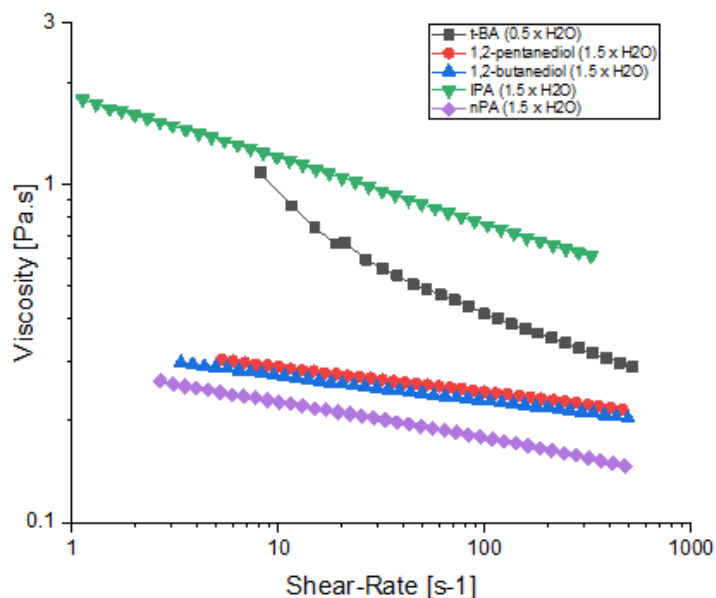


Figure 17. Rheology of water-alcohol blends. Source: NREL

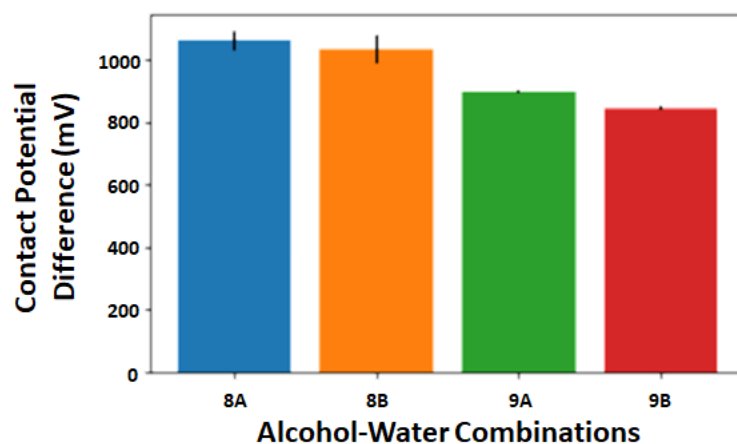


Figure 18. Kelvin probe measurements of selected GDE samples. 8A: 1,2-butanediol-water, alcohol rich; 8B: 1,2-butanediol-water, water rich; 9A 1,2-pentanediol-water, alcohol rich; 8B: 1,2-pentanediol-water, water rich. Source: NREL

MEAs were fabricated from this series of GDEs coated with inks having different alcohols and different alcohol-water mixtures. While no improvements in total cell polarization were observed compared to the original 1-propanol-water inks, we did observe interesting trends, such as that, for alcohol-water inks where the alcohol has a higher boiling point than water, water-rich inks lead to higher ionomer-surface content (as shown in Figure 18 above) and higher mass activity (as shown below in Figure 19 for the example of 1,2-pentanediol-water mixtures). Figure 19 also appears to suggest that a drying temperature of 80°C leads to better performance than 180°C. Based on previous studies, exploration of intermediate drying temperatures may provide optimization.

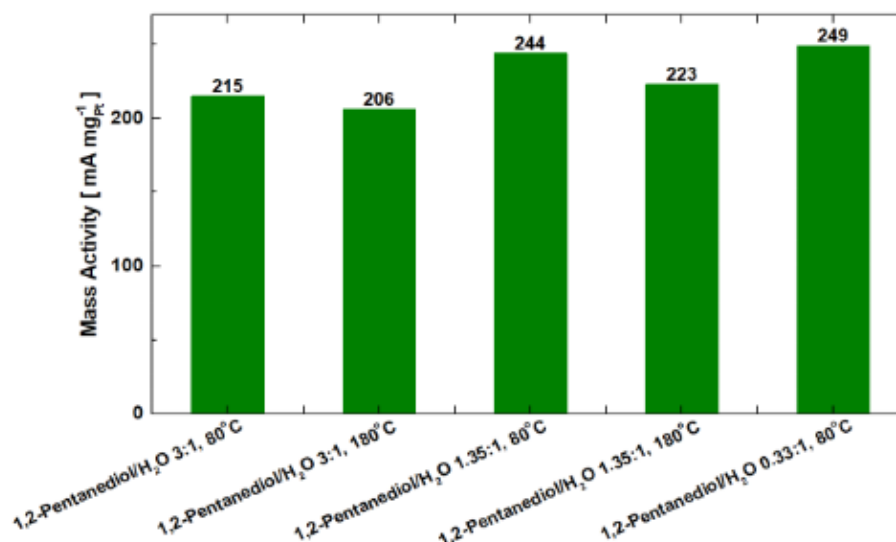


Figure 19. In situ mass activity measurements for 1,2-pentanediol-water mixtures of different ratio. Source: NREL

#### Ionomer Rich Surface Gas Diffusion Electrode Coating and Characterization Studies

Kelvin Probe measurements, which provide a rapid indication of the amount of ionomer on the surface of the electrode, were made of previously R2R-coated GDEs. Figure 20 shows these results, which largely replicated the results from the rod-coated samples, i.e. higher ionomer-to-carbon (I:C) ratio and higher fraction of water in the water/n-propanol solvent mixture lead to higher surface content of ionomer. All samples fabricated at 1 m/min web speed and 80°C oven temperature.

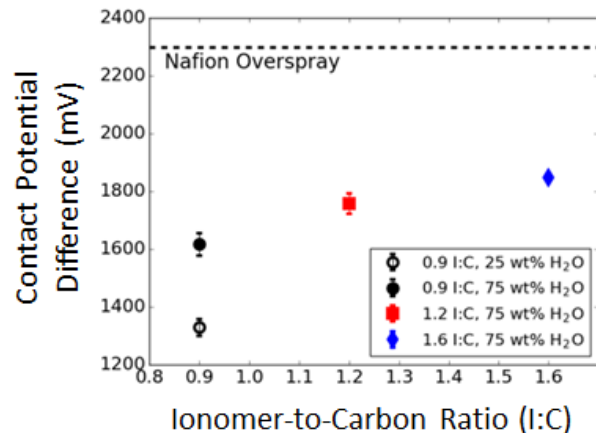


Figure 20. Kelvin Probe measurements of four R2R-coated GDEs for contact potential difference versus the ionomer to carbon (I:C) ratio. Source: NREL

In a related study, calibration relationships were developed for the Kelvin Probe method of determining ionomer surface content. As shown in Figure 21, we observed a reasonably consistent slope of the contact potential difference data from Kelvin Probe to the I:C ratio in the ink for several catalysts (standard platinum on high surface carbon (Pt/HSC) from TANAKA Kikinzoku Kogyo Co.), and two Pt group metal-free catalysts from Pajarito Powders. However, the intercept is different for the different catalysts, indicating that the technique likely needs a separate calibration for each catalyst type.

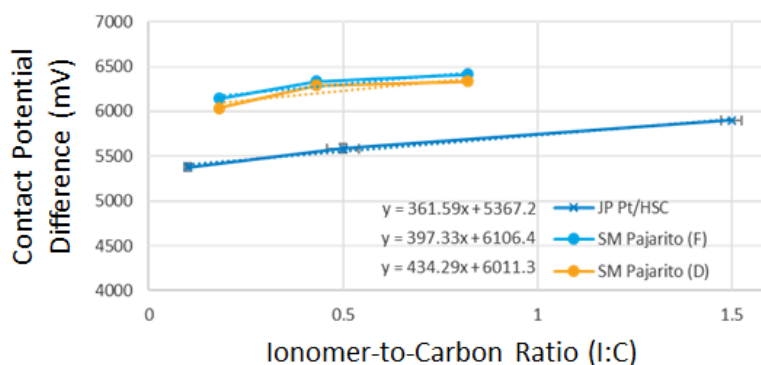


Figure 21. Kelvin Probe calibration data for three catalyst systems showing similar slope but different intercept for each catalyst. Source: NREL

In situ testing was performed on this same set of R2R-coated IRS GDEs, to validate if higher performance resulted from the electrodes for which the Kelvin Probe measurements indicated had higher surface ionomer content. Figure 22 (a) shows hydrogen/air polarization curves and Figure 22 (b) shows mass activity as a function of cathode proton resistance. These results confirm the trends observed in the rod-coated samples, i.e. that electrodes with higher surface content of ionomer perform better than those with lower levels.

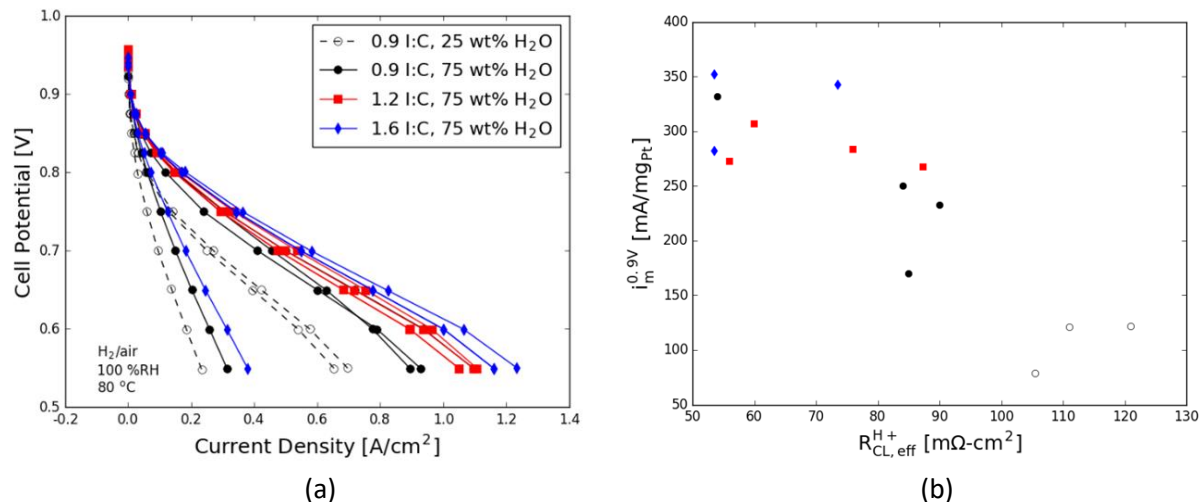


Figure 22. In situ testing results of fabricated MEAs with R2R-coated GDEs: (a) hydrogen/air polarization curves and (b) mass activity as a function of catalyst layer protonic resistance. Source: NREL

R2R coated GDEs were observed to have comparable mass activity to the spray-coated baseline as illustrated in Figure 23 (a) but initially did not match the baseline for high current density performance as shown by Figure 23 (b). To further explore this effect, we calculated the non-Fickian oxygen transport resistance for these electrodes. Table VIII shows that the R2R-coated electrode that performs the best (“1.6 I:C. 75 wt% H<sub>2</sub>O”) has the lowest transport resistance. However, this value is still slightly higher than state-of-the-art electrodes.

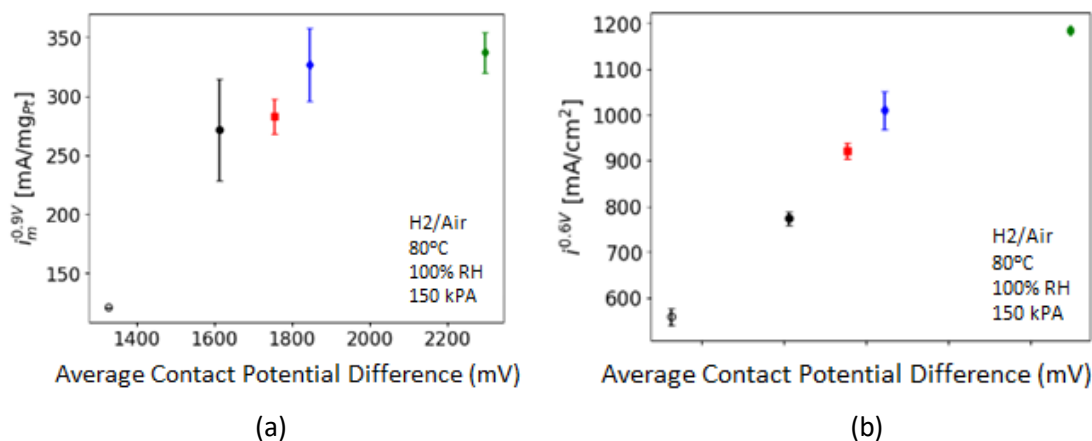


Figure 23. R2R-coated GDEs: (a) mass activity and (b) specific activity (high current density) as a function of contact potential difference compared to the sprayed baseline (using the same legend as shown in Figure 22 (a)). Source: NREL

**Table VIII. Calculated Non-Fickian O<sub>2</sub> Transport Resistance in R2R-Coated GDEs**

Catalyst-Coated Diffusion Media	Non-Fickian O <sub>2</sub> Resistance (s/cm)
0.9I:C, 25 wt% H <sub>2</sub> O	1.013
0.9I:C, 75 wt% H <sub>2</sub> O	0.719
1.2I:C, 75 wt% H <sub>2</sub> O	0.676
1.6I:C, 75 wt% H <sub>2</sub> O	0.381

In coordination with the R2R coating and in situ testing, ANL performed advanced x-ray characterization studies of inks and electrodes at ANL's APS included USAXS on catalyst-ionomer inks, providing us detailed information about the structure, tortuosity and ionomer distribution of these IRS GDEs. Again, in a very insightful result, the XCT ionomer profiles showed that the electrodes with the highest surface ionomer content as measured by Kelvin Probe and also the highest in situ performance indeed had a gradient of ionomer through the thickness of the electrode and the highest surface content. This was a strong validation of the phase-segregation approach to achieving ionomer-rich surface electrodes.

In associated work, a methodology and associated open-source code were developed to perform equivalent-circuit modeling of fuel cell MEA EIS data. The method is useful to evaluate EIS data of the resistances in the various MEA layers as a function of the various ink and process parameters, including protonic resistance of the cathode. The open-source code was published to the community via NREL's website.

### Gas Diffusion Layer Roughness Study

We explored the impact of the roughness of the diffusion media microporous layer (MPL) surface on performance. This study was envisioned based on efforts to understand the function of the ionomer overlayer in the GDEs. At least in part, the function appears to be the formation of a more integral physical interface between the membrane and electrode, which enhances proton transport. Thus, it seemed reasonable that a smoother MPL surface – the substrate for the electrode – could also have positive impact on this interface. Two diffusion media were used, Freudenberg H23C8 and SGL Group 29BC, the former material having a much smoother MPL coating surface than the latter. MEAs were fabricated from the R2R-coated IRS GDEs and in situ testing was performed to quantify performance. As shown in Figure 24, the MEAs made from the diffusion media with smoother MPL surface (H23C8) had improved performance compared to the rougher diffusion media and were able to achieve this performance with less overspray (one pass as opposed to two). However, these improvements did not obviate the need for the overspray altogether.

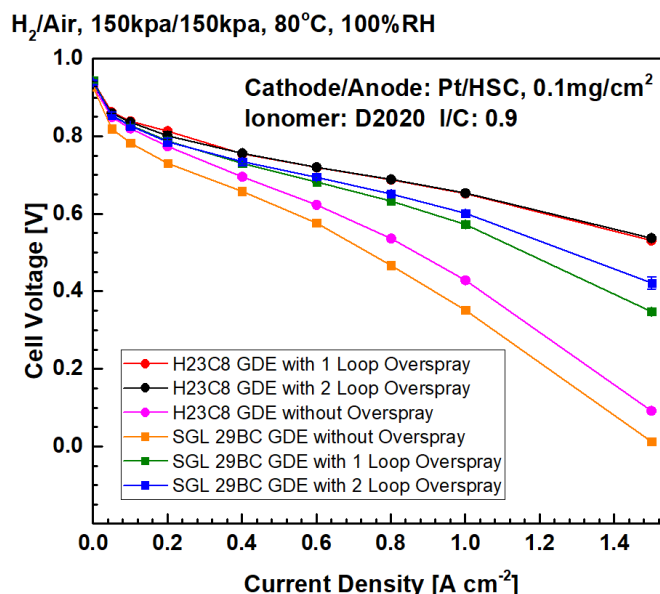


Figure 24. Polarization curves comparing MEAs fabricated from R2R-coated IRS GDEs on diffusion media with differing MPL roughness (note that GDEs on H23C8 diffusion media with 1 and 2 loops of overspray had identical performance). Source: NREL

### In-line NDE and Metrology Development

Leveraging metrology-development work supported by the FCTO, NREL demonstrated an in-line technique to perform real-time imaging of membrane thickness using hyperspectral imaging. In addition to ion-conducting membranes, we demonstrated the technique using commercially-available polyethylene terephthalate films of different thickness. Polyethylene terephthalate films are used across a breadth of different applications, suggesting potential usefulness of the technique to many applications in the AMO space. While the demonstration was successful, additional work is required to optimize device configuration, physical resolution, and data processing algorithms for the phase transformation of interference fringes and peak-fitting. Going forward, as has been noted in other discussions, this technique is ripe for implementation in an integrated process-metrology-characterization-device testing-machine learning-process feedback development platform, the concepts and application of which we understand to be of high interest to AMO, given outputs of a workshop on machine learning.

### Argonne National Laboratory

ANL supported the Fuel Cell Study by providing characterization of catalyst-ionomer-solvent inks, studying ink synthesis parameters, such as sonication time and energy and characterization of the nano and microstructure of electrodes. All tasks were completed, and milestones met on schedule.

### USAXS Characterizations of Inks Under Different Ultrasonic and Shear Mixing Conditions

Analyses were performed using x-ray scattering to analyze the ink agglomerate structure during mixing. X-ray scattering experiments were conducted to compare horn sonication, bath sonication, and ball milling for two catalyst types (Pt/HSC) and Pt on a lower surface area Vulcan carbon (Pt/Vu) and to determine the effect of platinum, solvent, and the I:C ratio. These different sonication methods were tested to determine the effects of electrode composition and to determine the optimum ink processing time to be used for electrode fabrication.

X-ray scattering experiments were conducted to compare homogenization and ball milling for two catalyst types, Pt/HSC and Pt/Vu to determine the effect of platinum, solvent, and I:C ratio. The inks were ball milled for 14 hrs and then USAXS was performed on the static inks. The inks were also homogenized with a Turrax mixer and USAXS was performed during the 25-min homogenization.

The primary carbon particles in the fuel cell catalysts form aggregates that are slightly clustered to form agglomerates with sizes as large as hundreds of microns. The USAXS and small-angle x-ray scattering (SAXS) profiles for Vu and HSC-based inks after ball milling are shown in Figure 25 (a) and Figure 25 (b) respectively. The curves at low  $q$ ,  $<0.002\text{\AA}^{-1}$ , represent scattering from the carbon agglomerates whose radii are beyond the measuring range of the USAXS.

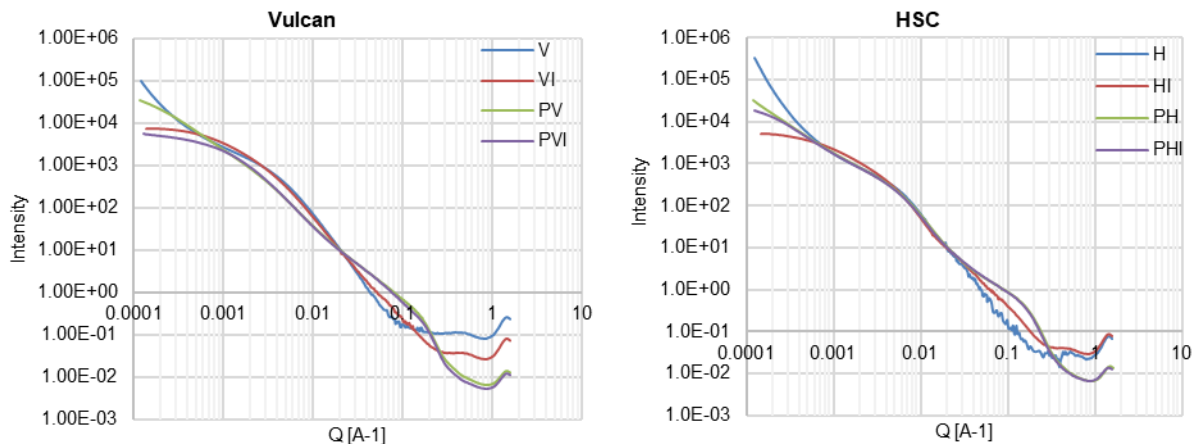


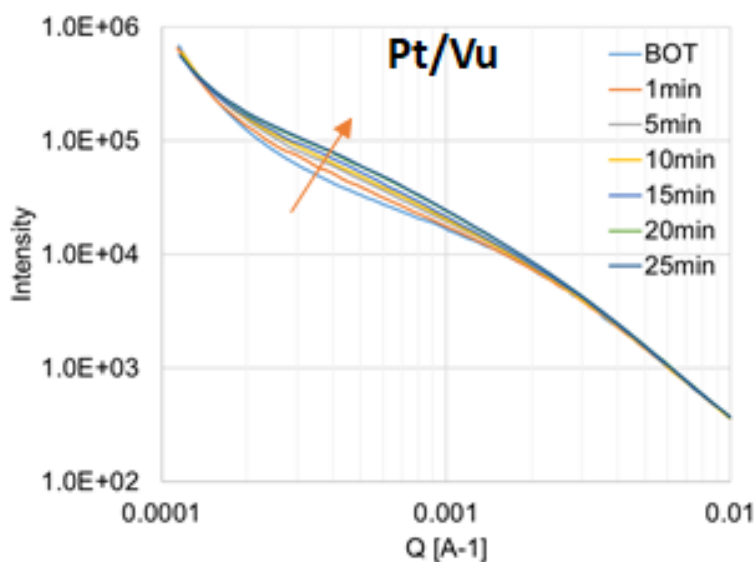
Figure 25. USAXS-SAXS scattering of (a) Vu and (b) HSC-based inks plotted on log-log scales. The intensity data sets have been offset to overlap at  $q=0.02\text{ \AA}^{-1}$  on the y-axis for clarity. Source: ANL

As shown in Table IX, the power law slope fittings to the USAXS data can be related to the level of carbon agglomeration. A decrease in the power law slope is generally correlated with a lower extent of agglomeration with the aggregates being more uniformly distributed throughout the ink. The USAXS results are in good agreement with NREL's viscosity data; i.e., (1) the HSC dispersion has a higher viscosity compared to Vu due to a higher internal porosity, (2) the presence of strongly charged Pt catalyst reduces the ink viscosity for both HSC and Vu, (3) the addition of ionomer to the carbon dispersions, without Pt, decreases the viscosity by electrostatic stabilization of the particles, and (4) Pt/Vu dispersions with Pt/Vu ionomer show similar rheology to the Vu ionomer while Pt/HSC dispersions shows an increased viscosity with ionomer addition possibly due to the heterogeneous ionomer distribution on Pt/HSC compared to Pt/Vu.

Table IX. Power-Law Fitting of Slopes of USAXS Data in the Low Q Region ( $<0.002 \text{ \AA}^{-1}$ )

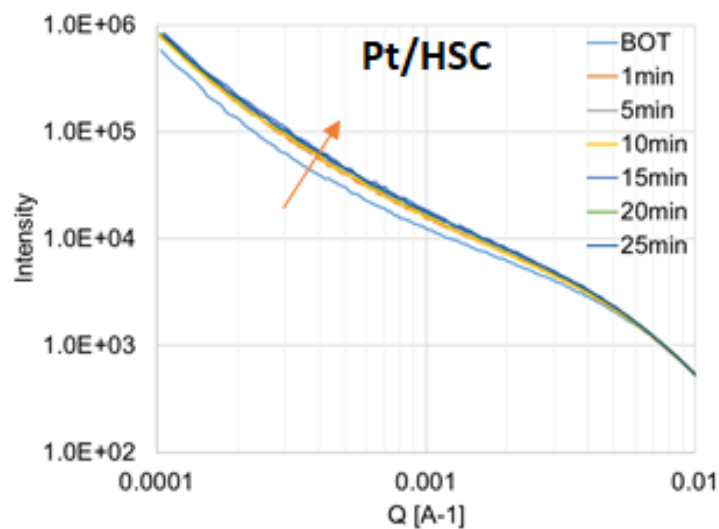
Sample name	Power law slope
Vulcan - 0 I:C (V)	3.25
Vulcan - 0.5 I:C (VI)	1.48
Pt/Vulcan - 0 I:C (PV)	2.94
Pt/Vulcan - 0.5 I:C (PVI)	1.53
HSC - 0 I:C (H)	4.82
HSC - 0.9 I:C (HI)	1.37
Pt/HSC - 0 I:C (PH)	3.75
Pt/HSC - 0.9 I:C (PHI)	2.90

The two inks with ionomer were stirred with a Turrax homogenizer while being chilled in an ice bath. The USAXS profiles for the Pt/Vu and for the Pt/HSC ionomer-solvent-inks after mixing are shown in Figure 26 (a) and Figure 26 (b) respectively. The data shows that the Turrax mixer is highly effective in breaking up the agglomerates in the concentrated Pt/HSC ink while it is less effective at breaking up the agglomerates in the Pt/Vu, which has larger carbon particles.



(a)

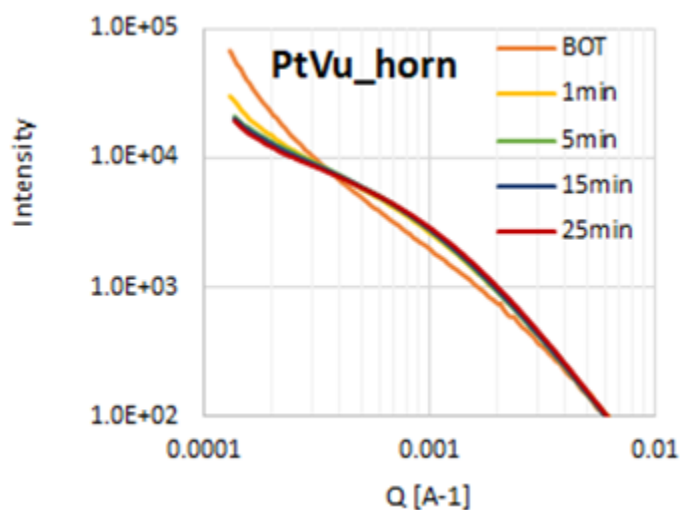




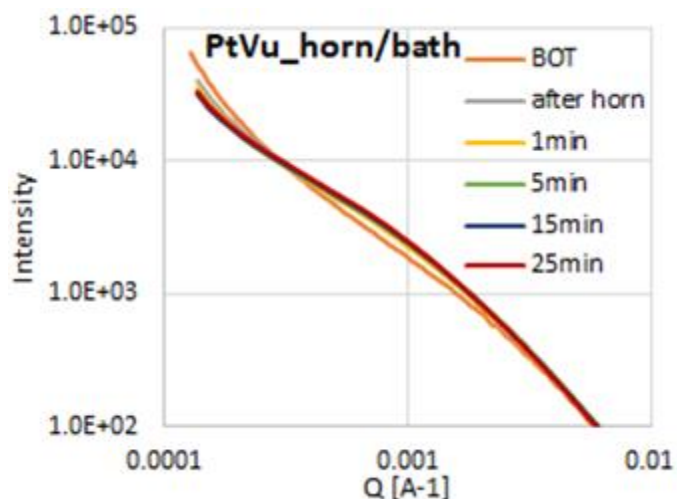
(b)

Figure 26. USAXS profiles for catalyst (a) Pt/Vu and (b) Pt/HSC-ionomer-solvent inks with the Turrax mixer as a function of homogenization time. Source: ANL

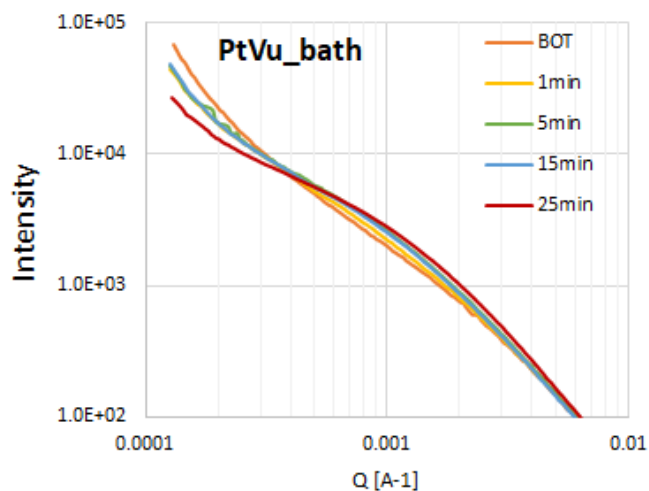
X-ray scattering can be categorized into different size regimes covering the agglomerates and aggregates (using USAXS), the catalyst particles (using SAXS), and the interatomic spacing (using wide-angle x-ray scattering (WAXS)). The USAXS regions of the scattering curves for three different mixing methods of horn, horn/bath, and bath for the Pt/Vu material are shown in Figure 27 (a), (b) and (c) respectively.



(a)



(b)



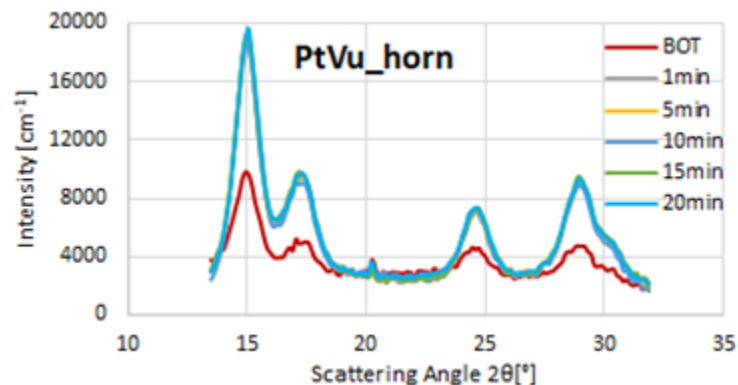
(c)

Figure 27. USAXS profiles for Pt/Vu-ionomer-solvent inks as a function of sonication time for (a) horn, (b) horn/bath and (c) bath sonication methods. Source: ANL

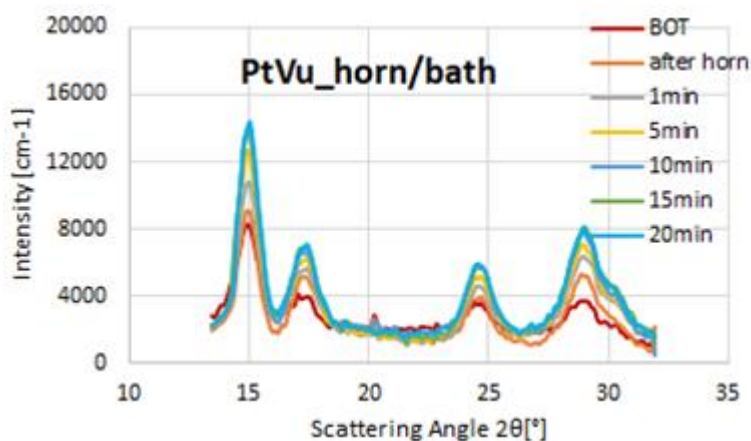
As shown in Figure 27, the scattering intensities in the intermediate  $Q$  region (aggregate region) increases with sonication time and the slope in the low  $Q$  region, which is proportional to the number of agglomerates, decreases. The scattering intensity in the aggregate region increases due to the agglomerates breaking up into aggregates with a wide size distribution. The abrupt change in the scattering occurred after only 10 s and up to 1 min of horn sonication (Figure 27 (a)) with only subtle changes after that shows that horn sonication is very effective at breaking up agglomerates.

The WAXS data corresponding with the USAXS data shown in Figure 27 are shown in Figure 28 (a), (b) and (c) respectively. The increase in the intensity of the scattering peaks from the various atomic planes in Pt is caused by the break-up of the agglomerates causing more of the Pt to be exposed to the x-ray beam. NREL observed that the Pt electrochemically-active surface area decreases with horn sonication time and stays constant with 10 s of horn sonication followed by the bath, and slightly increases with the bath sonication time indicating Pt particles may be increased due to either agglomeration of Pt particles on the carbon support with excessive sonication or dislodging of Pt particles from the carbon support. The WAXS and SAXS data show

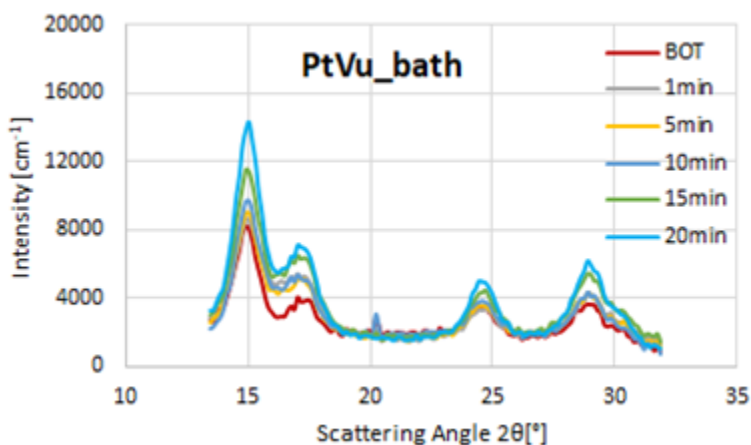
that the Pt particles are not increasing substantially in size with sonication, pointing the latter mechanism for Pt electrochemically-active surface area loss. The NREL electrochemically-active surface area data combined with the scattering data shown in Figure 27 and Figure 28 show that the 10 min horn sonication is sufficient to break-up the carbon agglomerates without causing undue degradation of the catalyst by detaching the particles from the support.



(a)



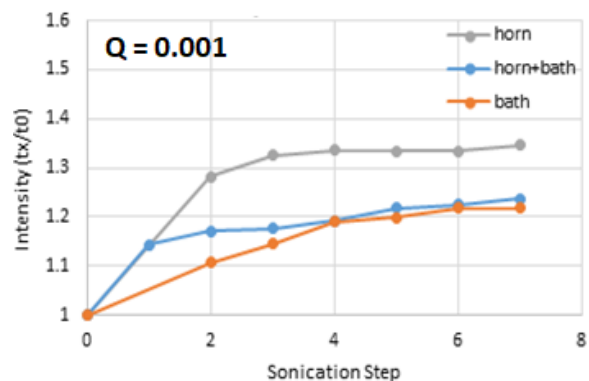
(b)



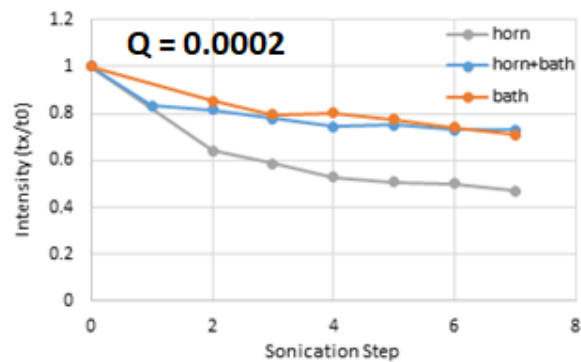
(c)

Figure 28. WAXS profiles for Pt/Vu-ionomer-solvent inks as a function of sonication time for (a) horn, (b) horn/bath and (c) bath sonication methods. Source: ANL

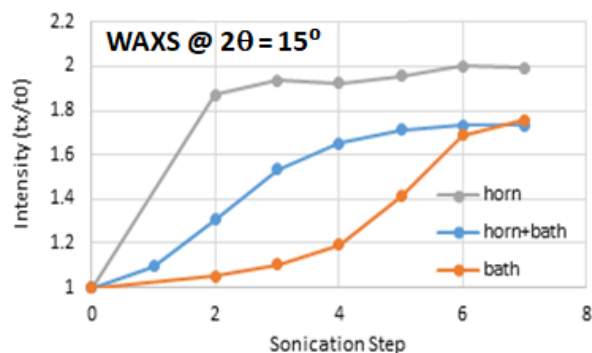
Sonication data was taken at seven times: after the horn and at 1, 5, 10, 5, 20, and 25 minute intervals. The intensities in the aggregate, agglomerate, and WAXS regions as a function of sonication step for the Pt/Vu catalyst ink USAXS are shown in Figure 29 (a), (b) and (c) respectively. The intensity level of peak at Pt (111) represents Pt particle dispersion rate of the ink during sonication. The WAXS results correspond with NREL's performance data: appropriate sonication breaks down large agglomerates without dislodging Pt particles from the support while excessive sonication decreases the electrochemically-active surface area do to this detachment process.



(a)



(b)



(c)

Figure 29. Scattering intensity in (a) aggregate, (b) agglomerate, and (c) wide-angle scattering regions for Pt/Vu as a function of sonication step. Source: ANL

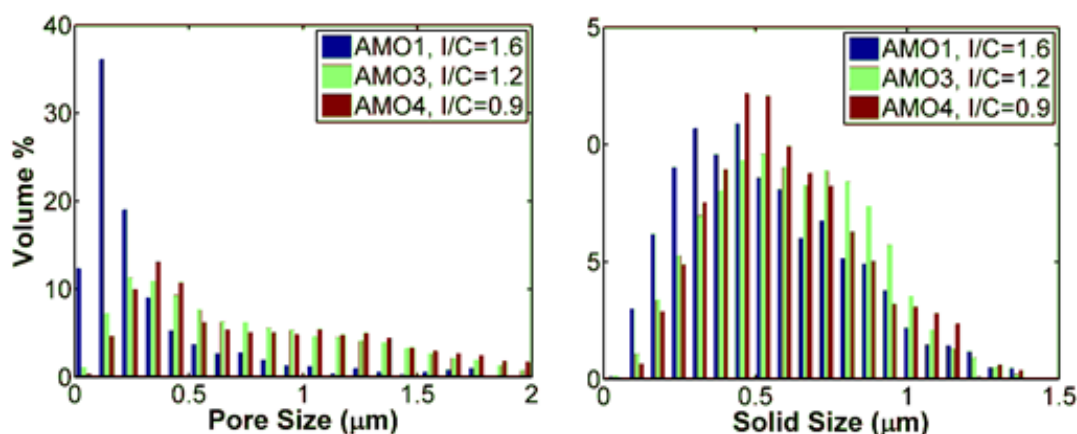
The key outcomes of these experiments were as follows:

- Just 10 s of horn sonication is effective at breaking up agglomerates to approximately 50% (on average) and after 25 mins of bath sonication.
- Addition of ionomer to Vu and Pt/Vu improves the carbon agglomerate break up; intermediate I:C ratios (e.g., 0.5) are generally most effective at quickly breaking up agglomerates.
- Presence of Pt also decreases extent of agglomeration of Vu carbon in inks
- Addition of ionomer to HSC and presence of Pt on HSC decrease agglomeration, whereas ionomer has relatively little effect on Pt/HSC ink agglomeration for ball-milled inks.
- While NREL typically ball mills their inks for >8 hrs, it was determined that only 3 hrs are necessary to break up the agglomerates in the inks to their final state.

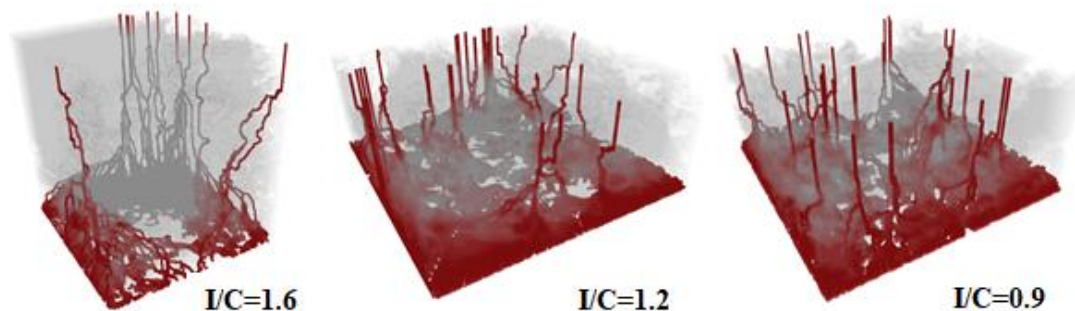
### Nano- and/or Micro- X-Ray Tomography of Coated Electrodes

Nine GDE and MEA samples were received from NREL and prepared for x-ray nano-tomography (nano-CT). The samples analyzed were GDEs with I:C ratios of 0.9, 1.2, and 1.6. Testing of these samples was to determine if an ionomer-rich layer could be formed at the interface between the GDE and the membrane by increasing the ionomer content in the ink rather than by the additional manufacturing step of spraying an overlayer of ionomer on the GDE.

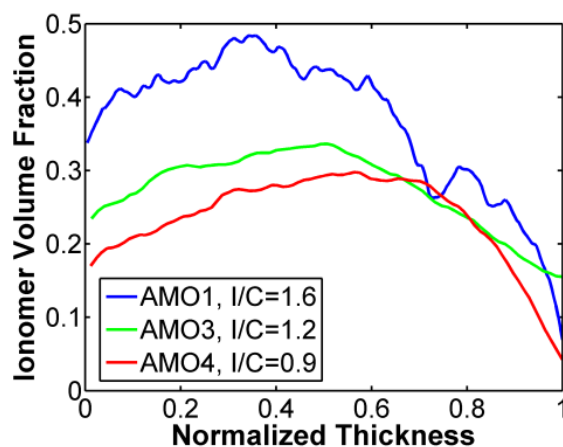
The pore and solid size distributions from the nano-CT data are shown in Figure 30 (a), which shows that the solid sizes (agglomerates) are larger and more uniform than the pores and the distribution of the solid sizes is slightly smaller for the sample with the I:C of 1.6. The sample with I:C of 1.6 is also dense and has very tiny pores compared to the other samples. The images in Figure 30 (b) show the shortest path tortuosity through the three electrodes and illustrate that reactant transport is mostly through the big cracks for the high ionomer content sample and less uniformly distributed than that for the other two samples. The ionomer volume fraction analysis results are given in Figure 30 (c) and show that the I:C of 1.6 sample does indeed have a higher ionomer volume fraction at the interface with the membrane, which is the structure NREL desired for this sample. The data from the x-ray scattering and tomography experiments has provided explanations for NREL's rheology data on the catalyst-ionomer inks and of the performance data on their electrodes.



(a)



(b)



(c)

Figure 30. Analysis of GDEs for (a) pore size and solid size distributions of three NREL GDEs with I:C ratios of 1.6, 1.2, 0.9, with (b) the shortest path tortuosity of the GDEs, and for (c) ionomer volume fraction through the thickness of the GDEs (0 thickness is at the membrane interface and 1 is at the GDL interface). Source: ANL

During available periods of beam time at the APS, nano-CT measurements were made on two GDEs with I:C of 1.6 and 0.9 with different water content at 80°C and room-temperature deposition. These samples were analyzed, and thickness-dependent ionomer distribution was illustrated. Analysis of the tomography data that compares the effect of solvent content and drying temperature on the electrode microstructure was performed. Tomography data for the samples with an I:C ratio of 0.9 with 75 wt% H<sub>2</sub>O (AMO 4) and 25 wt% H<sub>2</sub>O (AMO 2) solvent content were reconstructed as shown in Figure 31. The results indicate that water content has a very significant impact on the ionomer distribution through the thickness of the electrode as illustrated in Figure 32. Low water content solvent forms a very dense layer of ionomer close to the membrane boundary.

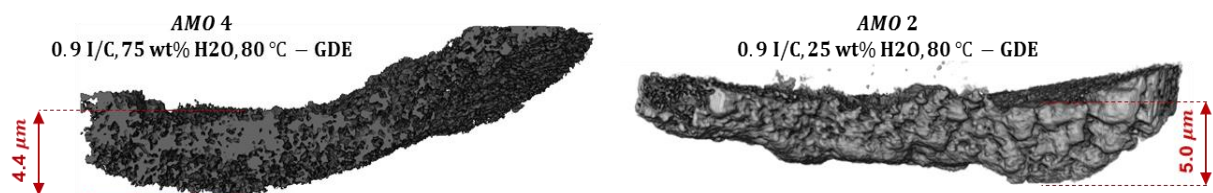


Figure 31. Reconstruction of the electrode layers with different solvent content. Source: ANL

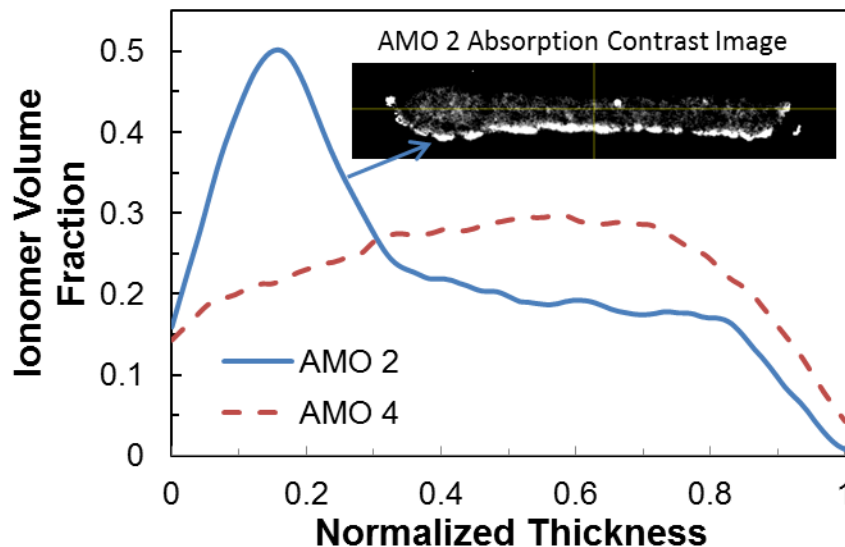


Figure 32. Ionomer distribution of the electrode layers with different solvent content. Source: ANL

We also analyzed tomography data for sample with I:C of 1.6 with two different ink drying temperatures: 80°C (AMO 1) and room temperature (AMO 6). The tomography data shows that the drying temperature affects the agglomerate and pore size distributions. Drying at room temperature results in larger agglomerates as shown by Figure 33 (a) and respectively larger pores as shown in Figure 33 (b). Consequently, it does not have a significant impact on the thickness-dependent ionomer distribution as shown in Figure 34. A technical manuscript was submitted by NREL and has been accepted by the American Chemical Society Applied Materials and Interfaces section on the rheology, performance, and X-ray scattering data.

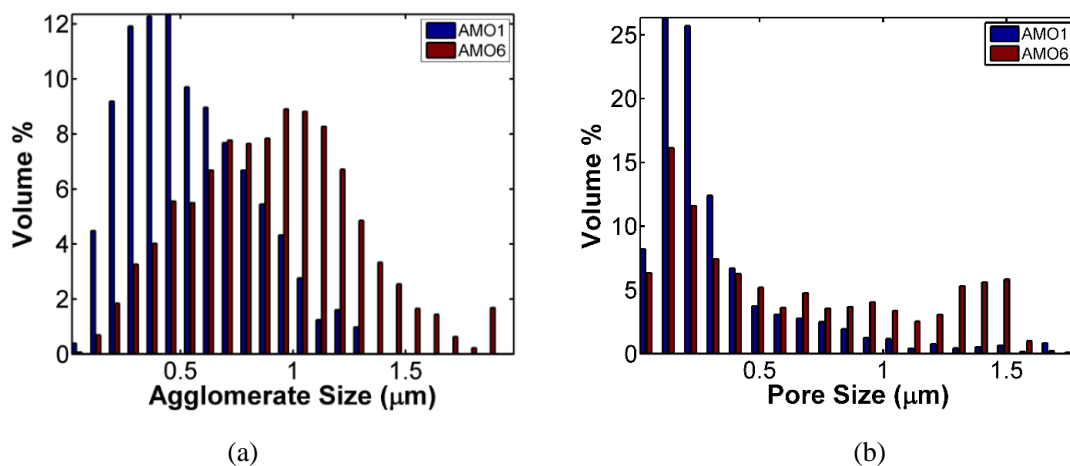


Figure 33. Tomography data for (a) agglomerate size distribution and (b) pore size distribution of electrode layers dried at different temperatures. Source: ANL



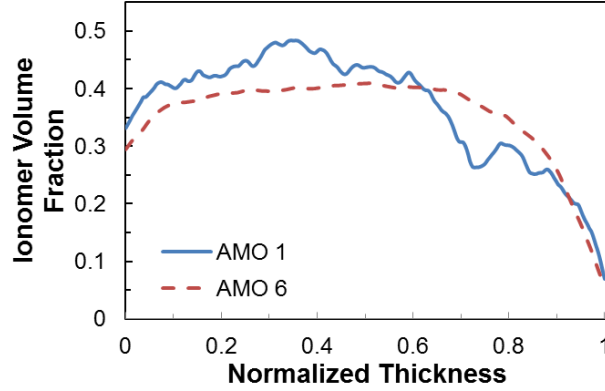


Figure 34. Ionomer distribution of the electrode layers with different drying temperature. Source: ANL

Two GDEs from NREL with I:C ratios of 1.6 and 0.9 that were fabricated at 80°C and room temperature during the ink deposition on the GDL were examined using nano-CT. The reconstructed nano-CT data from these two samples are shown in Figure 35 (a) and (b).

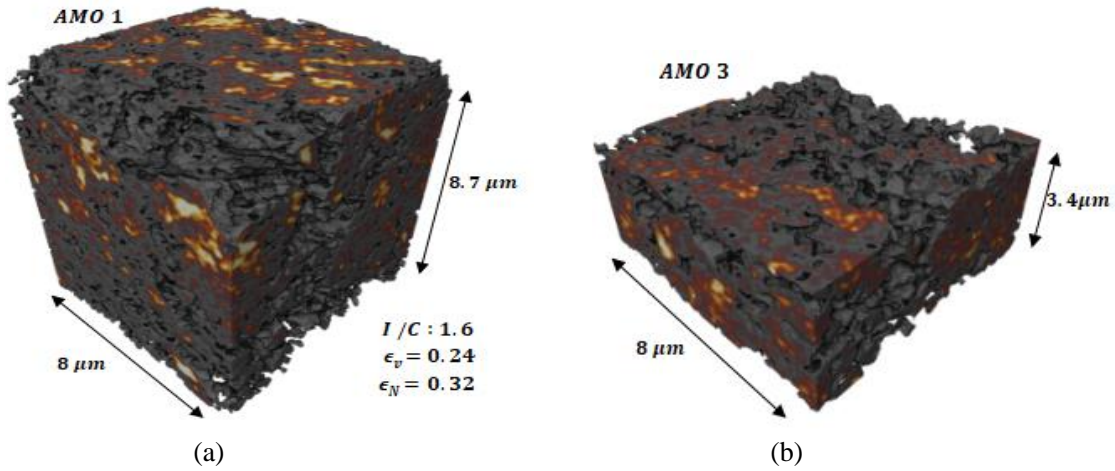


Figure 35. Reconstruction of the nano-CT data for electrode layers with different I:C ratios of (a) 1.6 and (b) 0.9 and different solvent evaporation temperatures of (a) 80°C and (b) room temperature. Source: ANL

### Analysis of the Performance of Gas Diffusion Electrodes Fabricated and Measured at NREL Using Inks of Different Compositions and Processing Conditions

We analyzed the galvanostatic impedance data for different GDE samples and concluded that the cathode catalyst layer (CCL) resistance ( $R_{\Omega}^c$ ) is 3-4 times higher than the resistance of the state-of-the-art CCMs. The inferred CCL resistance depends mainly on the I:C ratio and weakly on the drying temperature and solvent composition. A distributed oxygen-reduction reaction (ORR) kinetic model was applied to derive the reaction parameters from polarization data obtained under  $H_2/O_2$  conditions. The measured cell voltage at high current densities is lower than the values calculated assuming uniform distributions of Pt, ionomer and carbon in catalyst layer and constant  $R_{\Omega}^c$  at different current densities.

To explain the difference between the measurement and model cell voltages, we conducted three-dimensional simulations on a half cell with  $10 \mu m \times 10 \mu m$  active area and investigated the effect of CCL-membrane contact area on cell performance. The simulations shown in Figure 36 indicate that a 75% reduction in contact



area results in Pt utilization decreasing from 60% to 50%, effective membrane resistance ( $R_{\Omega}^m$ ) increasing from 35 to 95  $\text{m}\Omega\cdot\text{cm}^2$ , and CCL resistance increasing from 25 to 90  $\text{m}\Omega\cdot\text{cm}^2$ .

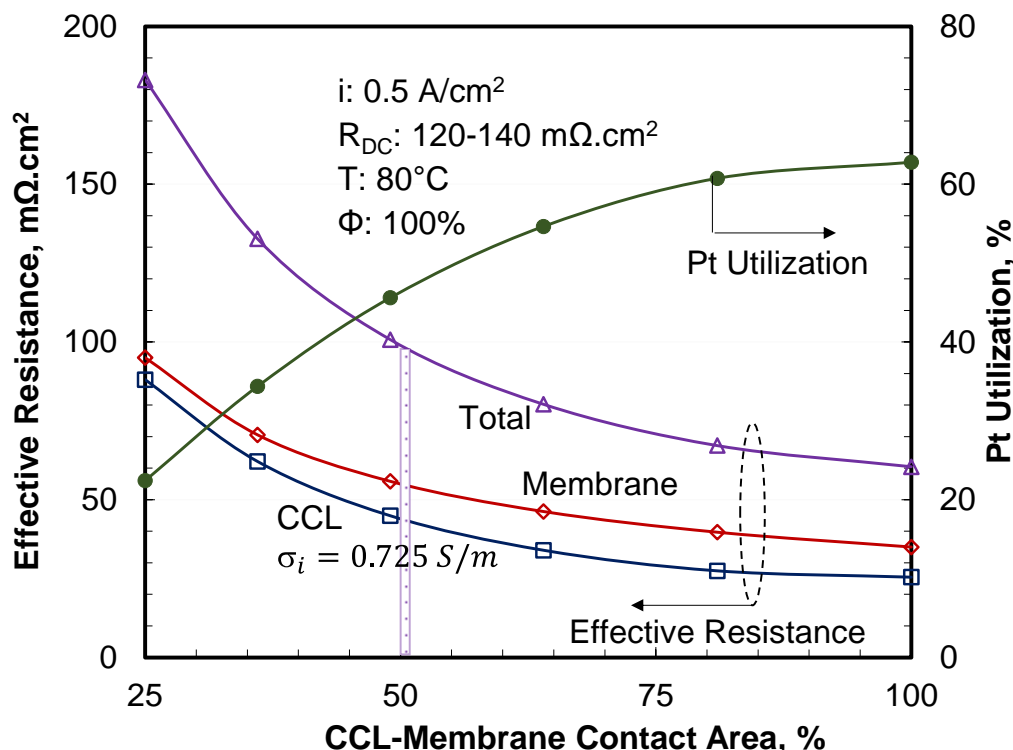


Figure 36. Effect of CCL-membrane contact area. Source: ANL

## Oak Ridge National Laboratory

The ORNL tasks for the Fuel Cell Study were to investigate low-cost methods of MEA manufacturing (slot-die) and coating electrocatalyst layers onto gas diffusion media to make GDEs, utilize R2R hot-pressing (calendering) of GDEs to PEMs to make “unitized” MEAs, and implement processes for thickness control and metrology for MEA production QC. The GDL roll, carbon black catalyst support, and Pt-supported electrocatalyst powder were received from NREL and ORNL. Microscopy support from ORNL Materials Characterization Core was obtained to verify coated microstructures. The dual slot-die coating at ORNL on GDLs with Pt to form an ionomer-rich layer for bonding to the membrane was delayed to FY19.


### Determination of Solids Loading Range for GDE Slot-Die Coating

As shown in Table X, mixing carbon black (CB) and water over a range of solids loadings up to 15 wt% with the addition of Nafion D2020 dispersion (containing both ionomer and 1-propanol) and 5-15 wt% solids is the optimum range for slot-die coating. Table XI shows a high-quality ink with 7.0 wt% solids loading and 0.9 ratio of ionomer/CB.

Table X. CB/Water Ink Quality at Nine Different Solids Loadings of CB with Constant Mixing Speed of 3500 rpm

Sample No.	Carbon Black	Water	Mixing Time (min)	Mixing Speed (rpm)	Carbon Black (wt%)	Image of Mixture
1	7925.8	44923	40	3500	15.0	
2	7928	52072	40	3500	13.2	
3	7928	72072	40	3500	9.9	
4	7928	920072	40	3500	7.9	
5	7928	102072	40	3500	7.2	
6	7928	112072	40	3500	6.6	
7	7928	122072	60	3500	6.1	
8	7928	132072	60	3500	5.7	
9	7928	142072	60	3500	5.1	

Table XI. Improvement in GDE Ink Quality at 7 wt% Solids Loading with the Addition of Nafion D2020 Dispersion Containing 1-Propanol. I:C is 0.9 and Nafion D2020 Contained 20 wt% Ionomer

Sample No.	Carbon Black (g)	Nafion D2020 (g)	Water (g)	Mixing Time (min)	Mixing Speed (rpm)	Solid Loading (%)	Mixture Image
1	1.745	7.8467	41.103	60	3500	7.0	

### **Preliminary Slot-Die Coating of SGL Group GDL 29BC With Nafion D2020 and Vu XC-72R Without Supported Pt Catalyst**

A thin (~10  $\mu\text{m}$ ) Vu XC72-R CB and Nafion D2020 layer without Pt catalyst was successfully slot-die coated onto the GDL substrate as a preliminary test. A solids percentage of ~9 wt% gave a slurry with the right viscosity for slot-die coating. The slurry formulation was as follows:

#### Ink Composition:

18.3 g Vu XC 72R

82.35 g D2020 Nafion Dispersion (20% Nafion, 46% 1-propanol, 34% de-ionized water)

281.82 g de-ionized water

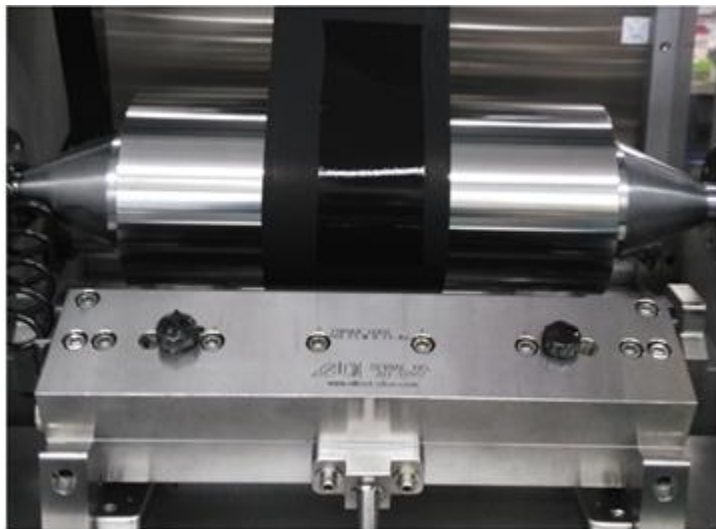
Additional 35 g of 50% de-ionized water and 50% 1-propanol

#### Solids Composition:

52.6 wt% CB

47.4 wt% Nafion

Images of the wet and dry coating are shown in Figure 37 (a) and Figure 37 (b). The coating appears smooth and uniform and demonstrates that a slurry with relatively high solids percent can be successfully slot-die coated.



(a)



(b)

Figure 37. Nafion (D2020 dispersion)/CB Vu XC-72R coating on SGL Group GDL 29BC substrate: (a) wet and (b) dry.  
Source: ORNL

### **Identification of rheological parameters for the high-solids-loading ink analysis**

A rheology study investigated slot-die coating efficacy at 5 wt%, 10 wt%, and 15 wt% solids loadings at three different mixing speeds (1000 rpm, 3500 rpm, and 6000 rpm) and three different mixing times (20 min, 40 min, and 60 min). Rheological analysis was carried out on the baseline slurry to find out the pre-shear time and soaking time to remove the shear history and regain the original structure of slurry before every analysis. Originally, a slurry pre-shear step was used for 60 seconds followed by a hold step for 30 mins prior to each subsequent analysis. This pre-shear and holding time of the slurry was arbitrary, so a document from TA Instruments was implemented instead, which had a procedure to find these values experimentally. In addition,

analysis of the pre-shear effect on the linear viscosity region was carried out, and there was a significant change in storage modulus ( $G'$ ) and loss modulus ( $G''$ ) which verified that pre-shear is necessary for better rheological measurements. An oscillation strain of 0.1% was used for further analysis, as it was in the linear viscosity region as shown by the data in Figure 38.

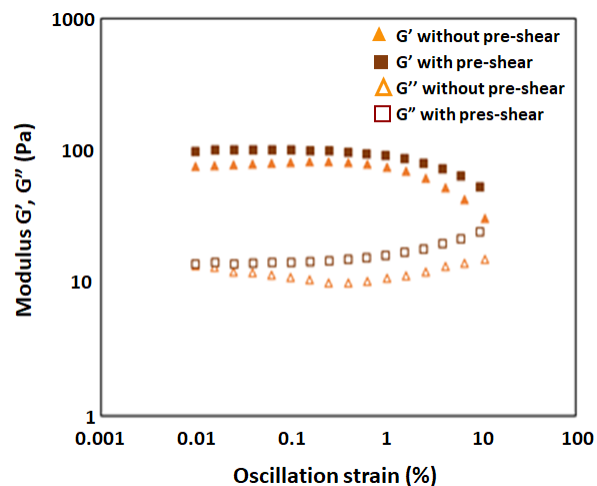


Figure 38. Analysis of the linear viscosity region using a rheometer. Source ORNL

A shear rate of 100 rad/s was identified for the shear thinning behavior of the baseline slurry for further analysis. The time sweep was carried out (in two steps) to get the resting time of the slurry for it to regain the initial structure and remove shear history. Figure 39 shows the shear thinning behavior of the baseline slurry.

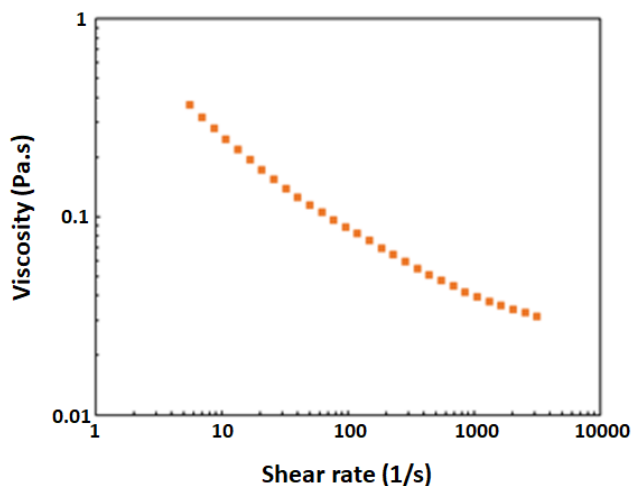


Figure 39. Shear thinning behavior of the baseline slurry. Source: ORNL

The slurry was pre-sheared with a 100 s<sup>-1</sup> shear rate (from shear thinning data) for 120 seconds. The time sweep was performed with the following operating parameters:

- Temperature: 25°C
- Duration: 3600 s
- Strain %: 0.1 (from linear viscosity region analysis)
- Frequency: 1 Hz

The effect of pre-shear time was also determined, and it was found that 120 s pre-shear time gave better rheological measurements as shown by the data in Figure 40 (a). The time required for the constant slope of the storage modulus is the amount of time that slurry need to regain the initial structure. In our case, with 120 seconds pre-shear time, the time was determined to be 945 seconds (~16 mins) as shown in Figure 40 (b). This study increased the confidence of data from the rheometer and decreased the overall analysis time.

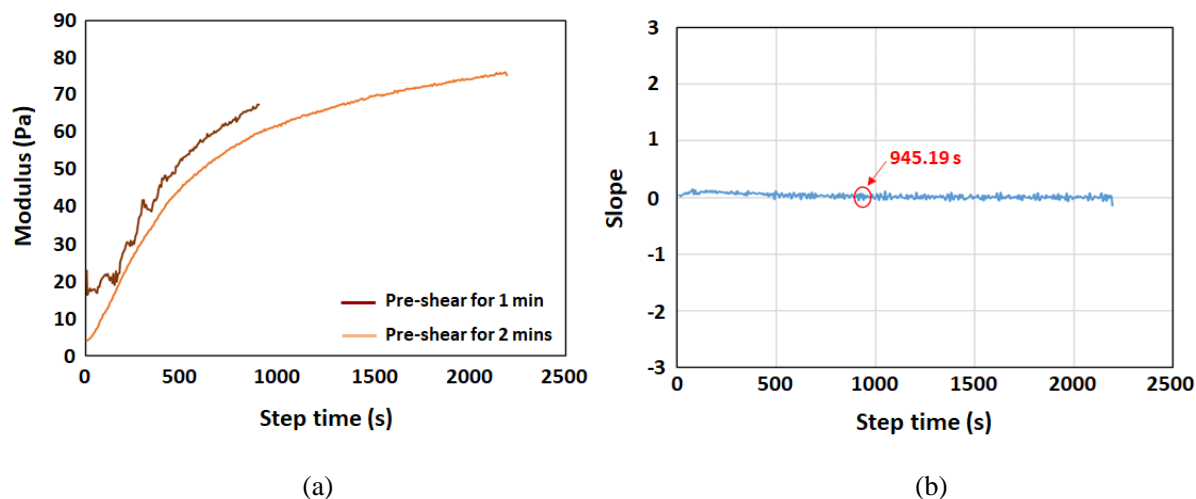


Figure 40. Analytical data for (a) the effect of pre-shear time and (b) the resting time for the slurry to regain its initial structure. Source: ORNL

### Ink optimization studies

Different formulations were analyzed with a rheometer to understand the viscoelastic properties of the slurries as a function of solid loading; i.e.:

$$\text{Solid loading} = \frac{\text{CB mass} + \text{Nafion mass}}{\text{CB mass} + \text{Nafion mass} + \text{water mass} + 1 - \text{propanol mass}}$$

Preliminary formulations of different solid loadings with variations in mixing speeds and mixing times are given in Table XII.

Table XII. Preliminary Slurry Formulations

Solid Loading (%)	Mixing Speed (rpm)	Mixing Time (mins)
4.8	2000	60
4.8	4000	60
4.8	4000	1094
9.1	2000	60
9.1	4000	60
9.1	4000	240
13	4000	60

Nafion D2020 dispersion was used and the weight fractions of Nafion, solvent and water are given in Table XIII. All slurries were mixed as a high energy shear mixture. CB was dispersed in the water first for 15 minutes and then D2020 was mixed in. The slurries showed shear thinning behavior, which means the colloidal structures align with increasing shear rate.

**Table XIII. Nafion D2020 Composition**

Component	Weight Fraction
Nafion	0.20
1-Propanol	0.46
Water	0.34

As can be seen from Figure 41 (a) and (b), better structural alignment was achieved with increased mixing speed for shear thinning, which led to an increase in viscosity. Surprisingly, a decrease in viscosity was seen with increasing solid loadings, as shown in Figure 41 (c) (not considering the ink with 4.8% solid loading, as it did not properly gel).

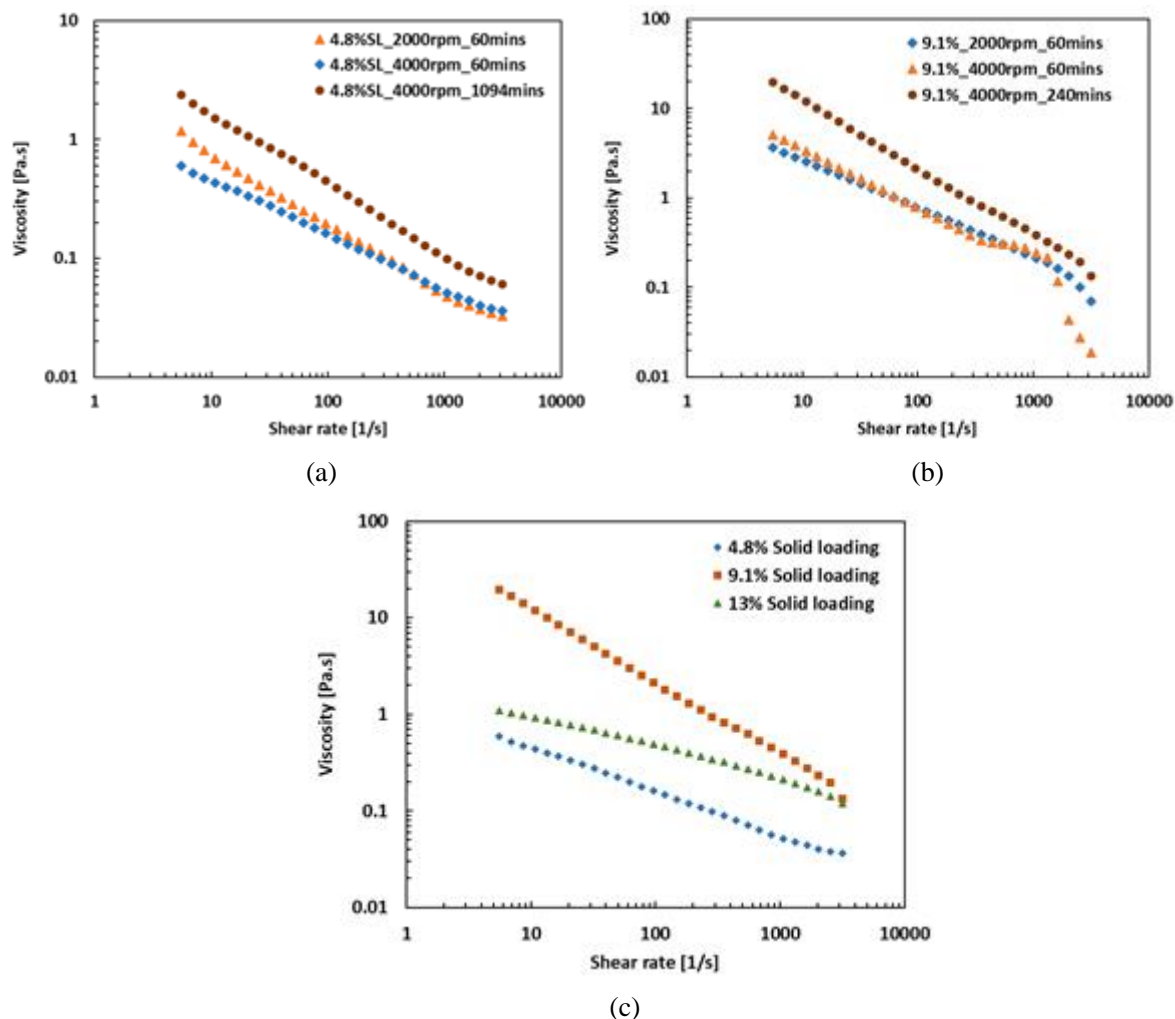


Figure 41. Shear thinning behavior of slurries for (a) 4.8% solids loading, (b) 9.1% solids loading and (c) comparing the three solid loadings. Source: ORNL



A Hegman gauge was used to analyze agglomerates in the slurry. Agglomerate size decreased with increase in solid loading, which is also an interesting phenomenon, as shown in Figure 42.

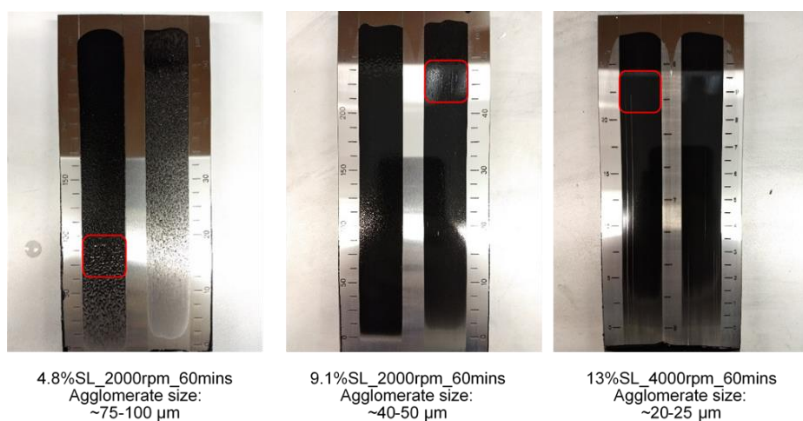


Figure 42. Agglomerate size analysis by Hegman gauge. Source: ORNL

Coatings on the GDL were applied using conditions as shown along with the results in Table XIV.

**Table XIV. Results of Slurry Coatings with a Doctor Blade on the GDL**

Solid Loading (%)	Mixing Speed (rpm)	Mixing Time (mins)	Doctor Blade Height (mm)	Results Observed	Coating Images
4.8	6000	240	0.254	It was impossible to coat the slurry because of the inhomogeneity.	
9.1	2000	60	0.254	A good coating was observed with this doctor blade height (image on the left) but after drying cracks were observed due to greater coating thickness (image on the right).	
9.1	2000	60	0.127	A good coating was observed with this doctor blade height and even after drying the coating was acceptable (image on the left was before drying and image on the right was after drying for 1 hour).	
9.1	2000	60	0.051	Coating was not uniform with this doctor blade height (image on the left was before drying, and image on the right was after drying for 1 hour)	

A minimum 0.127 doctor blade height was required for optimal coating quality based on formulations attempted. From this preliminary analysis, a slurry with 4.8% solid loading did not exhibit good physical and rheological properties, and higher solid loadings in the range of (9.1% to 13%) were further optimized for a slot die coating process.



Optimization for coating uniformity and viscoelasticity using ink formulations of 9.9%, 11.1% and 13% solid loading were carried out at a mixing speed 4000 rpm and a mixing time 60 mins. A similar phenomenon was observed as previously described. An increase in solid loadings resulted in a decrease in viscosity of the slurry as seen in Figure 43. It is hypothesized that an increase in solid loading also increases 1-propanol, which leads to better dispersion and a reduction in viscosity. Agglomerate size for all three inks were characterized with a Hegman gauge and was found to be between 3  $\mu\text{m}$  to 15  $\mu\text{m}$ .

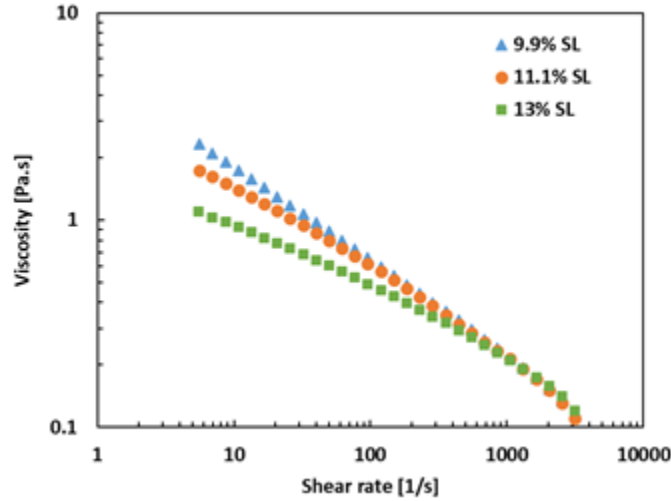


Figure 43. Shear thinning behavior of inks with varying solid loading. Source: ORNL

Rheological results were analyzed for understanding the effect of solid loadings on storage and loss modulus. As shown in Figure 44 (a), the storage modulus ( $G'$ ) was less than loss modulus ( $G''$ ) in inks with solid loadings 11.1% and 13%. The case of  $\tan \delta = 1$  means  $G' = G''$  and is called the viscoelastic or 'gel point'. It was observed that an increase in solid loading increases  $\tan \delta$  as shown in Figure 44 (b). The case of  $\tan \delta > 1$  means the slurry is more viscous than elastic, which means deformation of the slurry with exertion of force increases with increasing solid loading. Thus, it was concluded that a slurry with a solid loading between 9.9% and 11.1% exhibited the best viscoelastic properties for slot die coating.

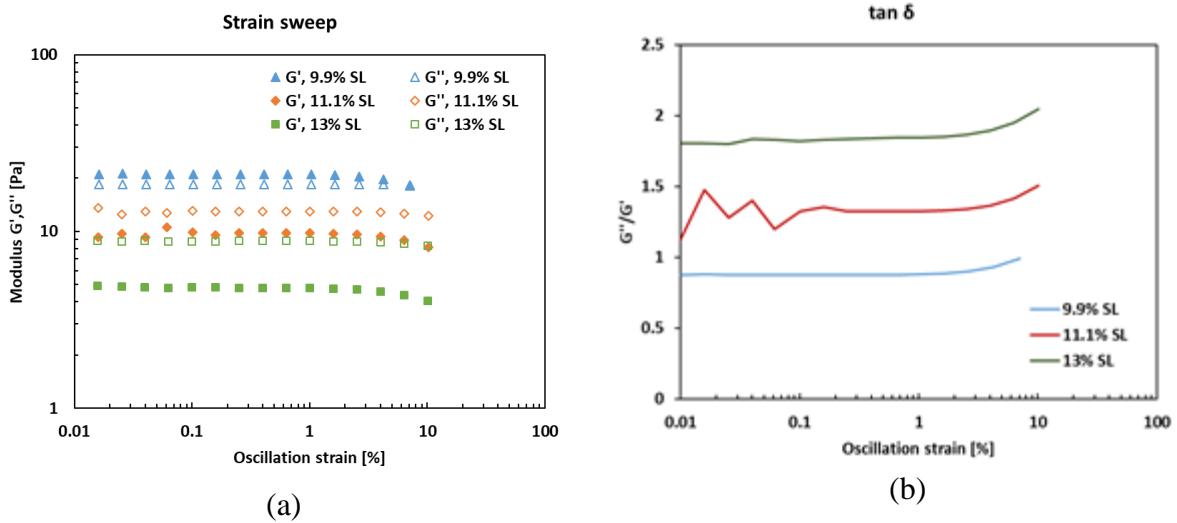


Figure 44. Effect of ink composition on (a) storage and loss modulus and (b)  $\tan \delta$  as a function of solid loadings. Source: ORNL

Coatings on the GDL with a doctor blade were carried out with 11.1% solid loading ink. Coated GDLs were dried in the tape caster for one hour. A dry thickness of 8-10  $\mu\text{m}$  was achieved with a 25  $\mu\text{m}$  doctor blade height. Figure 45 provides images of the ink coatings for various doctor blade heights.

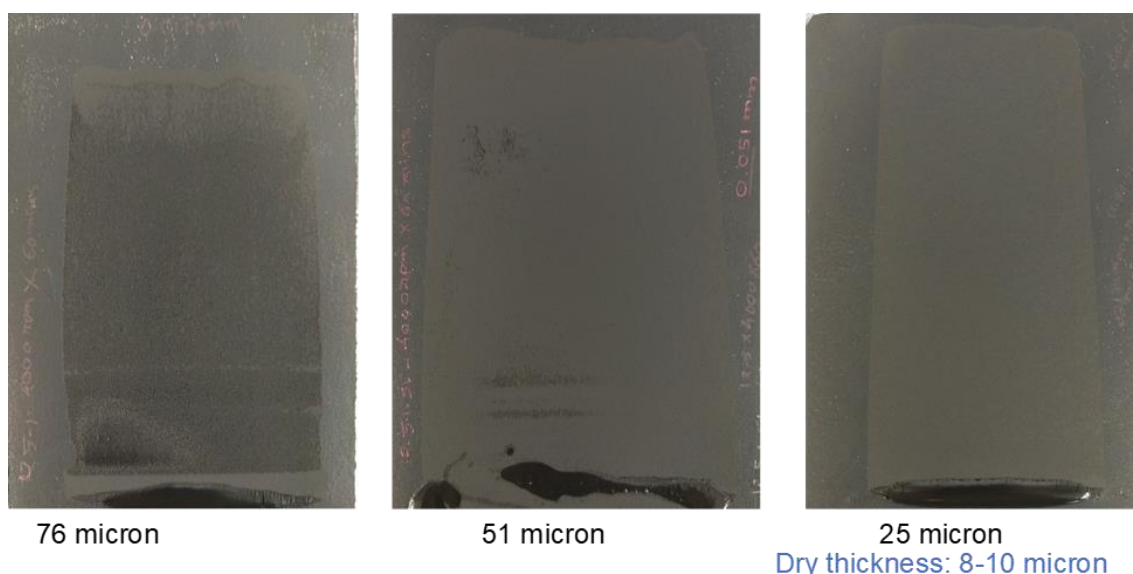


Figure 45. Ink coatings on GDL at various doctor blade heights. Source: ORNL

### Effect of solvent on Ink properties

It is hypothesized that an increase in solid loading decreases viscosity of the slurry because it also increases solvent percentage when Nafion D2020 was used. To prove this hypothesis, slurries with different solid loadings of CB and Nafion and constant solvent content were mixed at 4000 rpm for 60 mins as shown in Table XV and analyzed for the effect on viscosity.

**Table XV. Compositions of Ink Formulations Investigated for Effect on Viscosity**

Component	Weight (g) for 9.9% Solid Loading	Weight (g) for 11.1% Solid Loading	Weight (g) for 13% Solid Loading
Carbon Black	3.99	4.48	5.28
Nafion	3.59	4.04	4.75
Water	57.96	57.22	55.98
1-Propanol	10.93	10.94	10.94

An increase in solid loading at constant alcohol content resulted in increase in agglomerate size as measured using a Hegman gauge as shown in Figure 46. Agglomerates ranged from 1  $\mu\text{m}$  to 5  $\mu\text{m}$  as the solids loading increased from 9.9% to 13%.

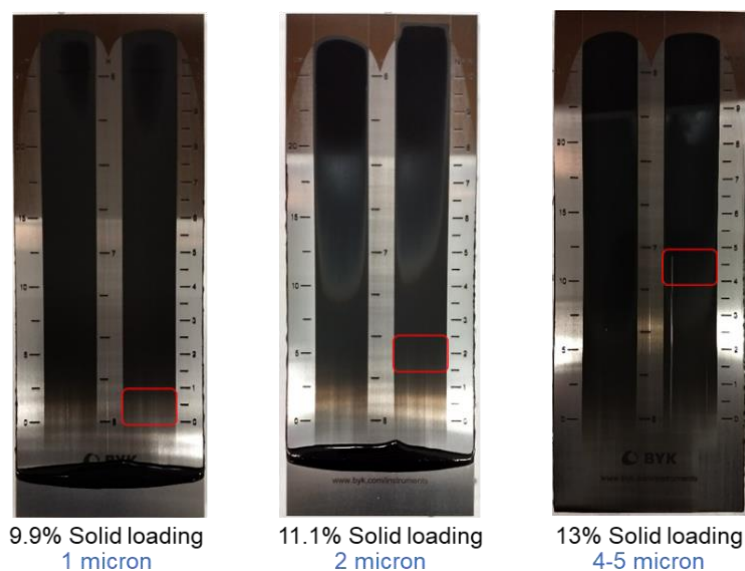


Figure 46. Agglomerate size analysis using a Hegman gauge for constant solvent and different solids loading. Source: ORNL

An increase in viscosity with increase in solid loadings with constant 1-propanol was also observed (Figure 47 (a)), which proved the hypothesis that increasing solids loading yields a better dispersion and decreasing viscosity as shown in Figure 47 (b).

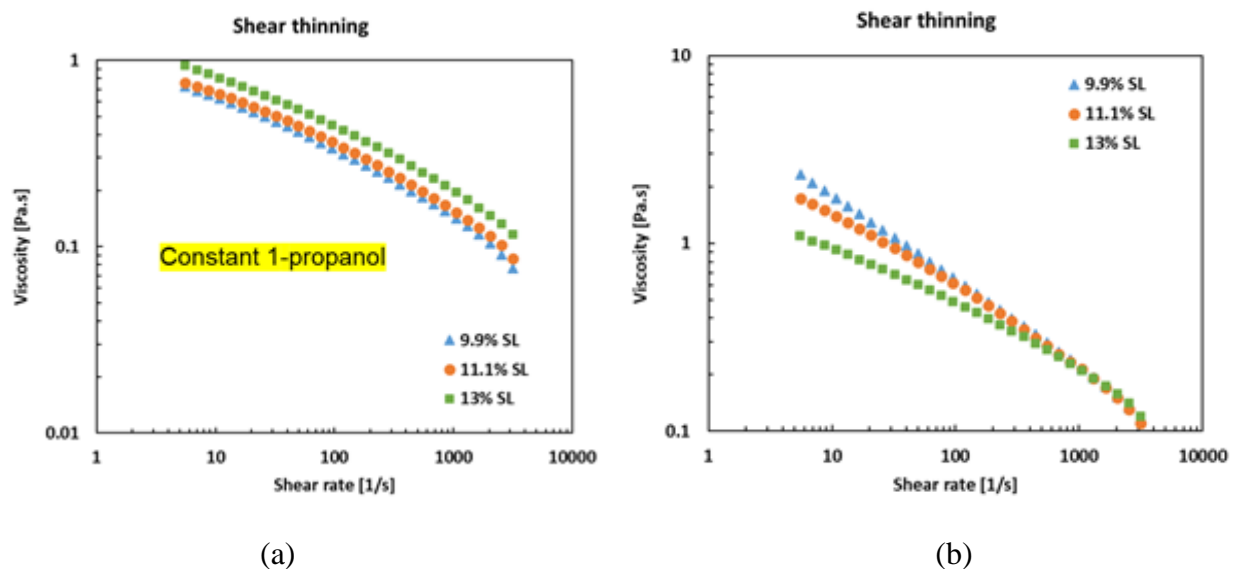


Figure 47. Effect of solvent proportion on shear thinning of inks for (a) constant 1-propanol and (b) increased solids loading. Source: ORNL

An increase in 1-propanol at constant solid loading decreases the viscoelasticity of the ink, and an increase in solid loading at constant 1-propanol increases the viscoelasticity. Data for the experiments showing the effect of solvent proportion on storage modulus ( $G'$ ) and loss modulus ( $G''$ ) of inks without and with constant 1-propanol is presented in Figure 48 (a) and (b) respectively.

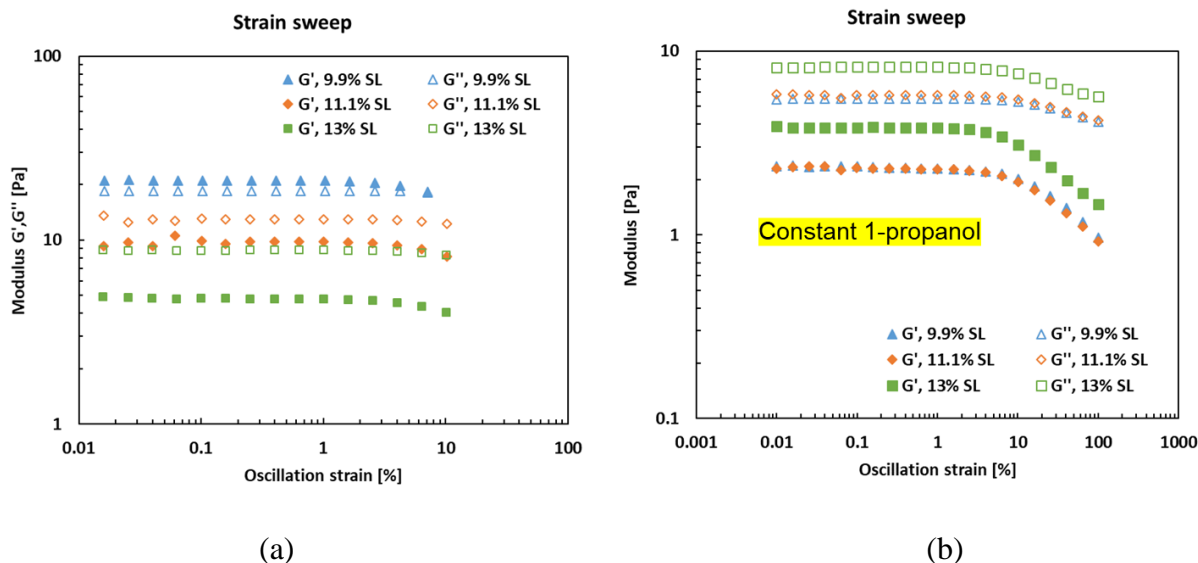


Figure 48. Effect of solvent proportion on storage and loss modulus of inks (a) without and (b) with constant 1-propanol.

Source: ORNL

## Modeling, Simulation and Data Mining

### Lawrence Berkeley National Laboratory

The objectives for the LBNL modeling, simulation and data mining studies were as follows:

- Develop a physics-based model established on principles of colloidal science for battery electrode processing. A better understanding of the electrode fabrication processes from a standpoint of colloid science can shed light into the physics of battery electrode processing, which includes complex phenomena such as interactions between organic and inorganic material, rheology of slurry, drying, and evaporation of solvents. These interactions and processes affect crucial properties of the slurry, which in turn affect the properties of the electrode such as electrochemical reactivity and mechanical strength.
- Develop the theory of synthesis using data mining and deep learning approaches. Predicting the conditions under which a specific compound and crystal structure form is an unsolved and fundamental problem in materials synthesis, and one which, if understood and harnessed, could enable the rational design of synthesis pathways of novel battery materials. To address this problem, we proposed two subsequent steps. First, using text mining and natural language processing to create a database of so-called “codified recipes” of synthesis, extracted from research papers for hundreds of thousands of inorganic compounds. Second, using machine learning in combination with first-principles thermochemical data, data mine the database and suggest synthesis routes for novel battery compounds.

### Modeling of the Slurry Rheology

The previous model that was developed to study the rheology of anode slurries with polymer binders of different molecular weights was applied to new slurry compositions. The polymer binders other than KF9300 (MW=1 million) that were used were KF 1700 (MW=0.5 million), and KF 1100 (MW=0.28 million). The viscosity of slurries of CB plus polymer binder at three different particle volume fractions, i.e., 0.9%, 1.2% and

3.2% were studied. As shown in Figure 49 (a), (b) and (c), the viscosities calculated from the model match the experimental data fairly well. In the modeling, polymer brush length ( $L$ ) and fractal dimension ( $D_f$ ) were chosen as fitting parameters.  $D_f$  is a parameter characterizing the structure of particle aggregates. The value of  $D_f$  is dependent on the competition between the reaction and diffusion rates of particles. Stronger attraction increases the particle aggregation rate and therefore, changes the aggregations from diffusion limited to reaction limited.  $D_f$  ranges from 1 to 3 for diffusion limited cluster aggregation to reaction limited cluster aggregation.  $D_f$  is related to the colloidal interactions.  $D_f$  is set equal to 2, 1.7, and 1.5 to fit KF9300, KF1700 and KF1100 respectively. The polymer lengths estimated from experimental considerations were close to the ones used for modeling.

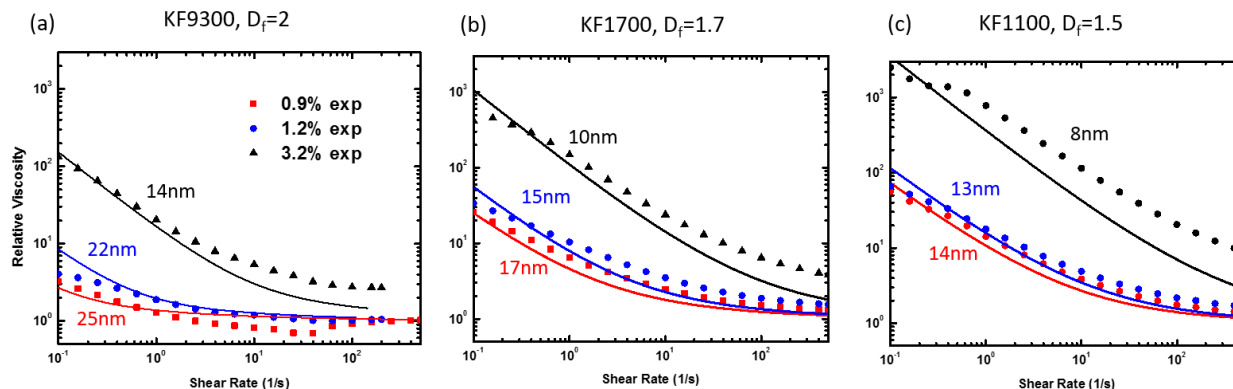


Figure 49. Experimental and modeling rheology of carbon black slurries with polymer binders of different molecular weights: (a) KF9300 (MW: 1 million), (b) KF1700 (MW: 0.5 million), and (c) KF1100 (MW: 0.28 million). Source: LBNL

For high molecular weights, the attraction is weak, and the assembly of particles is dominated by reaction. A more close-packed assembly, i.e. higher  $D_f$ , should be obtained as illustrated in Figure 50 (a). At low molecular weights, attraction is strong, and assembly is controlled by particle diffusion. Therefore, a more open assembly, i.e. lower  $D_f$ , is expected. Figure 50 (b) shows an increase in viscosity with increasing  $D_f$  for the three polymer binders studied.

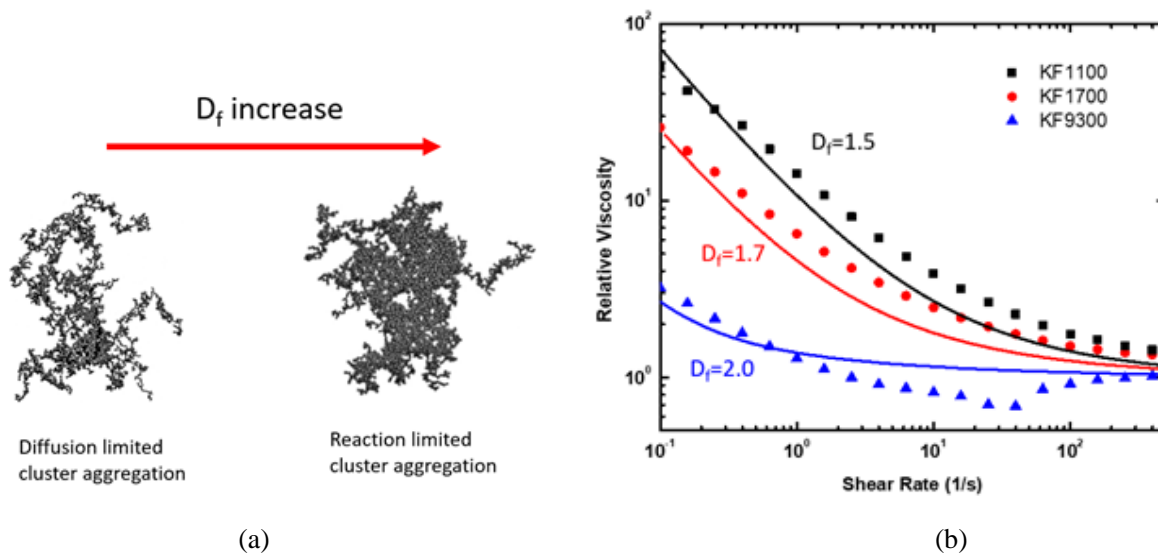


Figure 50. Proposed assembly structures for CB with polymers of different molecular weights (a) as  $D_f$  increases and (b) the relationship of increased viscosity with decreasing  $D_f$ . Source: LBNL



To support our hypothesis and get a better understanding of the effect of molecular weights on assembly, we followed our previous recipes and prepared three CB plus PVDF slurries using the three polymer binders and then studied the assembly behavior of CB's. Optical images and SEM images were taken to analyze the morphologies of the CBs. As illustrated in Figure 51, both the optical and SEM images clearly show that the assemblies of CBs become closer packed with increasing polymer binder molecular weights from KF1100 to KF9300. The assembly morphologies of CBs were very similar to what we proposed during the modeling studies. More accurate values of fractal dimensions from ImageJ were pursued. The “FracLac” plugin in software ImageJ was used to analyze the fractal dimension of the above CB slurries.

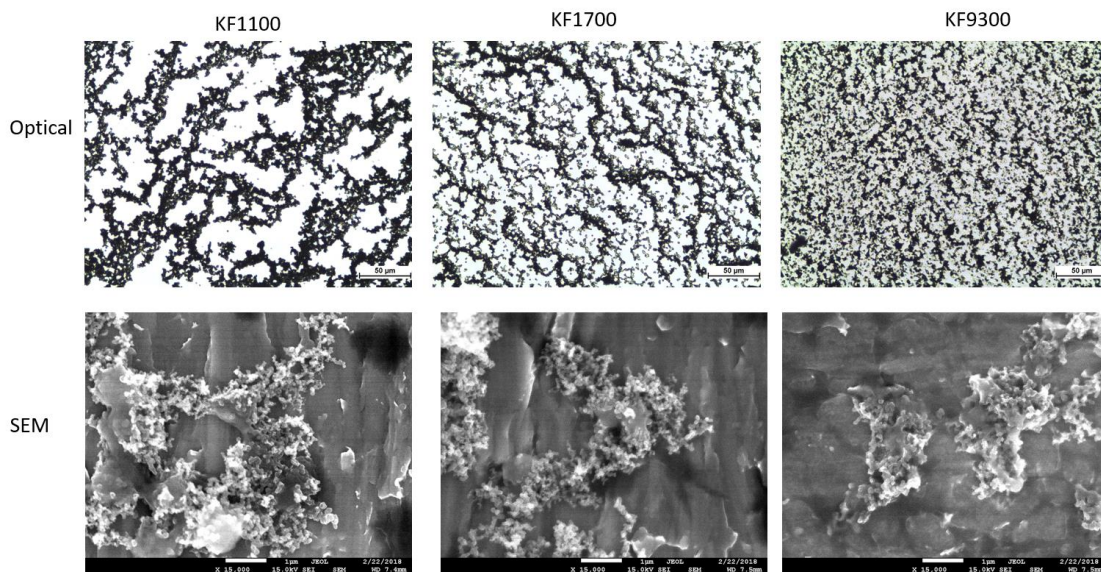


Figure 51. Optical and SEM images of dried CB particles with PVDF of three binders with different molecular weights. Source: LBNL

The whole anode slurry was modeled with micron-scale graphite active material particles in addition to the solvent, binder, and CB components used earlier. The CB slurry was used as the background medium and its viscosity as the medium viscosity. The (hydrodynamic) contribution from addition of graphite particles to slurry viscosity was calculated from the Krieger-Dougherty model. As shown in Figure 52, the modeling predicts the viscosity of the whole slurry, fairly well, with polymer binder of different molecular weights.

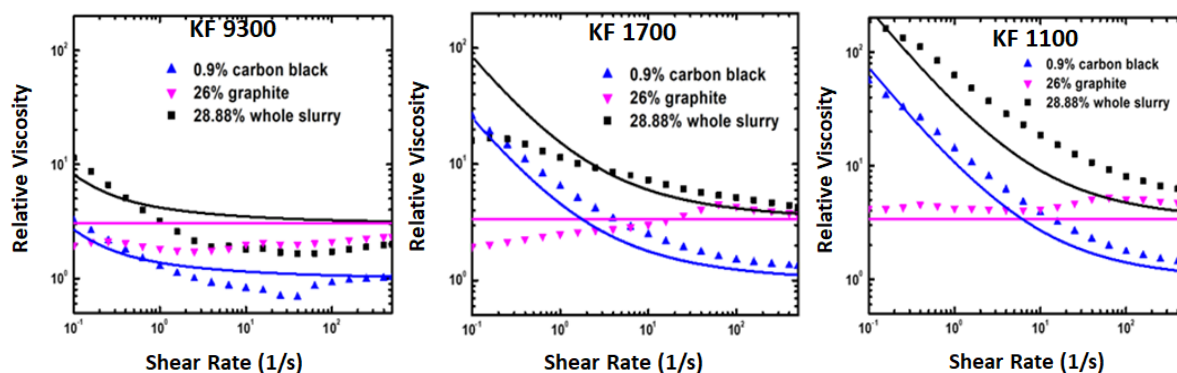


Figure 52. Modeling results of anode slurries with polymer binders of different molecular weights: (a) KF9300, (b) KF1700 and (c) KF1100. Source: LBNL

Micron-scale graphite active material particles are not expected to form network as colloidal particles, but instead are expected to be embedded in the CB network, but are primarily affected by gravity and hydrodynamics as illustrated in the diagram and SEM image of Figure 53 (a) and (b). The resulting predictions were compared with steady-state rheology data that was obtained for whole anode slurries at a range of shear rates shown in Figure 53 (a). Good agreement was obtained at high shear rates, while at low shear rates, the whole slurry values were nearly identical to the earlier slurries that did not contain graphite particles, but which possessed the same volume fractions of binder and CB.

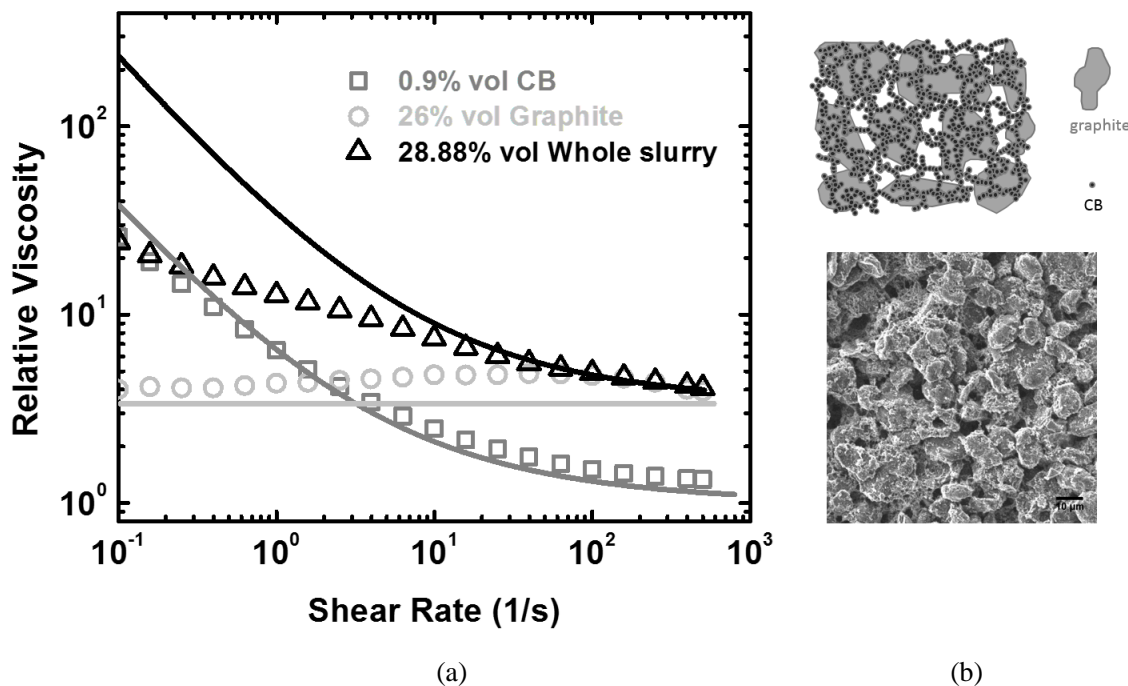


Figure 53. Material effects for (a) steady-state viscosity data and model predictions and (b) diagram of whole anode slurry organization with the SEM image of the anode material. Source: LBNL

The application of viscoelastic models on studying the rheology of CB inks for fuel cells was discussed with researchers from NREL and a plan was developed to apply the models to study the rheology of fuel cell inks. Upon consultation with project management, and our NREL teammates, LBNL efforts were redirected to focus on developing a modified slurry model that describes NREL's fuel cell inks. Since the physical phenomena governing ink behavior have not been fully determined, we decided to begin not with a set of specific sub-models describing physical phenomena, but by exploring possible mathematical model forms. By calculating optimal fits of these mathematical forms to ink viscosity data from NREL (for both high surface area (HSA) CB and a Vu brand of CB), we were able to immediately rule out forms that cannot describe the inks and find forms that might provide adequate descriptions. Of these, we selected forms that retain some mathematical similarity with our earlier battery slurry model as shown by Figure 54 (a) and (b) for different ranges of viscosity (viscosity data provided by NREL). Since the battery slurry model was built from a set of sub-models describing various physical phenomena, similar mathematical forms may indicate that the corresponding sub-models can be reused in the description of fuel cell inks.



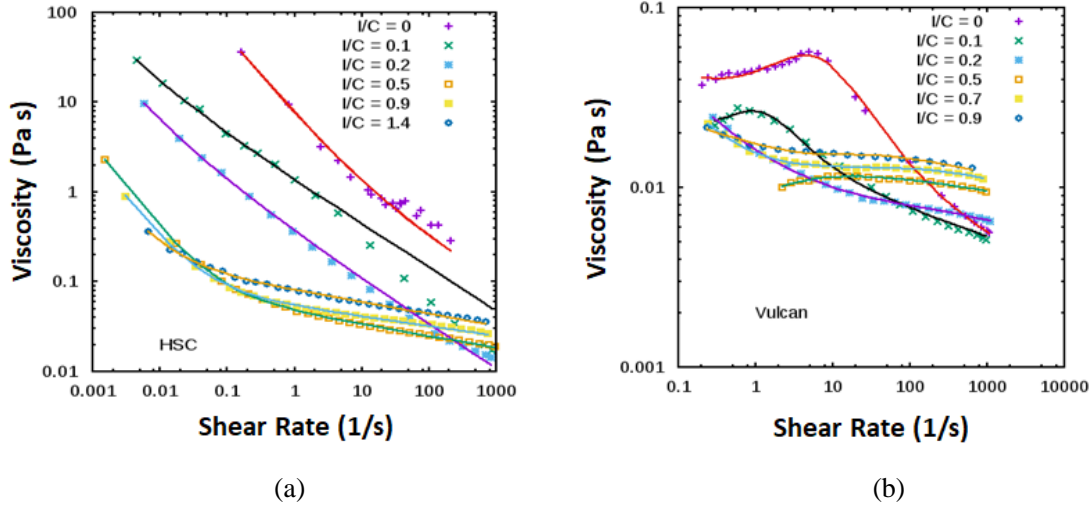


Figure 54. Fits of selected mathematical forms to fuel cell ink viscosity data for (a) high viscosity and (b) low viscosity inks. Source: NREL

Having determined candidate mathematical model forms, we began to explore ways in which they could arise from a physical model. We first considered modifying the battery slurry model in the simpler case of inks based on the Vu-brand CB, which show monotonic viscosity dependence on shear rate. The mathematical form fits suggest that this behavior might be understood in terms of a low shear-rate regime that corresponds to particle-particle interactions, and a high shear-rate regime that corresponds to hydrodynamic interactions. The battery model developed earlier made the same distinctions, and the mathematical fitting form was designed to have the same low shear-rate regime shear-rate dependence as in the battery model; the good fits obtained with this form suggest that it might be appropriate to reuse the particle-particle interaction sub-model used in the earlier battery model. In the high shear-rate regime, variation of the effective aggregate volume fraction in the battery model is the only possible explanation for the shear-rate dependence suggested by the fitting form. The microrheological model used as a basis for the battery model proposes a relationship (which must be solved numerically) to calculate this volume fraction. However, by nesting a numerical solver within an iterative nonlinear least squares fitting procedure, it was determined that this form cannot produce the observed viscosity behavior shown in Figure 55. This suggests that the hydrodynamic sub-model used in the battery model must be revised in order to describe the fuel cell inks.

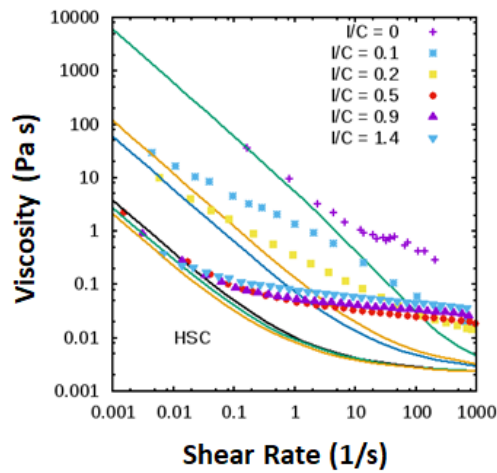


Figure 55. Least-squares fits of battery model form to fuel cell ink data (provided by NREL), showing poor agreement at higher shear rates and suggesting that hydrodynamic sub-model should be revised. Source: LBNL

## Data Mining of Materials Synthesis “Recipes”

A machine learning algorithm was implemented to identify potential targets and precursors of a synthesis route. The algorithm employs bi-directional recurrent neural network architecture with long short-term memory (LSTM) units as diagrammed in Figure 56. First, a synthesis paragraph is split into sentences and each sentence is also divided into tokens. The algorithm takes as input a sequence of tokens creating a feature vector for each of them (blue circles). Next, the algorithm processes each sentence token by token and then it feeds the token to neural net in forward (green rhombs with  $l_i$  marks) and reverse (green rhombs with  $r_i$  marks) directions. Then it combines information (green rhombs with  $c_i$  marks) and generates output (yellow circles). It then decides on each token whether it represents target material, precursors compounds, any other material mention or none of them. The bi-directional screening of sentence allows for taking in to account situations when the defining word precedes or follows the materials object mention. For example: “The Material was synthesized <...>” vs. “To synthesis the Material <...>”. In both situations “synthesize” is a meaning-defining word which provides information that the Material is target of the synthesis route.

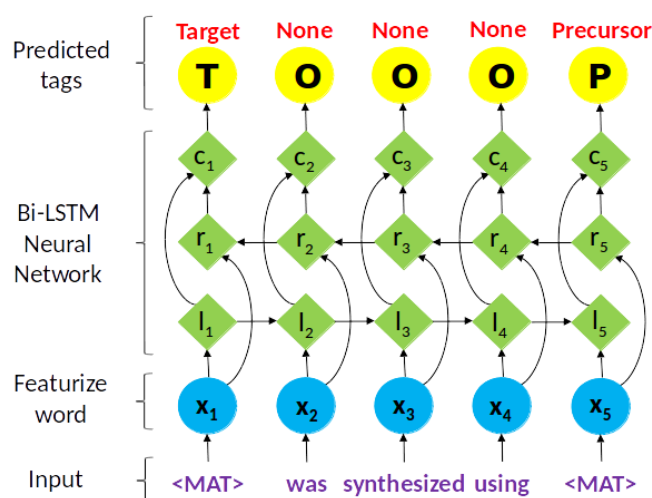


Figure 56. Schematic representation of the algorithm based on bi-directional recurrent neural network with LSTM units to classify materials entries in synthesis paragraphs. Source: LBNL

As a word feature's vector, we used Word2Vec representation (<https://code.google.com/archive/p/word2vec/>) trained on ~2,000 synthesis recipes paragraphs, and its grammatical features such as part-of-speech and action verb. The algorithm was trained on ~700 sentences. The current accuracy estimated by calculation F1 score is: for materials F1 = 84%, for targets F1 = 83%, for precursors F1 = 84%.

A Materials Entity Recognition algorithm was developed and implemented to identify materials mentions in synthesis paragraphs and classify which materials are mentioned in context of starting compounds (precursors) and final products (targets) of the synthesis. The algorithm uses a recurrent neural network model with LSTM units to scan tokens in synthesis paragraph sentences and identify tokens which represent materials entities. The accuracy of the algorithm is ~90%. In significant number of paragraphs, target names are given in the form of an abbreviation, yet other significant fraction of target names contain off-stoichiometric variables. For example, “The conventional solid state reaction method was employed to prepare the ceramics with formula  $(1-x)\text{Pb}(\text{Zr}_{0.52}\text{Ti}_{0.48})\text{O}_3-x\text{SrBi}_2\text{Nb}_2\text{O}_9$  or  $(1-x)\text{PZT}-x\text{SBN}$  where  $x = 0, 0.1, 0.3, 0.5, 0.7, 0.9$  and  $1.0$  weight fraction” or “ $\text{Ba}[(\text{Ni}_{0.6-x}/2\text{Zn}_{0.4-x}/2\text{Mgx})1/3\text{Nb}_{2/3}]\text{O}_3$  ( $x = 0, 0.1, 0.2, 0.3$ ) powders were synthesized by a solid-state reaction method”. This issue significantly complicates search of the materials properties in Materials Project database, which are important for building chemical reactions. To deal with these and similar cases, a Materials Parser utility was developed, which is able to: a) search the text for abbreviations and make corresponding substitution of chemical name, b) correctly split chemical formula into elements and

corresponding stoichiometries, c) look for chemical names in PubChem (<https://pubchem.ncbi.nlm.nih.gov/>) database and assign corresponding chemical formulas.

In a significant amount of synthesis paragraphs (~70%), materials names are given by chemical formulas with variables either as elements or in stoichiometry, or both. For example, “Ba[(Ni<sub>0.6-x</sub>/2Zn<sub>0.4-x</sub>/2Mgx)<sub>1/3</sub>Nb<sub>2/3</sub>]O<sub>3</sub> (x = 0, 0.1, 0.2, 0.3) powders were synthesized by a solid-state reaction method”. This issue significantly complicates search of the materials in Materials Project database and constructing chemical reactions. We have extended our Material Parser to be able to correctly resolve corresponding values of variables from a given sentence. The parser uses various heuristic approaches based on “regular expression” Python package. For the example given earlier, the parser finds values of x = 0, 0.1, 0.2, 0.3, substitutes them into chemical formula and generated corresponding list of correct formulas: Ba[(Ni<sub>0.6</sub>Zn<sub>0.4</sub>)<sub>1/3</sub>Nb<sub>2/3</sub>]O<sub>3</sub> for x = 0, Ba[(Ni<sub>0.55</sub>Zn<sub>0.35</sub>Mg<sub>0.1</sub>)<sub>1/3</sub>Nb<sub>2/3</sub>]O<sub>3</sub> for x = 0.1, etc.

To address some issues due to wrong sentence tokenization, an additional method was implemented in Material Parser which corrects the incorrectly tokenized chemical names. The currently used Chem-Data-Extractor packaged for sentences processing fails to separate properly chemical formulas and chemical names or other terms, for example: “titanium oxide TiO<sub>2</sub>”, “LiFePO<sub>4</sub> compound”, etc. The updated version of Material Parser performs a “clean-up” of these or similar tokens using heuristic rules and “regular expression” package. This improved extraction of materials formulas by ~15%.

An algorithm was implemented which obtains sequence of synthesis step from the synthesis paragraphs. The algorithm utilizes feedforward neural network combined together with Word2Vec model (Genism package) and grammatical parser (SpaCy package). It traverses each sentence in the paragraph word by word and classifies them according to the following categories: not operation, start of synthesis, heating operation, mixing operation, drying operation, shaping operation and quenching operation. These classes represent the most important steps of ceramics synthesis process. The accuracy of the algorithm in terms of F1 score, precision and recall for each class is given in Table XVI.

**Table XVI. Steps in Synthesis Process and Accuracy of Data Mined**

Operations Class	F1	Precision	Recall
Not Operation	0.939	0.937	0.94
Drying Operation	0.947	0.9	1
Heating Operation	0.902	0.868	0.939
Mixing Operation	0.842	0.87	0.816
Quenching Operation	0.5	0.4	0.667
Shaping Operation	0.867	0.929	0.812
Starting Synthesis	0.954	1	0.912

The operations classifier was used to assign to extracted reactions with corresponding synthesis steps and to obtain synthesis conditions on each step.

## R2R Functional Materials

### Argonne National Laboratory

While manufacturing cathode sheets using R2R techniques, cathode particles in the form of slurries are cast on top of the current collectors. Performance and lifetime of LIBs depend strongly on the morphology of these

cathode active particles. All the morphological features (size, shape, size distribution, internal porosity, etc.) of cathode particles are determined during the synthesis processes. Scalable cathode particle synthesis techniques, usually adopted in the industries, involves two different steps: a) Coprecipitation, where the hydroxide precursors are formed from the metal salts through reactions inside chemical reactors, and b) Calcination, where the hydroxide precursors are oxidized, lithiated and sintered through a high temperature heat-treatment process. A computational methodology was developed to elucidate the mechanism behind the formation of primary and secondary active particles during the coprecipitation process. Mass balance relations for the reactants were coupled with the mechanisms of nucleation, growth and aggregation of the primary particles to successfully capture the formation of secondary active particles. The developed computational methodology was extended to analyze the impact of solution pH and ammonia content on the size and size distribution of the secondary particles. The major outcomes are discussed in the following sections.

### Impact of Ammonia Content

Increasing ammonia content helps to increase the amount of metal ammonia complex within the solution. Larger amounts of metal ammonia complex lead to higher nucleation density, as well as faster growth of the primary particles. The diffusion coefficient of primary particles has been hypothesized to be directly proportional to the bulk ammonia concentration. Results from the present simulation have been depicted in Figure 57 (a), which indicate that increasing ammonia content leads to larger size of the secondary particles. The secondary particle size distribution is also higher for larger concentrations of ammonia within the reacting solution. Comparison with experimental results demonstrates good correlation. As the particle size gets smaller, the size distribution also reduces monotonically as shown in Figure 57 (b).

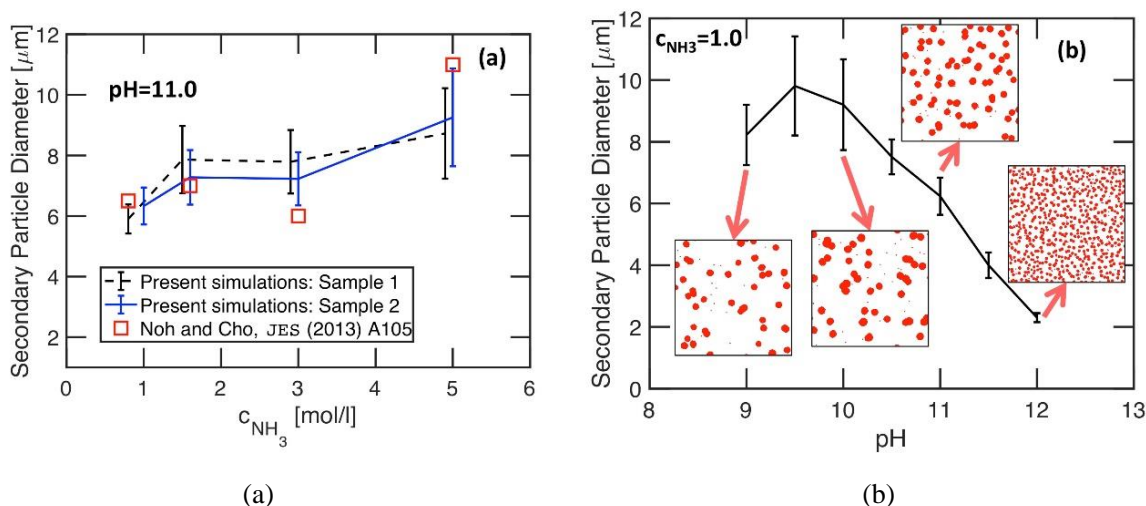


Figure 57. (a) Variation in secondary particle diameter with ammonia content within the reacting solution and (b) decrease in secondary particle size with increasing solution pH. Source: ANL

### Impact of Solution pH

By solving mass balance equations, it has been observed that with increasing solution pH, the amount of metal ammonia complex decreases. Hence, the growth rate of primary particles also decreases at higher pH. However, the nucleation density tends to increase significantly due to the orders of magnitude increase in the concentration of hydroxyl anions. As demonstrated in Figure 57 (b) above, with increasing solution pH, the average size of secondary particles decreases gradually. This can be attributed to the proton abstraction reaction that may occur at the particle surface at high values of pH, and the subsequent repulsion experienced by the primary particles.

## Phase Map Between Solution pH and Ammonia Content

A phase map was developed and is shown in Figure 58, which clearly demonstrates that smaller secondary particles should precipitate at higher pH. Increasing ammonia content not only helps to increase the secondary particle size, but also results in a larger size distribution. Two optimum regions have been specified in Figure 58 (by red circles), where secondary particles of certain size are supposed to precipitate with minimum particle size distribution. Optimum operating conditions, in terms of pH and ammonia content, for precipitating relatively larger and smaller-sized secondary active particles have also been highlighted within the figure.

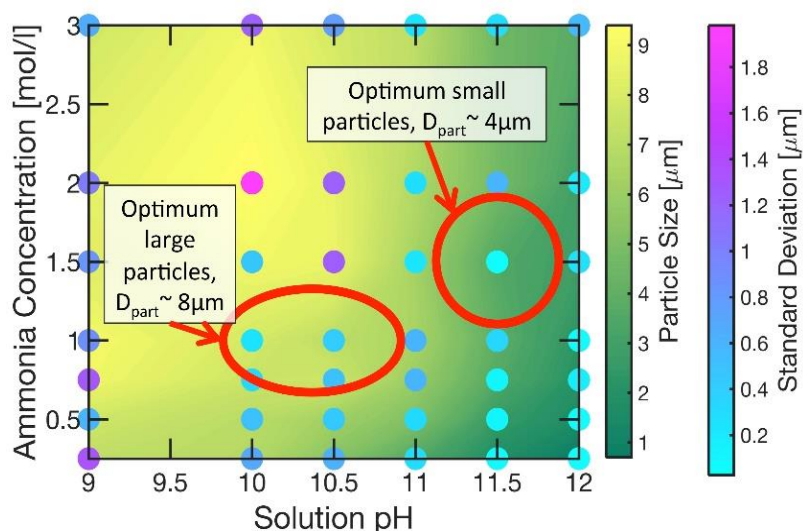


Figure 58. Phase map between solution pH and ammonia content showing the average particle sizes and their first standard deviation under the assumption of Gaussian particle size distributions. Source: LBNL

Based on SEM images of several transition metal hydroxide precursors and lithiated metal oxides, it is evident that the primary particles are never spherical in shape. The present model approximates the primary particles as spheres. Relaxation of this assumption and developing the capability to simulate non-spherical elongated primary particles is a necessity for obtaining more accurate estimations of the secondary particle size and its internal porosity.

Detailed experiments were conducted to understand the growth of primary and secondary particles observed within the nickel manganese cobalt hydroxide precursors. The coprecipitation experiment was carried out in a chemical reactor maintained at 60°C. The reaction proceeds with the addition of aqueous ammonia and transition metal sulfate solution (prepared by mixing nickel, cobalt and manganese in desired amount) into the reactor. A pH-meter is used to monitor the pH value. Sodium hydroxide is automatically added to the reacting solution to maintain the desired pH. Samples have been prepared under two pH levels, namely, 10.6 and 11.4. An overhead rotor is used to stir the solution at a constant speed. Nitrogen gas flow is maintained through the reacting solution to get rid of oxygen. The total experiment has been conducted for three hours. In situ WAXS, SAXS and USAXS experiments were conducted at ANL's APS. A Cilas particle size analyzer has been used to measure the evolution of secondary particle size within the reactor.

## Crystallographic Structure of the Hydroxide Precursor

WAXS data has been used to analyze the crystallographic structure of the samples. The area of the (101), (102), and (100) peaks of the two samples (pH 10.6 and 11.4) have been plotted in Figure 59. The olive line stands for the computationally predicted amount of  $\text{Ni}_{1/3}\text{Mn}_{1/3}\text{Co}_{1/3}(\text{OH})_2$  obtained by solving global mass



balance relations. The computational model is able to successfully predict the larger precipitation of hydroxide precursors at higher magnitudes of pH. Maximum amount of deposition and growth was observed along the (101) direction, which increases almost linearly with time. A computational model was developed to estimate the amount of hydroxide precipitate by solving global mass balance and chemical equilibrium equations. The developed model successfully captured larger precipitation at higher pH.

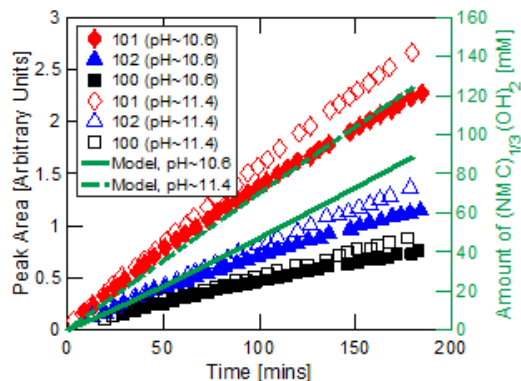


Figure 59. Area of the diffraction peaks obtained by analyzing the WAXS data during operation at pH 10.6 (solid symbols) and 11.4 (open symbols). Source: ANL

### Growth of Primary and Secondary Particles

USAXS data collected from the APS have been used to determine the size evolution of primary particles. Faster growth is observed initially, which slows down as the coprecipitation continues. According to the growth pattern demonstrated in Figure 60 (a), primary particles initially grow at very high rates of 1 nm/s and 0.22 nm/s during operations at pH 10.6 and 11.4, respectively. Later, the growth rate slows down to 0.02 nm/s and 0.03 nm/s for pH 10.6 and 11.4, respectively. SEM images of the particles obtained at different pH levels have been included as inset in Figure 60 (a). Presence of porous structure has been attributed as the major reason behind faster growth of primary particles observed after long-term operation at higher pH.

Secondary particle size evolution was measured using the Cilas particle size analyzer. As demonstrated in Figure 60 (b), the average secondary particle size is significantly larger at lower pH. Size of secondary particles ( $D$ ) correlate with time ( $t$ ) through power law relations ( $D \sim t^n$ ). Growth of secondary particles can be divided into two distinct domains, where power law relations exist between particle size and time, but with different exponents. Two distinct regimes were identified, corresponding to faster growth of secondary particles at smaller time, and relatively slower growth during long time operation. The faster growth regime with an exponent of  $n \approx 0.7$  can be attributed to a combination of rate limited and diffusion-limited growth. At longer times, smaller exponent of  $n \approx 0.25$  indicates a combination of diffusion limitation and shortage of available reactants.

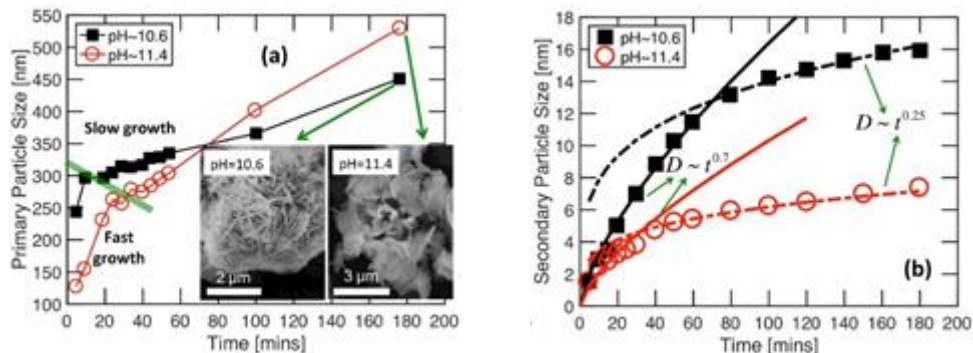


Figure 60. (a) Growth of primary particles with time and SEM image of the coprecipitated particles are shown as inset. (b) Evolution of secondary particles with time. Source: ANL

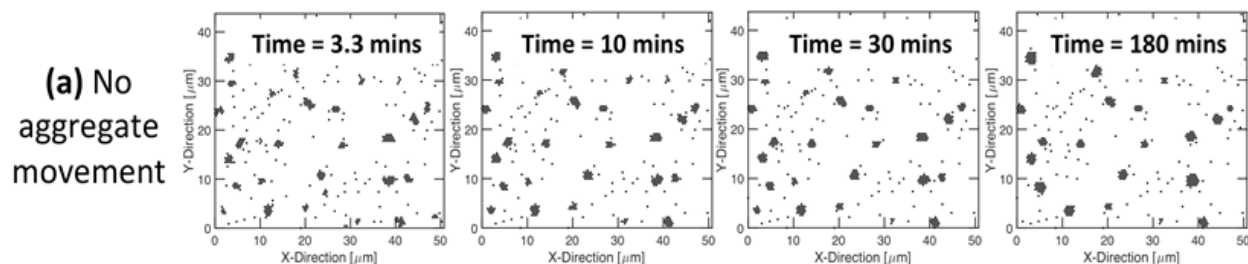
Based on the SEM images of the co-precipitated transition metal hydroxide precursors, it is evident that the primary particles are never spherical in shape, and usually forms a disk like structure. Tap density of the sample co-precipitated at pH 10.6 is much higher than that obtained at pH 11.4. This indicates presence of higher internal porosity within the precursors precipitated under high pH. Further electrochemical characterization of the samples, conducted by our collaborators, revealed that the cathode active materials generated from porous precursors demonstrate improved rate performance. Whereas, better capacity retention was observed for the samples with higher tap density. Hence, for improved rate performance, it is beneficial to conduct co-precipitation at higher pH, whereas, for enhanced capacity retention, co-precipitation should be conducted at lower magnitudes of pH.

Two different manuscripts were prepared for publication in peer-reviewed journals. The first manuscript covered detailed *in situ* and *ex situ* experiments conducted to analyze the growth dynamics of primary and secondary particles, respectively. Tap density measurement and SEM images taken to characterize these primary and secondary particles, were also discussed in the first manuscript. Detailed computational procedures developed to capture the nucleation, growth and aggregation of primary particles were discussed in the second manuscript. Comparison between computational predictions and experimental observations was also covered in this particular article.

Research in the first one and a half years captured the particle growth mechanism usually observed in batch reactors. The majority of the coprecipitation reactions are usually conducted in continuous stirred tank reactors (CSTR). Hence, some effort was devoted to developing computational models that can capture the primary particle aggregation process observed there. Unlike batch reactors, usually a steady state condition exists within CSTRs. Lifetime of a particle within a CSTR is characterized by its residence time. Within this time period, primary particles nucleate then grow and aggregate with each other or with existing secondary particles. Several physico-chemical aspects, such as, movement of the secondary particles, repulsion among the primary particles, and fluid shear induced breakage of the secondary particles, which were missing in the earlier version of the computation model, have been incorporated within the modified version, and are described below.

### Movement of Secondary Particles

Due to rigorous stirring, both primary and secondary particles within the reactor keep moving around. In the earlier version of the computational model, movement of secondary particles was not captured. The particle aggregation process has been modified to incorporate the movement of secondary particles, which aids in further agglomeration of the secondary particles. Figure 61 demonstrates the growth of secondary particles comparing between the cases of “no secondary particle movement” (see Figure 61 (a)) and “with secondary particle movement” (see Figure 61 (b)). Movement and aggregation of the secondary particles can be clearly observed in Figure 61 (b).





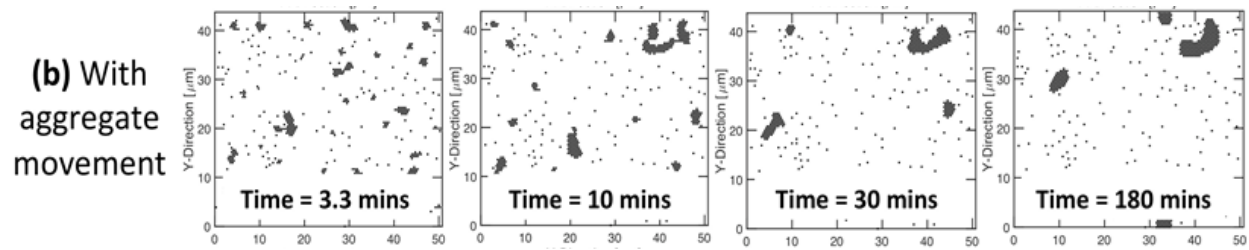


Figure 61. Evolution of secondary particle morphology with time (a) without the movement of secondary particle aggregates and (b) incorporating the movement of secondary particle. Source: ANL

### Repulsion Among Primary Particles Due to Surface Charge

Since coprecipitation reaction is always conducted at relatively high pH, there remain excess hydroxyl anions ( $OH^-$ ) within the solution. These anions can participate in proton abstraction reaction with the surface of the primary hydroxide particles, and effectively form negative charge at the particle surface. Strength of this surface charge increases with increasing solution pH. This surface charge tends to repel the primary particles, and eventually leads to flocculated structure or relatively smaller size of the secondary particles. Figure 62 demonstrates the impact of charge strength on the secondary particle size and morphology. Two distinct regions were observed. In the first phase (also characterized as Regime I), increasing charge strength demonstrates minor impact on the particle size. Average sizes of the particles are also relatively large in Regime I. Decrease in sphericity of the particles, with increasing surface charge strength, may be observed in this domain due to internal repulsion. Overall, low strength of the surface charge is observed at low pH. In the second phase (characterized as Regime II), excessive surface charge strength prevents the primary particles from aggregating. Hence, the secondary particle size decreases dramatically with increasing surface charge strength, and the sphericity becomes extremely poor. This type of aggregation is usually observed at very high pH conditions, where coprecipitation is not advisable.

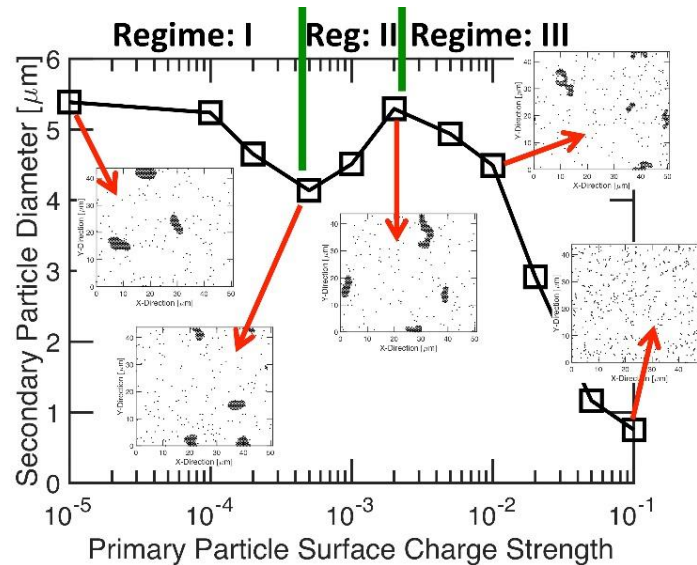


Figure 62. Variation in secondary particle diameter with increasing surface charge strength of the primary particles. Source: ANL

The coprecipitation of hydroxide precursors can be modeled as the following three steps: 1) nucleation, 2) growth, and 3) aggregation. The aggregation step is considered to be a complicated one, which involves not only aggregation of particles, but also rupture of the aggregates under extreme conditions. Breakage of secondary particles due to fluid shear induced force were also incorporated to extend the capabilities of the aggregation model. Due to the stirring mechanism within the reactor, lots of large and small eddies generate

(see Figure 63 (a)). Size and velocity of these eddies can be estimated using the Kolmogorov theory. Due to the shear force exerted by these eddies, aggregates larger than the smallest eddy length-scale, tends to rupture. Figure 63 (b) demonstrates a representative particle used for analyzing their stability under fluid shear induced forces. The phase map between particle length and aspect ratio, shown in Figure 63 (c), demonstrates that larger particles tend to be more spherical in shape. However, there also exist a maximum particle size beyond which nothing is stable, and this maximum size depends on the stirring speed. Comparison between the evolutions of size of the secondary particles without and with fracture is demonstrated in Figure 63 (d) by the red and black lines, respectively. Significant decrease in secondary particle size due to breakage of aggregates was successfully captured. Nucleation and growth mechanisms need to be incorporated with this generalized aggregation model for making better prediction of secondary particle size.

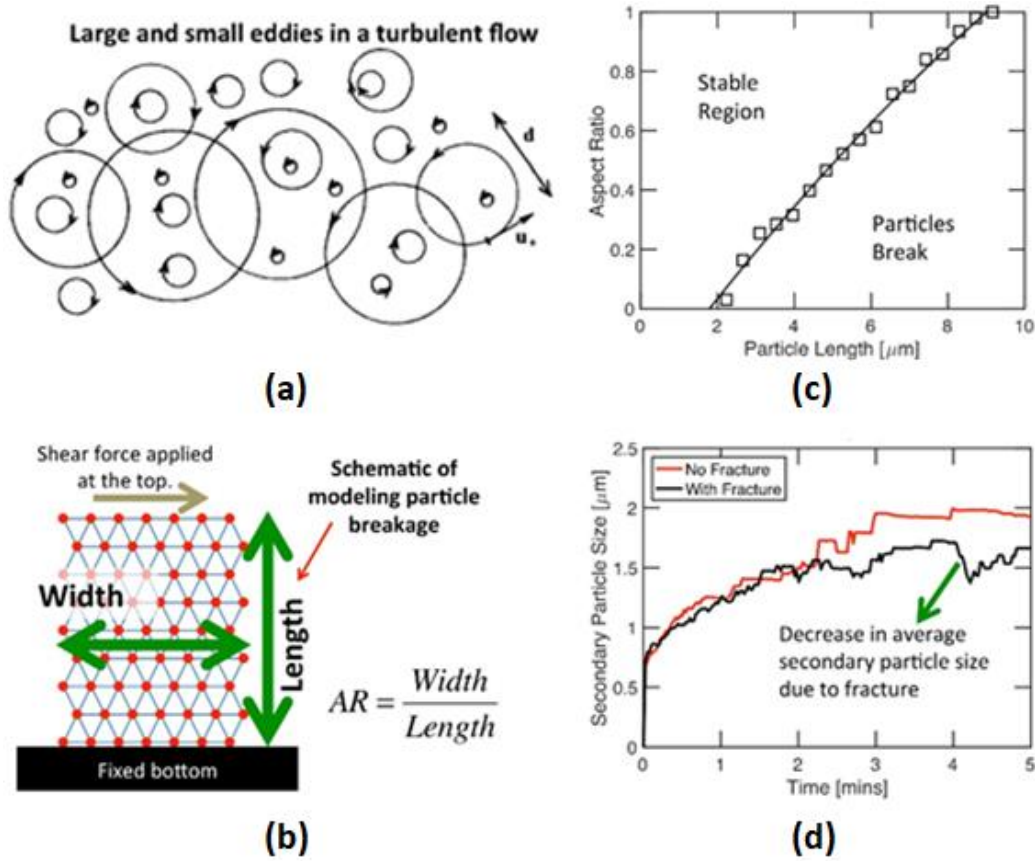


Figure 63. Breakage of secondary particles within the aggregation model. (a) Presence of large and small eddies in a turbulent flow. (b) Modeling particle rupture under the influence of fluid shear induced force. (c) Phase map between particle length and aspect ratio demonstrating the stability limit beyond which the breakage of secondary particles should occur under a stirring speed of 1000rpm. (d) Comparison between the particle size with and without rupture. Source: ANL

The next step in NMC cathode synthesis is the calcination process, where the hydroxide precursors are mixed with the source of Li and heated in an oven at 850°C – 900°C for several hours under an oxygen atmosphere. During this step, the transition metals oxidize, and Li insertion happens within the crystal structure. Also, sintering of the primary particles occur during this high temperature calcination process. A phase field based model was developed to capture the sintering of primary particles that occur during the calcination process. Figure 64 (a) graphically demonstrates sintering induced coalescence of two unequally sized particles. Higher magnitude of diffusivity leads to quicker migration of the grain boundary and early coalescence of the two particles. This behavior has also been captured in Figure 64 (b), where the reduction in area of the smaller particle has been plotted with respect to time (compare the red circles with black squares). Under high

diffusivity (red circles) the two particles coalesce faster than the case with lower diffusivity (black squares). The results obtained from the present calculations were qualitatively compared with that reported by Chockalingam *et al.* [4], which is demonstrated by the blue circles in Figure 64 (b). A decent correlation between the present results and that reported by other authors serves as a good verification step for the developed sintering model. The developed model is capable of predicting the densification and particle growth observed during the calcination process. Further modifications within the present model are required for successfully capturing the oxidation and lithiation phenomena.

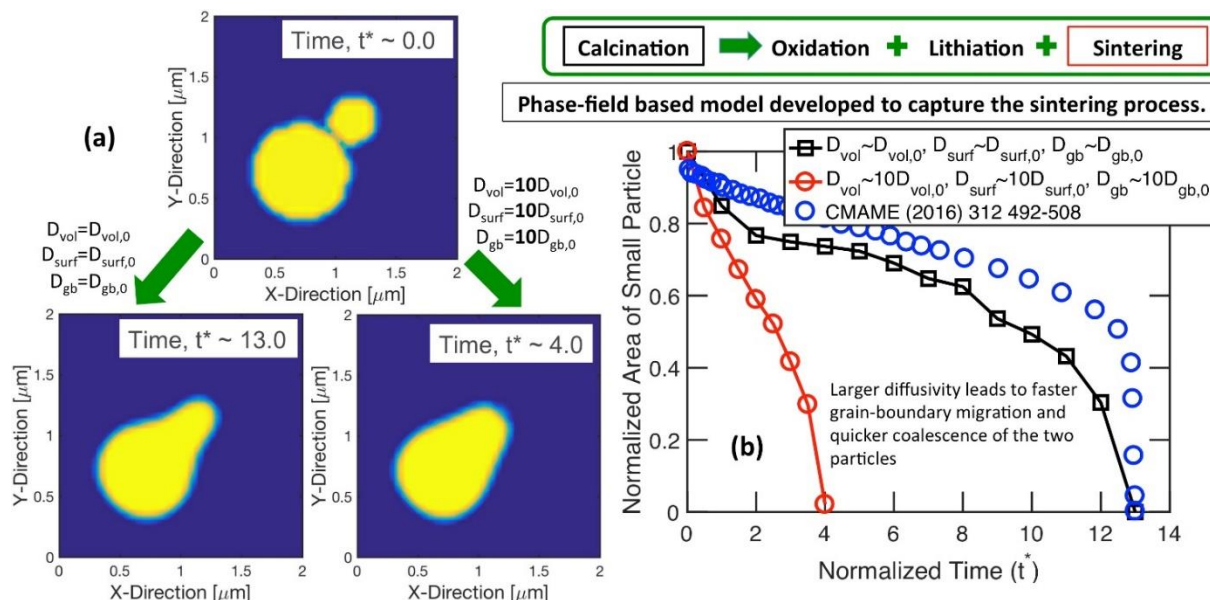


Figure 64. Coalescence of two particles as predicted by the phase-field based sintering model. (a) Initial (top) and final (bottom) shapes of the two adjacent particles as obtained after sintering with low (left-bottom) and high (right-bottom) diffusivity. (b) Decrease in size of the smaller particle with respect to time. Source: ANL and [4]

In the existing literature all the SEM images of hydroxide precursors look very much flocculated and not so dense. However, focused ion beam-SEM images of several NMC oxide cathode particles showed very dense secondary particles, with minimal inter-particle pore space. Also, size of the NMC oxide cathode primary particles appear to be much larger than that observed for NMC hydroxide precursors. There was ambiguity regarding the reason behind the increase in size of primary particles after calcination. Some scientists attributed it to Li insertion induced swelling, whereas, others tried to explain it as coalescence of multiple primary particles. Development of the sintering model unambiguously demonstrates that increase in size of the primary particles occur due to the grain-boundary migration and coalescence of multiple particles during the calcination process. Also, significant densification of the secondary particles occurs during calcination, which can be captured successfully by the sintering model. Through the present study, the importance of the sintering process in the formation of dense and high tap density secondary particles has been successfully demonstrated.

## R2R Water Project

### Argonne National Laboratory

During late FY 2016 and into FY 2017, EERE AMO proposed support to establish R&D efforts aimed to develop technologies leading to water from a variety of base sources, yielding "pipe purity" manufactured results. At a minimum, this "manufactured water" should use processes, materials, products and other production-related activities with an equivalent economic value. Energy and emissions "cost" of existing water

supplies should be on economic parity or better for any new system. To realize these goals, the introduction to the manufacturing process of highly-efficient, low-cost production technologies is needed. As such, it is recognized that high-value R2R processing technologies need to be incorporated along with high-performance computing integrated computational materials engineering approaches to enable predictive modeling that will aid in expedited process, materials, and equipment design. This project focused on the development of materials, processes and equipment to use to produce water for three primary uses: municipal fresh water, agricultural use, and industrial use (including, but not limited to the oil and gas sector). Given the diversity of water needs and respective requirements, there are multiple shared technical challenges that need to be addressed to envision demonstration of "pipe parity" approaches to clean water processing and production. This includes, not only processing water drawn from natural occurring and industrial process-generated sources, but also enabling process technology to be used in related wastewater treatment and water cleanup.

The objectives of this project are as follows:

1. Enable advanced materials process R&D, scale-up and synthesis for next generation water process and manufacturing materials including development of uniform, baseline materials that can be provided for industrial validation and to researchers for further development; development of a number of materials, processes, software tools and techniques that support and are compatible with higher speed and highly efficient R2R water manufacturing processes.
2. Create prototypes of water manufacturing processes, materials and membranes suitable to establish property sets envisioned to be used in data bases that support related materials design and development.
3. Develop tools and prototype devices to support scale up activities that are representative of potential commercial products envisioned to use the R2R technology as the primary manufacturing process.
4. Conduct efforts which potentially yield software tools to support and predict materials, process and device design and development.

The project included three efforts whose results are discussed below.

### **Development and Commissioning a Semi-Automation Assembly Line**

Three vendors were selected, and onsite visits were made to test their equipment. The properties of the materials processed by each equipment at the individual vendor were measured and/or characterized to compare to the specifications of current resin wafer material that was fabricated in the laboratory. Figure 65 (a) shows the blender and Figure 65 (b) shows the mixture of resin particles produced in the laboratory on the left and with the industrial blender on the right. The Intek IR oven that will be used for drying and curing is shown in Figure 66 (a) along with the temperature profile measured in the oven shown in Figure 66 (b). Figure 67 (a) shows the resin wafer cured using the IR oven and Figure 67 (b) illustrates the similar ionic conductivities of resin wafers made using the IR oven at the vendor's facility and using a hot press and a conventional oven in the laboratory. The IR oven reduces the curing time by 80% compared to the hot-press device.





(a)

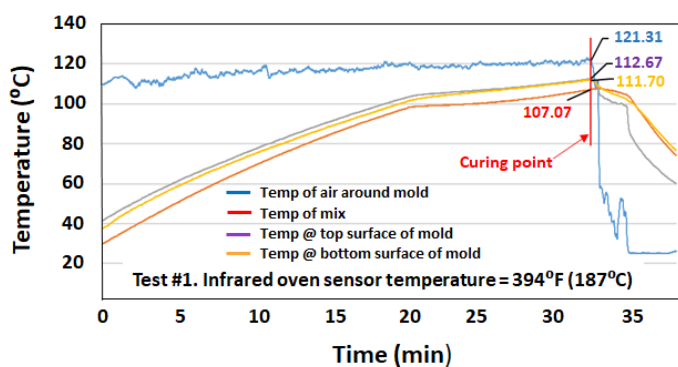


(b)

Figure 65. (a) Industrial blender equipment and (b) the particle mixtures from a laboratory blender and the industrial blender. Source: Eirich Machines



(a)



(b)

Figure 66. (a) IR oven and (b) the temperature profile measured in the oven. Source: Intek



(a)



(b)

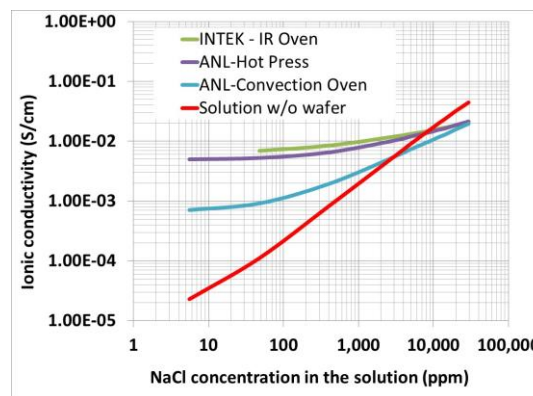


Figure 67. (a) Resin wafers fabricated using the IR oven and (b) the ionic conductivity for different processes. Source: ANL

A hi-bay space was allocated and commissioned (e.g., electricity, ventilation and etc.) to install the SAAL. Figure 68 shows the schematic of the SAAL design.

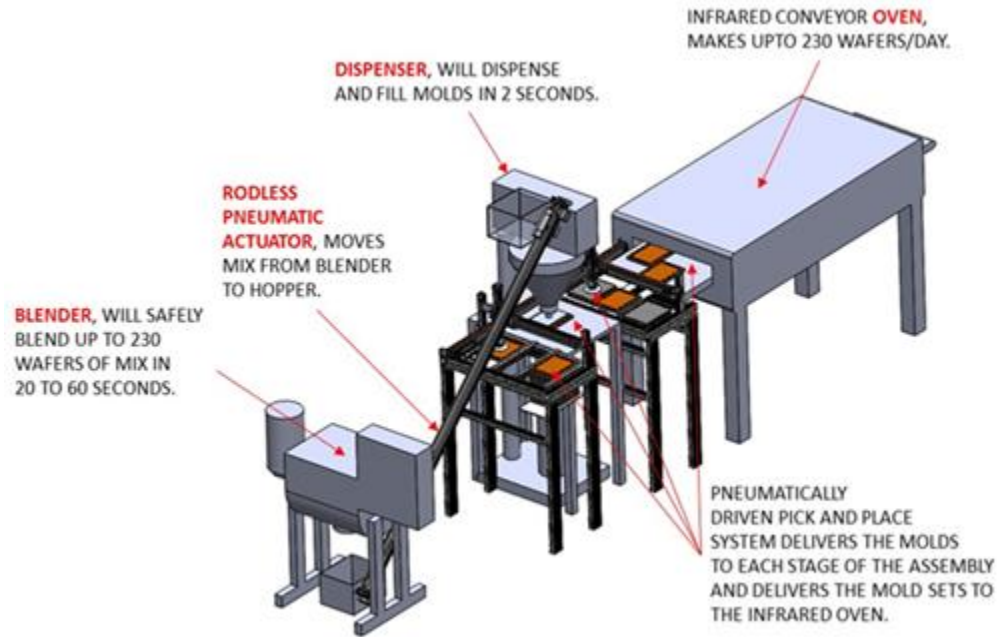


Figure 68. Schematic of the components for the SAAL design. Source: ANL

Figure 69 (a) shows the inline mixer, the lifter and the dispenser (yellow arrows) for the aligned equipment of the SAAL. Figure 69 (b) shows the location of the IR oven.



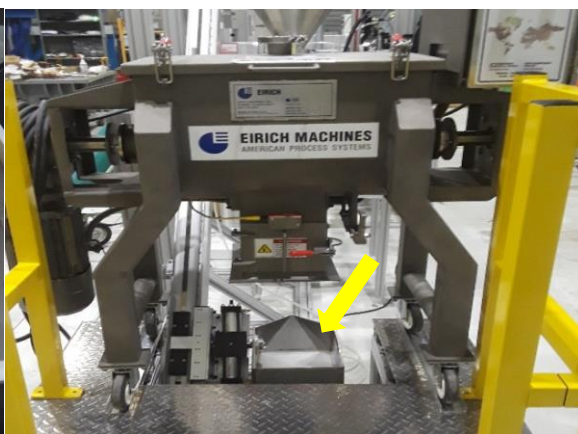
Figure 69. (a) Aligned equipment comprising the SAAL and (b) location of the IR oven. Source: ANL

Figures 70 shows the various stages of the operational testing of the individual components of the SAAL. First, the pretreated ion-exchange beads were poured into the mixer to uniformly mix the resin beads and polymer binder (Figure 70 (a)). The well-mixed resin beads and binder particles were lifted into the overhead inlet of dispenser where they are dropped into the underneath mixer box (Figure 70 (b) and (c)) and mixed particles in a bucket were lifted via the guiding arm and poured into the top of dispenser (Figure 70 (d)). The vertically moving dispenser uniformly sprays (disperse) the particles into the steel mold (Figure 70 (e) and (f)) before sending them into the IR oven for heat curing step to make the wafer (Figure 70 (g) and (h)). A temperature profile test of the IR oven was also conducted to fine tune the narrow temperature window needed to cure the wafer product.





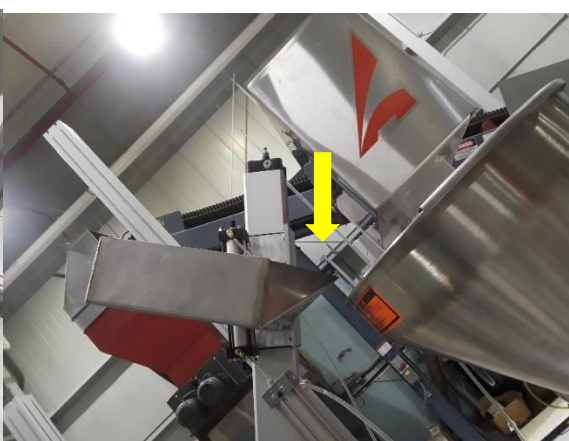
(a)



(b)



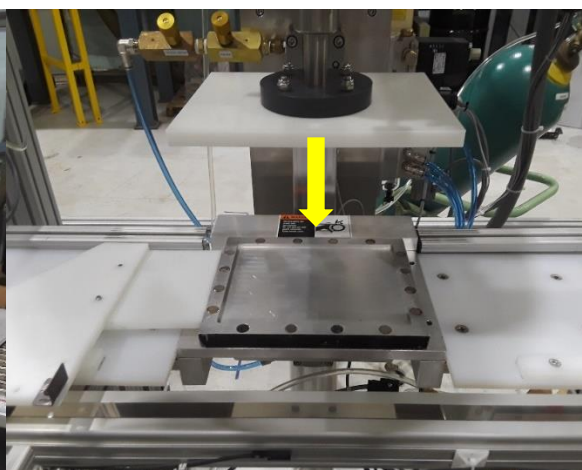
(c)



(d)



(e)



(f)





Figure 70. Various stages (a) through (h) of the operational testing of the individual components of the SAAL. Source: ANL

Five resin wafers were produced with different operational conditions in each step. Critical steps were identified that greatly influence the physical integrity of resin wafer. Preliminary characterization of the wafers was performed to measure their ionic conductivities using a proprietary electrochemical system and data analysis algorithm. Figure 71 (a) shows one of the wafers produced and Figure 71 (b) is a picture of the electrochemical characterization system.

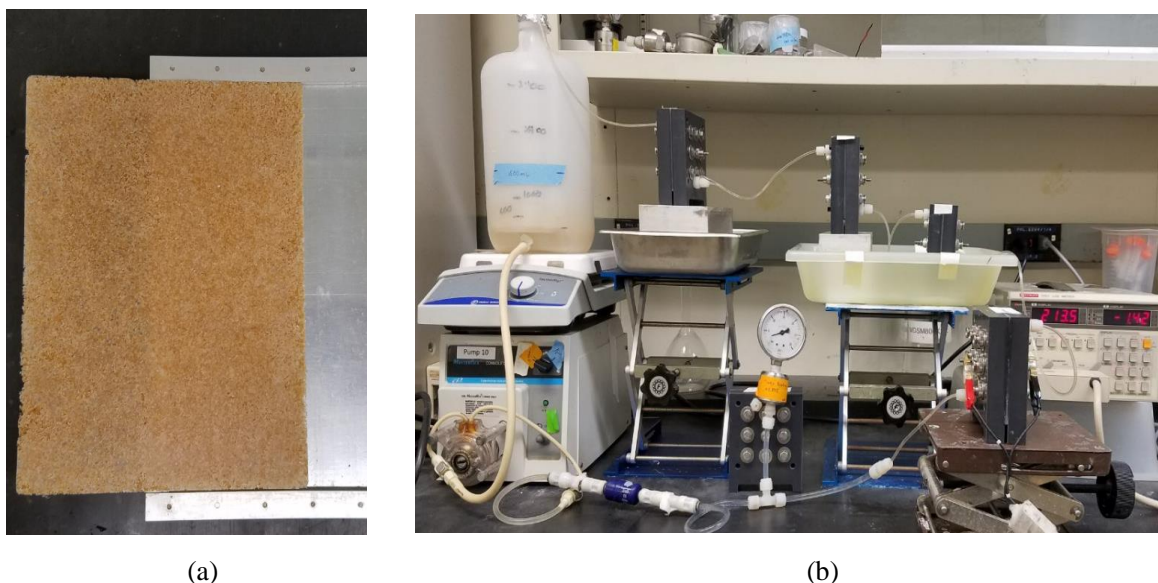


Figure 71. (a) A resin wafer made using the SAAL and (b) the characterization system to determine ionic conductivity of the wafer material. Source: ANL

The SAAL was officially commissioned and resin wafers were manufactured with different operational test parameters. All the PLC coding to control the SAAL was completed. More than 90 wafers were fabricated with very consistent physical integrity and wafer quality. There was an issue with the particle dispenser that prevented uniform distribution of the particles into the wafer molds. An alternative design and manufacture of an adaptor by the vendor was done to mitigate this issue. The troubleshooting of the SAAL was successful.

## Evaluation of the Manufactured Material for Water Processing

Characterization of the specific conductivity of the wafers was performed and all the wafers tested had equal or better conductivity when compared to the bench-mark wafer made by the laboratory hot-pressed method as shown by the data in Figure 72. Desalination testing of one of the wafers was performed the wafer made with the SAAL process showed a slightly better energy consumption of 0.64 kWh/m<sup>3</sup> versus 0.66 kWh/m<sup>3</sup> for the hot-pressed method. However, the desalination rate was less compared to the bench-mark wafer (6 gal/m<sup>2</sup>/hour for the SAAL versus 10 gal/m<sup>2</sup>/hour for the hot-pressed method). Testing of the flow distribution of these porous wafer materials was conducted as well as an evaluation of its water desalination performance using a larger scale electro-deionization system to confirm the desalination performance.

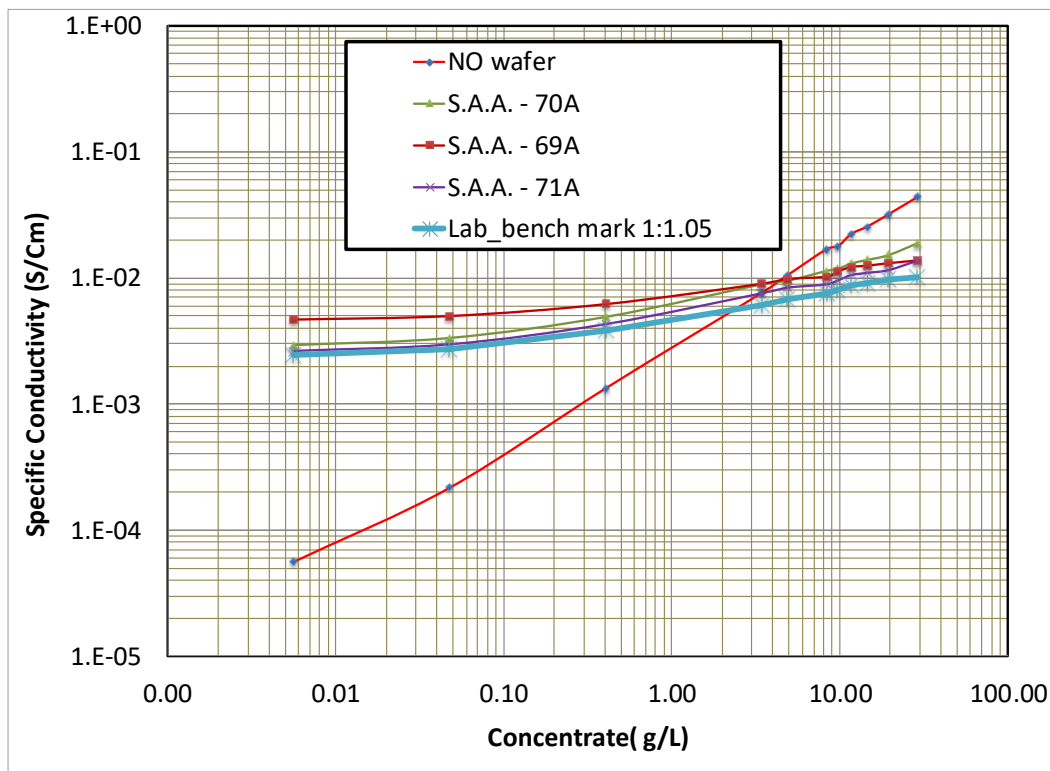


Figure 72. Specific conductivity for SAAL wafers compared to the benchmark wafer made with a hot-pressed method.  
Source: ANL

## Advanced Wafer Material Synthesis

The use of an ionomer binder to fabricate resin wafer was evaluated. The integrity of a dry ionomer-bonded resin wafer was good. However, after the wafer was soaked in water for a few hours (Figure 73 (a) through (c)), the resin wafer started to lose its integrity and eventually broke into pieces. This is due to the hydrophilic property of the ionomer that was dissolved in the water. New surface chemistry was formulated to reduce hydrophilicity of the ionomer binder.

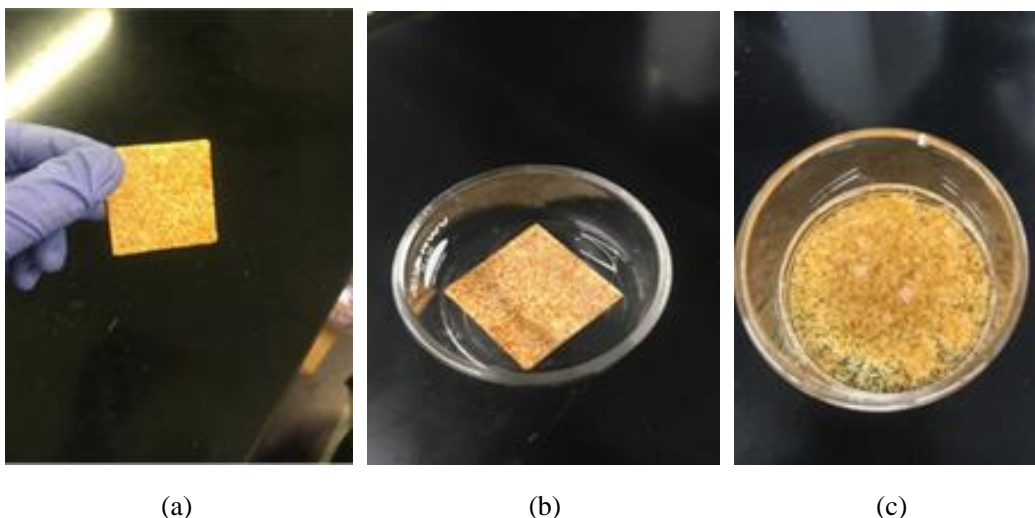


Figure 73. (a) Wafer made with an ionomer binder, (b) same wafer soaking in water and (c) wafer disintegrated. Source: ANL

A stable ionomer was identified that can produce water-stable resin wafers. Using a sulfonated polyether ether ketone (SPEEK) as cation-exchange ionomer binder, a stable resin wafer was produced as shown in Figure 74 (a) for the dry wafer and Figure 74 (b) for the wet wafer. Conductivity measurements of the new wafer made from the liquid binder has order-in-magnitude higher ionic conductivity than current poly ethylene binder wafer as shown in Figure 75.

The successful fabrication of a resin wafer using a liquid binder resolved the biggest hurdle of designing a full-scale R2R manufacturing process to produce resin wafers for industrial applications. The liquid binder completely eliminated engineering challenges of R2R fabrication using solid particles and resin binders.

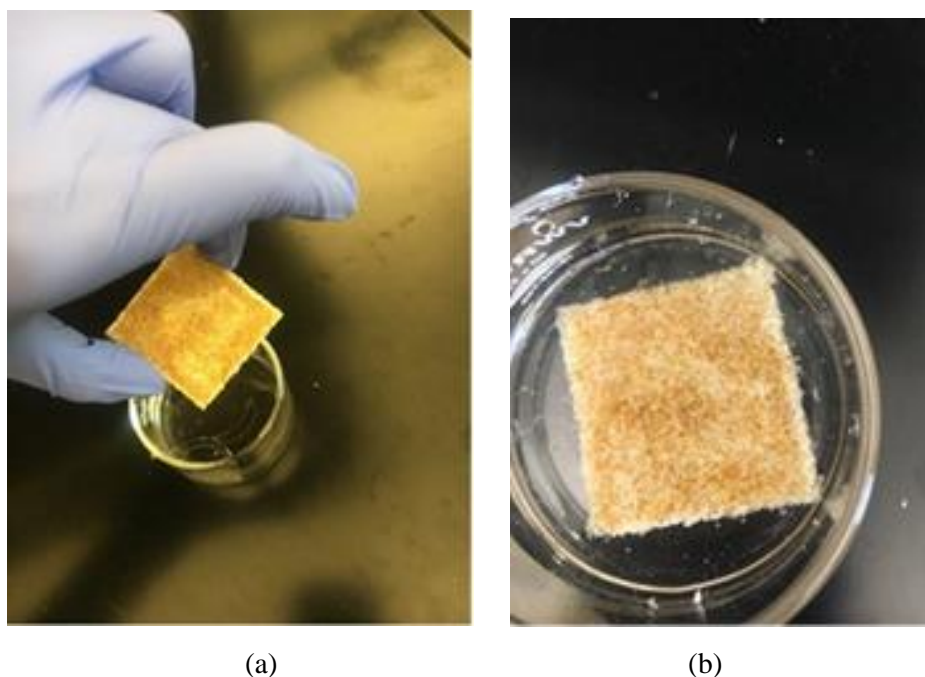


Figure 74. The resin wafer made with ionomer-bound resin beads (a) dry and (b) wet. Source: ANL

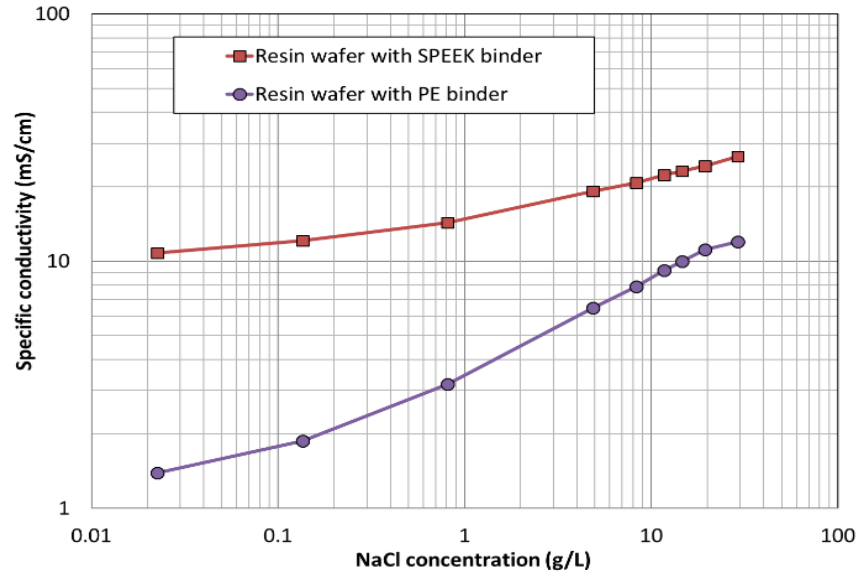


Figure 75. The ionic conductivity of a resin wafer made from a sulfonated poly-ether ether ketone. Source: ANL

Based on the experience of wafer fabrication using SAAL and the optimal property of resin wafers, the key parameters to design a fully automatic assembly line were defined and the conceptual design is shown in Figure 76.

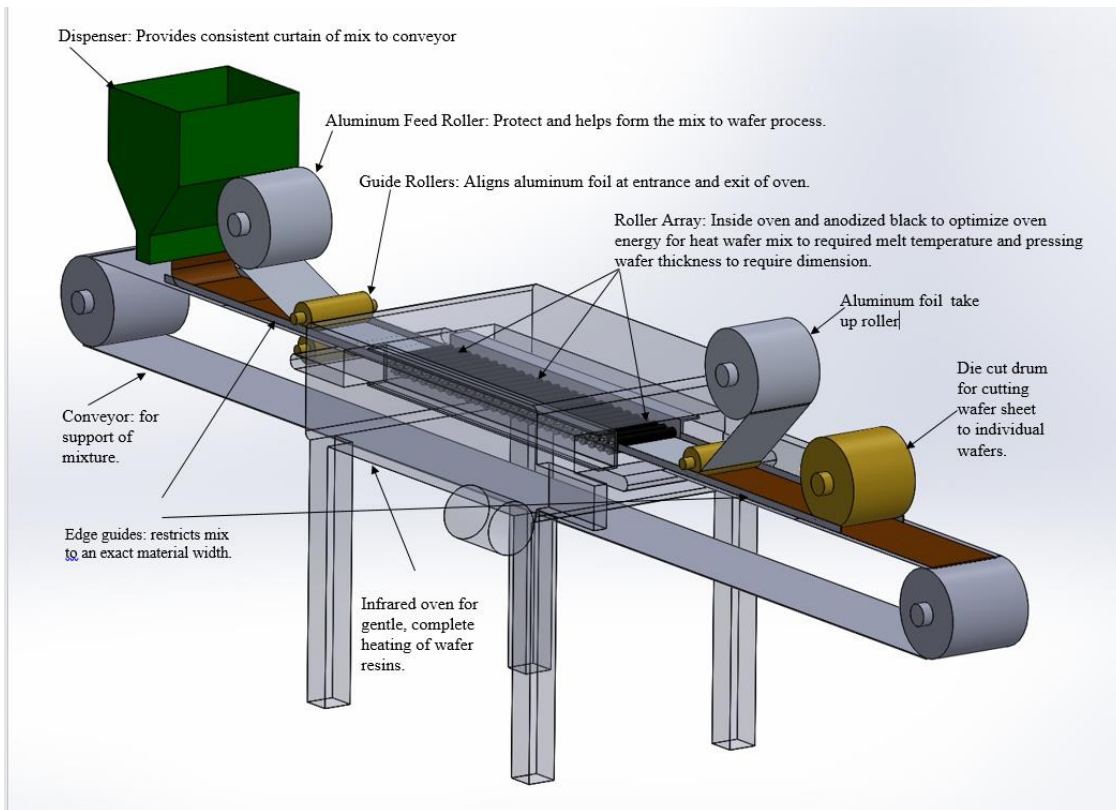


Figure 76. Conceptual design of a fully automatic assembly line for R2R manufacture of resin wafers. Source: ANL

The SAAL design has been improved and deviated slightly from the original wafer fabrication process to address automation issue of large-scale manufacture. After testing the system, we made major revisions to the wafer manufacture process from original process:

1. Solid Particles Mixing

Raw material preparation for mixture – Due to the inconsistency and difficulty to maintain a homogenous mixture of dry ion-exchange resin beads, water (to form moisture-saturated resin beads) and a new polymer binder was used in the procedure to prepare the raw ion-exchange beads received from the commercial vender. The impact was that adding water to the mixer equipment in the SAAL is no longer needed which simplifies the operation and provides the ability to produce a more uniform mixture of polymer binders and the moisture-control resin beads. The automatic particle mixing also reduce the operation time.

2. Particle Dispenser

The mixed particles were dispensed into a texture to the wafer mold using a controlled moving belt system. In original hot-pressed process, the mixed particles were dispensed into the mold and a different manual process is used for leveling the mold to ensure a uniform level and mixed particle distribution. The impact is that, compared to the manual process, dispensing particles into a moving bed provides more acute distribution of particles and results in a more uniform distribution of ion-exchange site and pores. This is critical to flow distribution during the operation of separations. Good flow distribution will reduce the foot-print of capital equipment. Good distribution of resin bead will improve energy efficiency for separations. Uniform distribution of the particle in the mold is one of the time consuming steps in current laboratory-scale hot-pressed process. It also contributes to the enhancement of manufacture rate.

3. Pressurization

Pressurized curing to form a porous wafer is one of the key parameters in original hot-pressed process. This is the major challenge in the SAAL as adapted from the hot-pressed process. Current SAAL design uses less pressure on the wafer mold. The impact is that the degree of pressurization may significantly change the structure of wafer porosity and the positions of ion-exchange sites that are two most important factors to the operation condition and separations performance.

4. Curing

Using an IR oven to replace the hot-surface press is the most distinct design difference from original hot-pressed process. The IR oven for curing of the polymer beads reduces 80% of curing time compared to hot-pressed process. The temperature profile of the wafer mold inside the IR oven can be controlled precisely and is very stable. This creates a stable and a more porous structure of the resin wafer. The impact is two-fold: 1) acute temperature control is important due to the narrow curing temperature windows to form a resin wafer with maximum ion-exchange property and 2) good porous wafer structure will improve the energy consumption and increase separations productivity resulting smaller foot-print of separations system

### **Impact of Resin Wafer Semi-Automated Assembly Line on Enabling the Industrial Applications of Resin Wafer Electro-Deionization Technology**

The SAAL can produce an adequate wafer material with significantly reduced processing time and cost for industrial applications beside water purification, e.g., chemicals purification, biofuel, biochemical separations and recovery. Based on our assessment of water desalination needed for the industrial cooling water tower from small-scale used in an institutional system to large-scale in a power plant, the current SAAL design



provides a significant pathway to reduce the challenges for industrial applications. Using a single manufacturing system operated in ANL, Figure 77 and Figure 78 show the comparison of the time and labor cost needed to produce the wafers using conventional hot-press and the SAAL to support cooling tower water supply for a small system of 4 gpm used in institutes or a large system of 500 gpm used in electric power plant s(e.g., 500 MW). Figure 77 shows very clearly the hot-pressed manufacturing method cannot supply the resin wafers both in time and cost compared to the RW-EDI system to process cooling water in a power plant. Figure 79 shows the estimated operation costs of resin wafer manufacture using the hot-pressed method and the SAAL. The SAAL reduces significantly the manufacturing cost that is close to the target wafer cost used in a techno-economic analysis of the RW-EDI process for water purification and other separation applications. The manufacturing cost estimation includes the costs of raw material, energy consumption and labor.

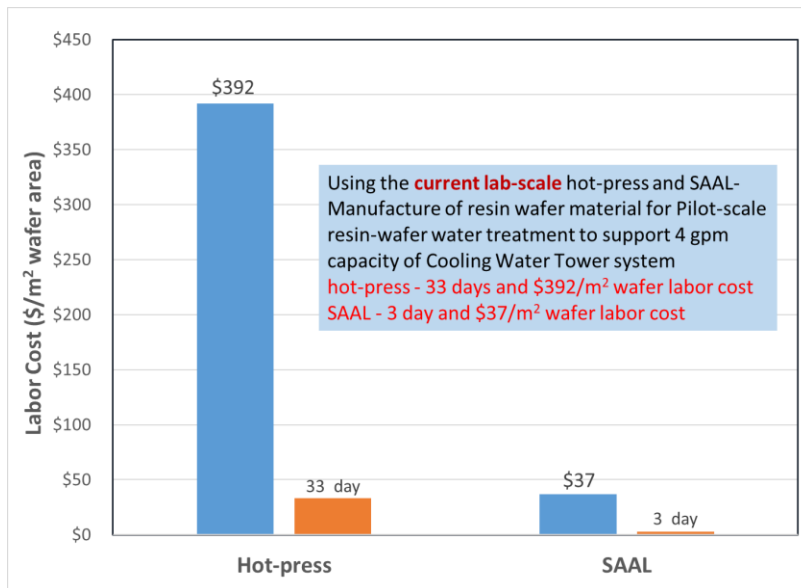


Figure 77. Comparison of manufacturing time and labor cost needed to manufacture resin wafer material for a small-scale cooling water system. Source: ANL

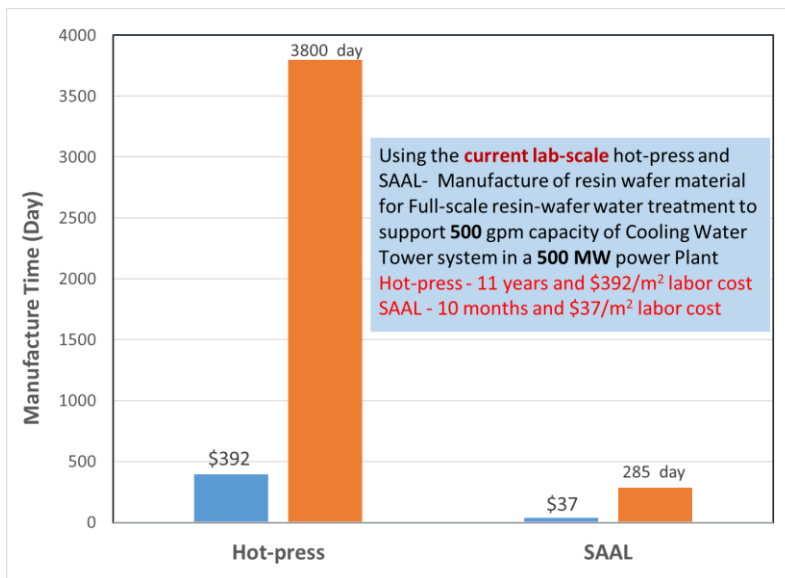


Figure 78. Comparison of manufacture time and labor cost needed to manufacture resin wafer material for a large-scale cooling water system. Source: ANL

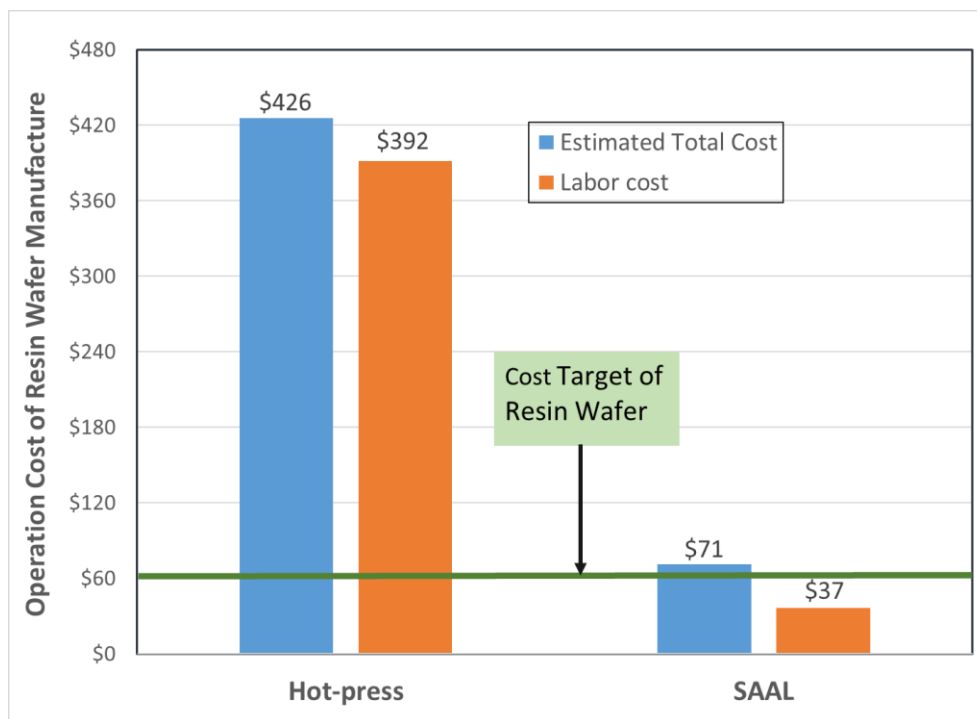


Figure 79. Comparison of cost of operation to produce resin wafer material. Source: ANL

## Collaboration/Coordination/Outreach/CRADA

### Core program

The consortium continues to extend its efforts for collaboration, coordination and outreach to the partner laboratories, industry and academia through the various meetings and attendance at review meetings, conferences and symposia. The R2R AMM DOE Team Leads and Team members participated in biweekly project conference calls along with AMO and FCTO Program Managers; the FY 2017 Program Review and FY 2018 Project Planning meeting at Kodak EBP on October 31, 2017; the FY 2018 Kickoff Meeting with the AMO Program Manager at NREL on January 25, 2018; an AMO Program Manage site visit at ORNL on May 1, 2018; a review of FY 2018 efforts and proposed future efforts was presented to the AMO Director on May 19, 2018; the Hydrogen and Fuel Cells Annual Merit Review on June 14, 2018; the AMO Peer Review on July 17, 2018; and the FY 2018 Program Review meeting at ANL on September 11, 2018. Lab Leads and principal investigators for each project task and three industry CRADA projects contributed to the FY 2018 Final Report.

ANL collaborated closely with researchers at the APS at ANL to conduct USAXS experiments to determine the evolution of primary particles during the materials fabrication process. Scientists at the MERF at ANL were collaborated with to understand the working principle.

ORNL collaborated with the other Consortium Labs to complete testing of matched electrodes for improved batteries and to develop the core plan for FY 2018 Fuel Cell Study.

NREL interacted with ORNL on ink studies, dual-slot coating and high-resolution electron microscopy, and interacted with ANL for the USAXS and XCT advanced characterizations.



LBNL collaborated with NREL and ORNL to redirect efforts for modeling and simulation of battery electrode materials to focus on developing a modified slurry model that describes NREL's fuel cell inks since the physical phenomena governing ink behavior have not been fully determined. LBNL also collaborated with partner laboratories to develop a data mining algorithm that traverses each sentence in a technical article paragraph word by word and classifies them according to the following categories: not operation, start of synthesis, heating operation, mixing operation, drying operation, shaping operation and quenching operation. These classes represent the most important steps of most materials synthesis processes.

## CRADA Projects

Three CRADA projects were initiated in FY 2018 based on proposals received on a Development Assistance Opportunity for R2R Advanced Energy Materials Manufacturing as a CRADA Solicitation No. R2RAMM-2017-02-02. One project with Proton OnSite was still awaiting approval at the end of FY 2018. Since the three projects that were selected began late into the fiscal year, a brief description of progress follows.

### Fisker, Inc.

Fisker, Inc. has partnered with LBNL and ORNL to demonstrate all-solid-state LIBs based on LLZO separators and cathode scaffolds that will allow scaling of freeze tape casting process to the pilot level at ORNL.

LBNL focused on investigating processing parameters for producing dense and porous green tapes of LLZO which when combined can form dense/porous bi-layers. The same efforts were made at Fisker in parallel, and some samples were shipped to LBNL and ORNL for cell assembly and characterization.

Green tape for dense LLZO layer was successfully demonstrated by LBNL. Commercial LLZO powder along with other industry standard tape-casting chemicals were used. High density LLZO films < 30  $\mu\text{m}$  thick were achieved on sintering to 1070°C/2 h. Figure 80 (a) is a picture of the LLZO green tape and Figure 80 (b) is a SEM image of the fracture surface of a sintered LLZO film. Common LLZO sintering involves extended sintering times >10 h at temperatures >1100°C. Short sintering time and lower temperatures have been achieved only by hot-pressing or when flame made nanopowders were used. LBNL demonstrated that even commercial ball-milled LLZO powders, when processed properly, can result in relatively low energy sintering. Green tapes of dense LLZO layer produced at LBNL were shared with Fisker and ORNL. There were reproducibility issues as the furnaces used by each party are different. This may require equipment calibration, heating schedule adjustment, and other changes.

Two batches of flame spray pyrolysis synthesized LLZO from MERF at ANL were tested for thin-film processing and sintering. Green tapes were readily produced but dense, thin films on sintering could not be achieved. Exaggerated grain growth and round rather than faceted grain boundary morphologies were observed suggesting excessive liquid phase sintering.

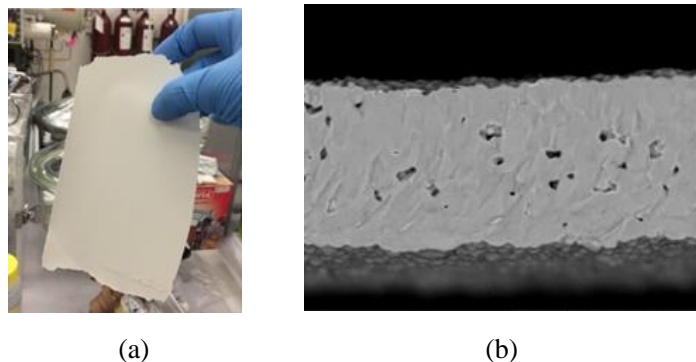


Figure 80. (a) Typical LLZO green tape. (b) SEM fracture surface image of sintered LLZO film. Source: LBNL

Iterations of freeze tape casting based on formulation shared by Montana State University (collaboration through Battery 500 Seedling project) were performed by LBNL. Aqueous slurries containing 7.5 – 10 vol.% of LLZO with binder, thickener, along with other additives were freeze tape cast at thicknesses of several hundred microns. Figures 81 (a) and (b) show 7.5 vol.% LLZO slurry freeze tape cast at 400  $\mu\text{m}$  and 10 vol.% LLZO slurry freeze tape cast at 200  $\mu\text{m}$ , respectively. The 7.5 vol.% LLZO sample shows higher porosity than the 10 vol.% sample as expected. Vertical pore alignment is observed in both but with significant bridging among the LLZO pillars which may interrupt the infiltration of  $\text{LiNi}_{0.6}\text{Mn}_{0.2}\text{Co}_{0.2}\text{O}_2$  (NMC622) cathode particles. Surface drying during freeze tape casting process was found to be problematic as shown in Figure 81 (c). This may be alleviated by generating a wet environment during freeze tape casting.

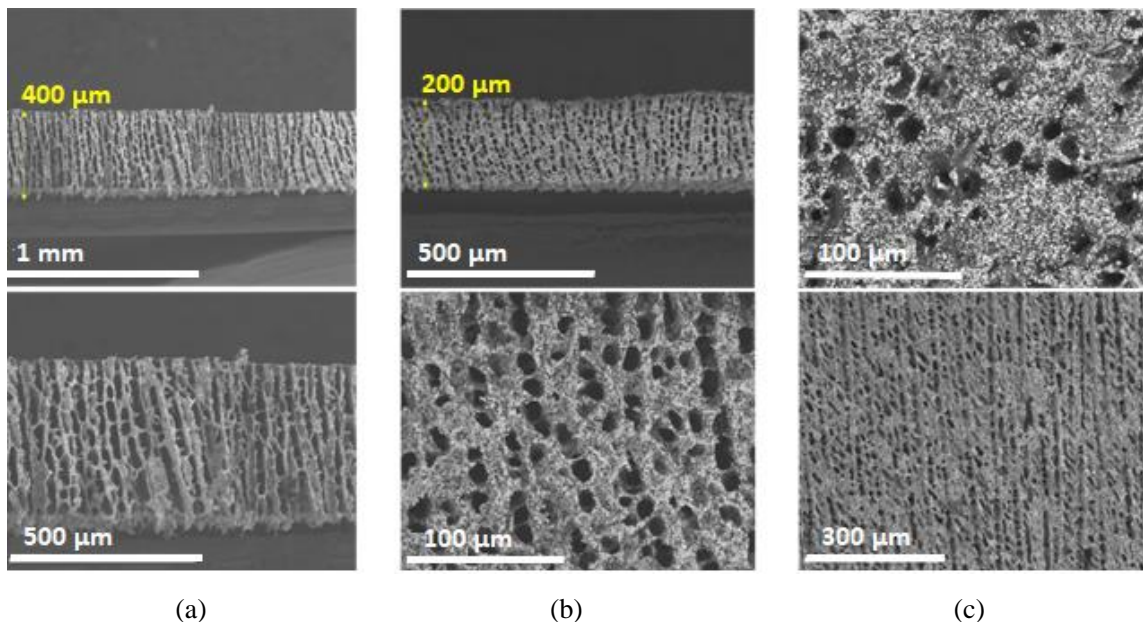


Figure 81. (a) Freeze tape cast 7.5 vol.% LLZO slurry. (b) Freeze tape cast 10 vol.% LLZO slurry. (c) Top surface (top) and bottom surface (bottom) of freeze tape cast 10 vol.% LLZO slurry. All images are of green tapes. Source: LBNL

The dispersion stability of the LLZO slurry was quite low, such that powder flocculation was observed in 10-20 mins into casting. The SEM images in Figure 81 are obtained from the initial part of the cast tape. Stability improvement is necessary for a longer cast. The pH control approach and other dispersants to replace the currently used Darvan C-N were investigated but both were unsuccessful. Increasing the viscosity by introducing more thickener to defer the time of noticeable flocculation is currently being investigated, which may serve as an intermediate solution.

Sintered bi-layers provided by Fisker were infiltrated with NMC622/Carbon black/PVDF mixtures, using NMP solvent. The mixture was added dropwise onto the porous side of the LLZO bilayer. Due to the low volatility of NMP, only a limited amount of mixture could be introduced. The empty space shown in Figure 82 (a) and (b) represents the approximate solvent volume. The dense layer was not fully dense compared to when sintered by itself (see Figure 80 (b)) and showed open porosity. The sintering schedule and infiltration method require further optimization. NMC622 seems to be well bonded to the LLZO surface.

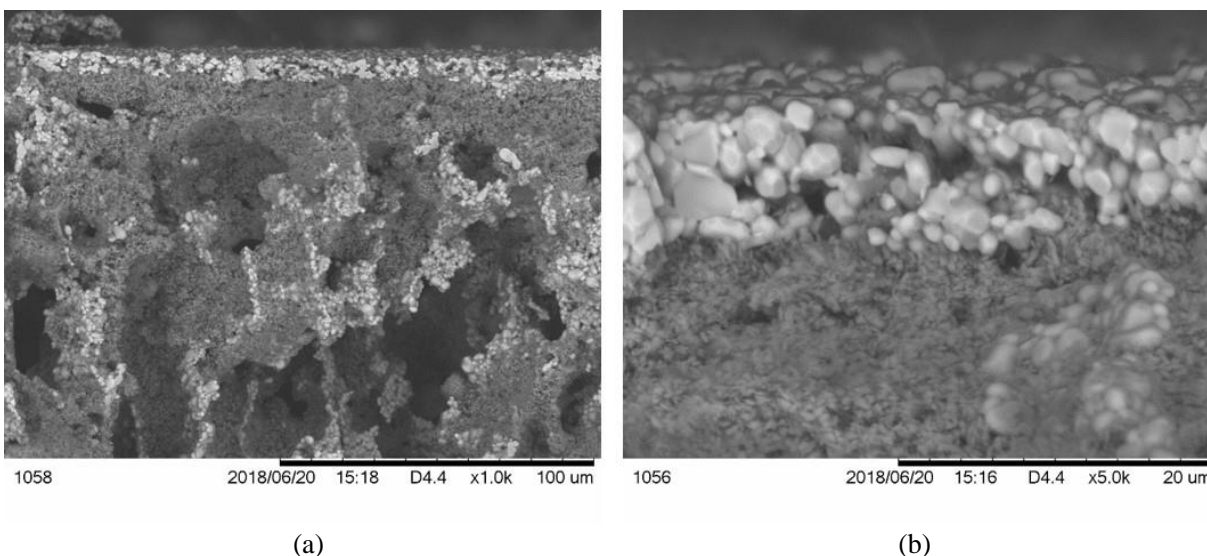


Figure 82. Two SEM fracture surface images (a) with low magnification and (b) high magnification of NMC622/carbon black/PVDF infiltrated dense/porous LLZO bilayer. Source: LBNL

During the project kick-off meeting, methods for modifying the tape-caster at ORNL to use it as a freeze tape-caster were discussed. A freeze tape-casting expert from Glacigen was also consulted for input but it was later determined that the modification is not suitable at the early stages of development. Hence, ORNL purchased a countertop freeze tape-caster from Glacigen for use in the laboratory. Modifications to the ORNL tape caster may be necessary when the processing variables are narrowed down and when the required experimental conditions become clear.

ORNL received the freeze tape caster during the second quarter of FY 2018 and a training session occurred in early August. Several personnel from Fisker, along with their industrial partners, visited ORNL in April 2018 and several coin cells and pouch cells were assembled and tested for electrochemical performance. Figure 83 shows rate performance of a hybrid cell consisting of a NMC622 infiltrated into a porous LLZO scaffold and a Li metal anode separated by a partially dense LLZO solid state electrolyte. A small amount of liquid electrolyte (1.2 M LiPF<sub>6</sub> in EC/EMC 3:7 wt.) was added to form the hybrid coin cell. The cell went through rate performance and cycle life test at C/3 at 30°C. As shown in Figure 83, the cell demonstrates pretty good rate performance and high coulombic efficiency. Cycle life test data is shown in Figure 84. The cell shows high coulombic efficiency (>99 %) and a capacity retention of 88 % after 150 cycles. Voltage profiles are shown in Figure 85 as a function of cycle number. The capacity fade and resistance increase can be clearly seen from the curves. Electrochemical impedance spectroscopy (EIS) was utilized to monitor cell impedance. The EIS was recorded at 3.6 V (discharge state) from 300 kHz to 10 mHz with 5 mV amplitude as shown in Figure 86.

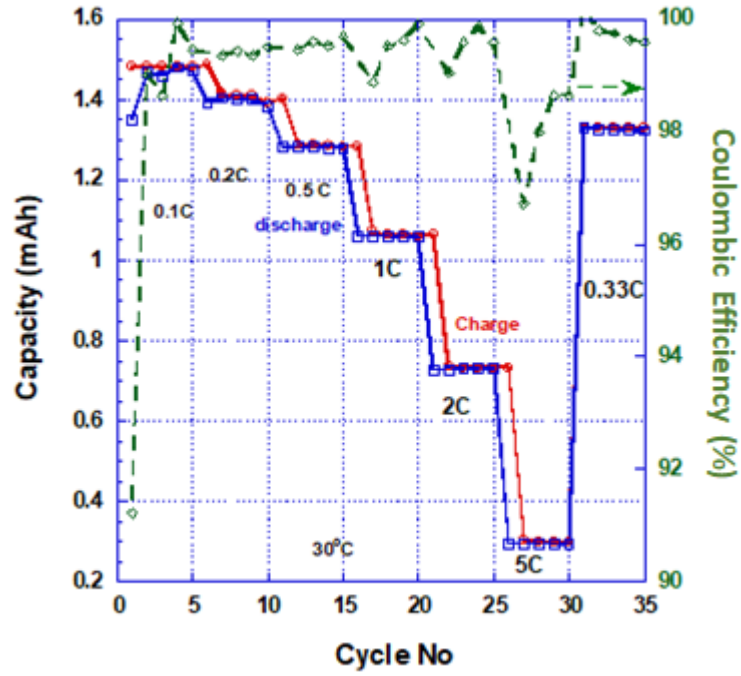


Figure 83. Rate performance of the hybrid coin cell. Source: LBNL

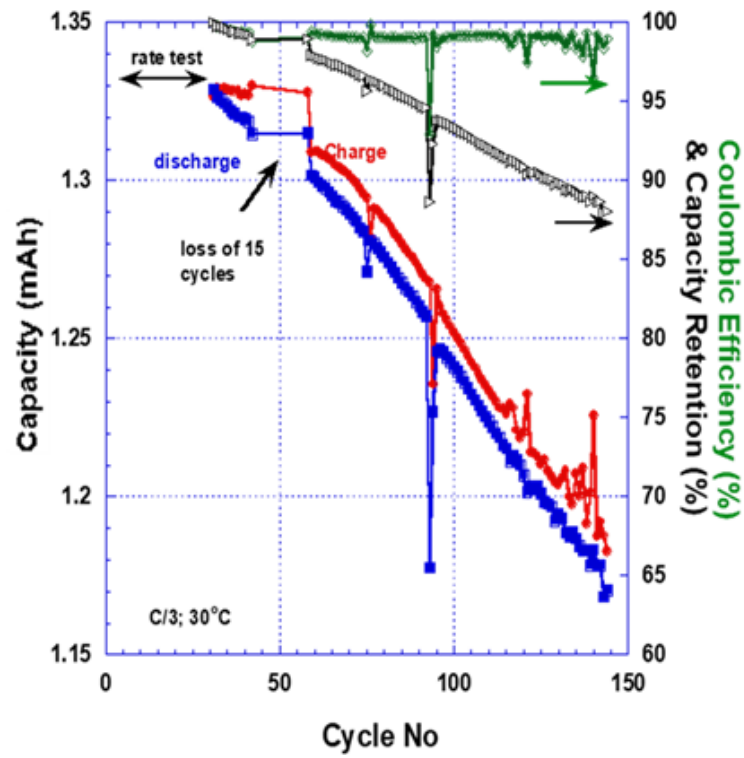


Figure 84. Cycle life test of the hybrid coin cell. Source: LBNL

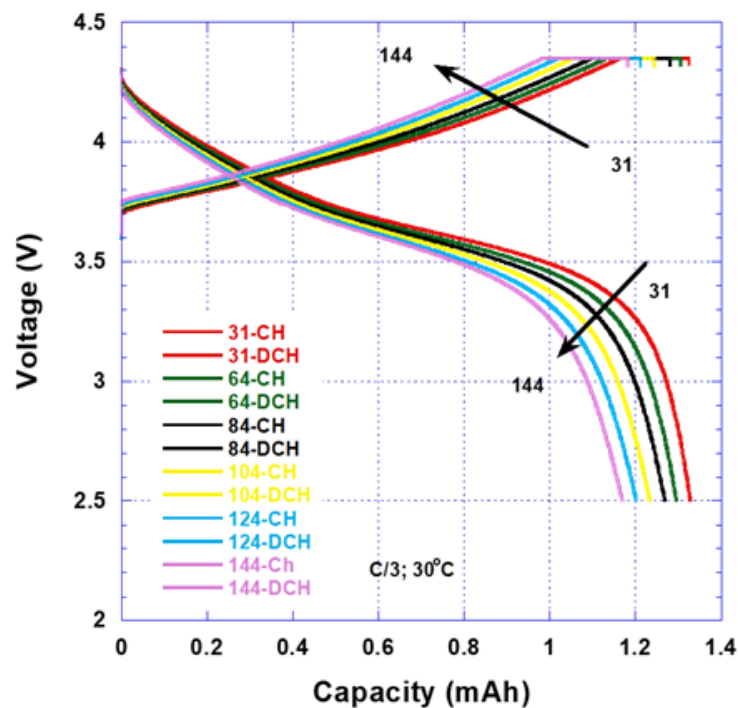


Figure 85. Voltage profiles. Source: LBNL

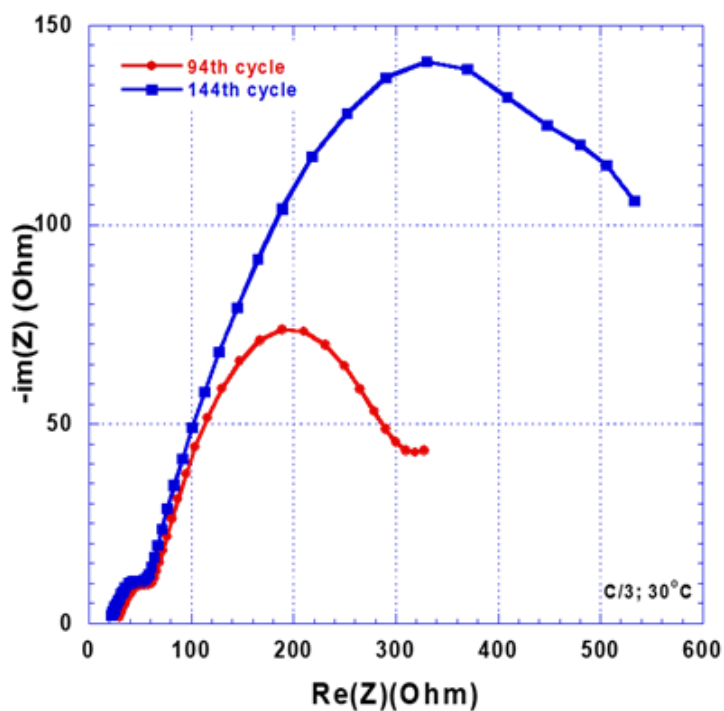


Figure 86. EIS profiles. Source: LBNL

Ohmic resistance, EIS intercepts with the real axis in the high-frequency region, is constant at the 94<sup>th</sup> and 144<sup>th</sup> cycles. This involves resistances from Li ion transport through the electrolyte and from electron transport



through the electrodes, current collectors, cables, and lead clips between the cell and potentiostat. The semicircles at the high-to-medium frequency region are related to electrolyte interphase resistance and attributed to impedances from Li ion migration through the surface films, which shows a significant increase at the 144<sup>th</sup> cycle compared to that at the 94<sup>th</sup> cycle.

ORNL also investigated the stability of a proprietary Li thin film, supplied by Fisker, under a dry room environment to determine the feasibility of assembly for solid state pouch cells. Morphology of the Li foil was captured using an optical microscope and is shown in Figure 87. There is no significant change in morphology after 240 min indicating that the Li foil is stable under the dry room environment (RH<0.1%). The next step was to investigate its electrochemical performance.

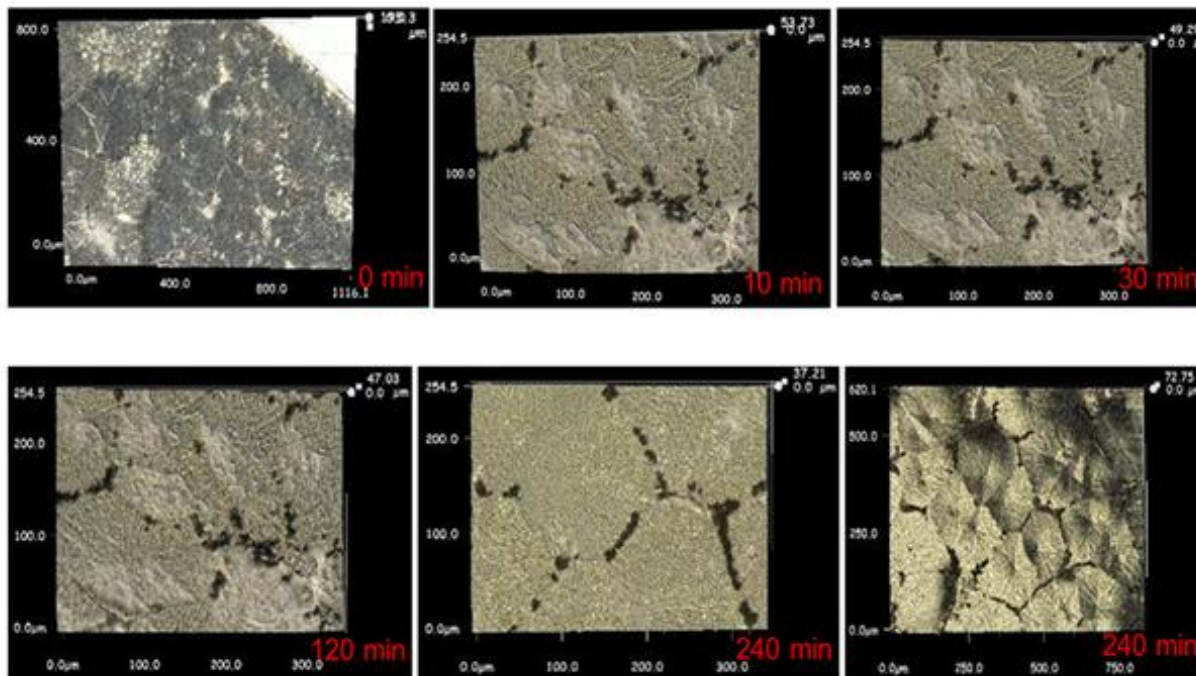


Figure 87. Morphology of a proprietary Li foil stored in a dry room at time intervals up to 240 mins. Source: ORNL

Several 4 cm by 4 cm porous LLZO scaffolds were supplied by Fisker to ORNL. These scaffolds were infiltrated at ORNL with the standard NMC622 cathode slurry via drop casting. These steps are shown pictorially in Figure 88. Small prototype hybrid pouch cells were assembled using the proprietary Li thin film anode and the cathode infiltrated porous LLZO scaffold. Li foil and cathode-LLZO assembly were separated with a Celgard 2325 separator and ~200 mg of liquid electrolyte (1.2 M LiPF<sub>6</sub> in EC/EMC 3:7 wt.) was added to each hybrid cell.

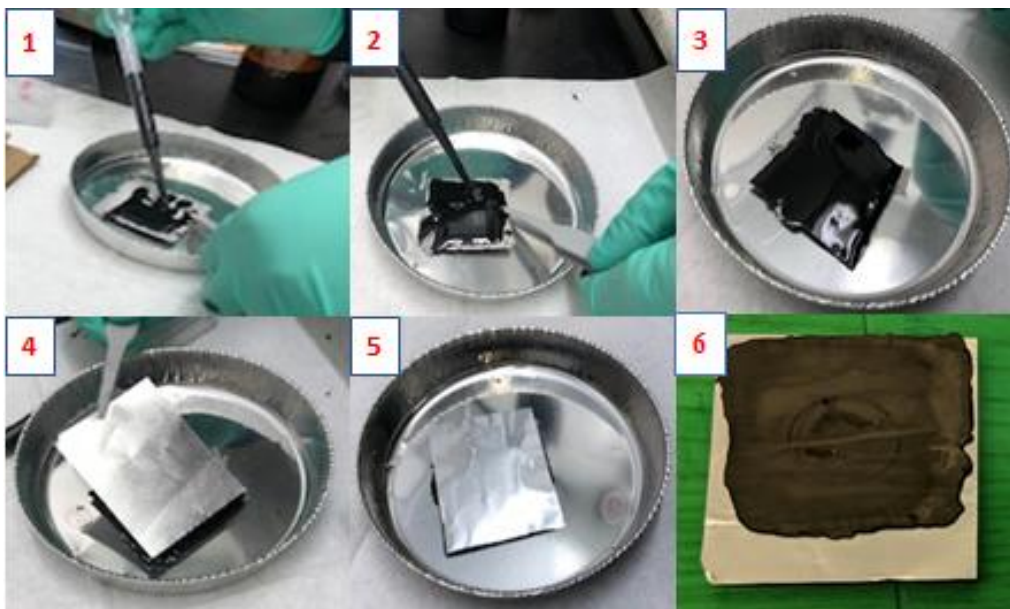


Figure 88. Steps 1 through 3 shows cathode slurry infiltration into porous LLZO scaffolds via drop casting. Steps 4 and 5 shows attachment of the aluminum current collector. Step 6 is final assembly after drying. Source: ORNL

Figure 89 shows the rate-performance of one of the hybrid pouch cells. The cells were cycled between 2.5–4.35 V with a 2 h hold at the upper cut-off voltage. The cell performed well at the initial low rate cycling (0.1C) to give a specific discharge capacity of  $\sim 180 \text{ mAh g}^{-1}$ . However, the capacity declined rapidly as the charge/discharge rate were increased, falling to almost zero at 1C rate. When the cell was cycled again at 0.1C after the 1C cycling, no capacity could be recovered.

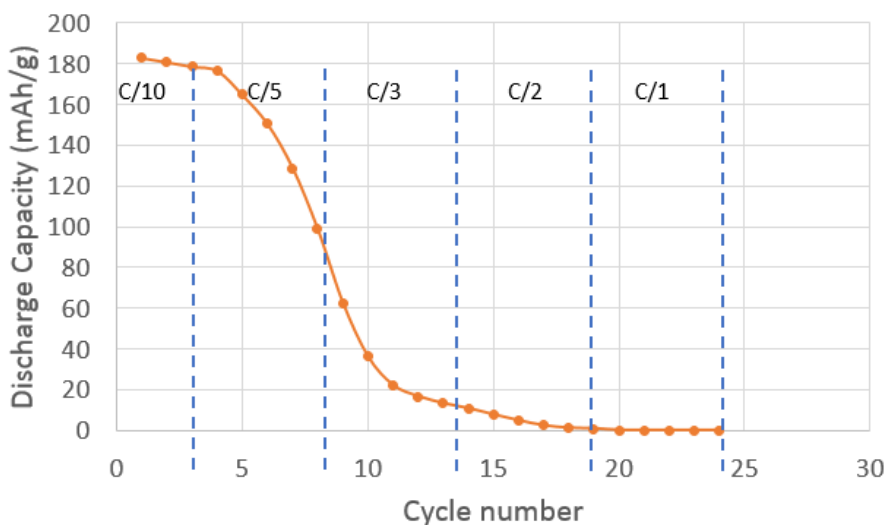


Figure 89. Rate performance of a hybrid pouch cell cycled between 2.5 – 4.35 V with a 2 hour hold at upper cut-off voltage. Source: ORNL

To test the cause behind this rapid performance decline, the cells were opened, and the components were visually inspected. While the cathode-LLZO assembly showed no apparent degradation such as delamination from aluminum current collector or fracture as seen in Figures 90 (a) through Figure 90 (c), the Li foil showed dramatic color change, delamination from the copper substrate as well as crumbling into smaller pieces as shown in Figure 90 (d) through Figure 90 (f). This suggests irreversible consumption of cyclable Li at the Li foil to form decomposition products.



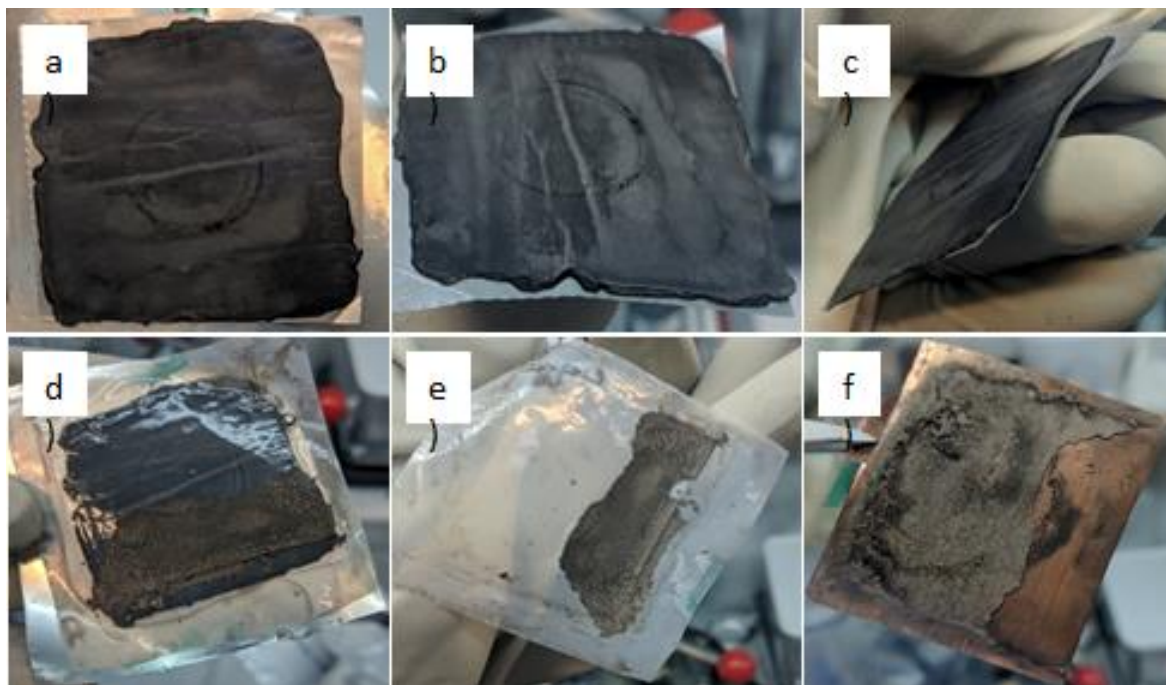


Figure 90. Photographs of the hybrid pouch cell components after the rate performance test. (a-c) show the cycled cathode-LLZO assembly, and (d-f) show the cycled proprietary Li foil. Source: ORNL

To test this hypothesis, we paired the extracted cathode-LLZO assembly (unrinsed) with regular Li foil and made hybrid coin cells with fresh liquid electrolyte and Celgard separator. Before assembly, the 4 cm by 4 cm assembly was randomly cut into small pieces using a ceramic scissor so as to fit inside a coin cell. Figure 91 shows the rate performance of one of the cells. The cell was cycled between 2.5-3.45 V with a 2 h hold at upper cut-off voltage. In the plot, only absolute cell capacity is presented as it was difficult to estimate the active material loading due to irregular shape of the LLZO-cathode piece. As can be seen, the cell performed significantly better with the discharge capacity reduction of only 18% going from 0.1C to 1C.

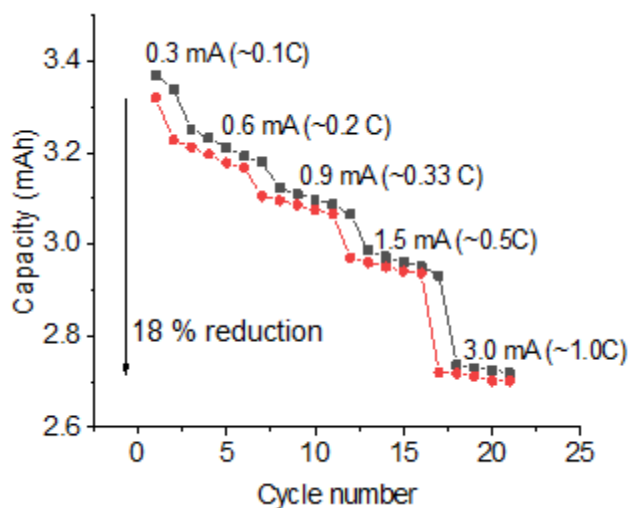


Figure 91. Rate performance of a coin cell containing a cycled cathode-LLZO piece, paired with a fresh regular Li metal disc, fresh liquid electrolyte and a Celgard separator. Source: ORNL

Several collaborative efforts occurred during FY 2018 on the Fisker CRADA project. Freeze tape casting formulation shared by Montana State University was transferred to Fisker and ORNL. ORNL constructed

hybrid pouch cells using thin Li foils (30  $\mu\text{m}$  deposited on Cu foil) supplied by Fisker. ORNL performed SEM characterization of LLZO bilayer from Fisker. Fisker supplied 15  $\mu\text{m}$  thick LLZO green tapes to LBNL for sintering studies. Dilatometry experiments were carried out at LBNL to obtain densification profiles of the LLZO powder on heating, which the raw data was shared with Fisker as they have a modeling effort to predict densification rate at selected sintering temperatures. Fisker supplied a commercial mixed electronic/ionic conducting polymer electrolyte to LBNL.

### **Navitas Systems, Inc.**

Navitas Systems, Inc. has partnered with ORNL and NREL to demonstrate R2R production of an advanced separator for Li ion batteries. The project began in March 2018 due to a delay in funding allocation.

#### **R2R Production of Advanced Separators and Lithium Ion Batteries**

A project kick-off meeting took place at Navitas Systems, LLC on May 11, 2018, where the principal investigators of the contractors, Dr. Jianlin Li from ORNL and Dr. Michael Ulsh from NREL, met with the principal investigator of the industry partner, Dr. Chris Silkowski, from Navitas Systems. The lab participants toured the facility and observed the operation of the new cell assembly line at Navitas, which helped them better understand how the final product in this CRADA project will be processed and assembled. The three parties finalized an experimental plan.

Navitas down-selected two baseline separators which met their requirements on lamination capability and mechanical properties. Navitas provided samples of the two baseline separators to ORNL in June 2018. Their electrochemical stability was investigated via cyclic voltammetry (CV) between 2.5 and 4.6 V, at 0.1 mV/s in half coin cells with NMC622 and Li metal as the working and counter electrode, respectively.

Figure 92 (a) through (e) show the CV curves of the NMC 622 with various separators. Most of the cells show similar behavior and the characteristic redox peaks of NMC 622. There current density in the 4<sup>th</sup> cycle of the Celgard 2325-1 and Entek-1 was much larger, which could indicate formation of a local short circuit. More coin cells were assembled to repeat the experiment. Figure 93 (a) and (b) compares the CV curves at the 1<sup>st</sup> and 4<sup>th</sup> cycles with various separators respectively. The oxidation peak in the 1<sup>st</sup> cycles was relatively broad, and the potential varied which could be due to some absorbent on the separator which was oxidized or interaction between separators and electrolyte. In the 4<sup>th</sup> cycles, they were more aligned and much narrower. The current intensity was slightly higher for the cells with Celgard and Teijen separator indicating superior mass transport. There seemed other reactions in the cell with Entek 1 as shown in the spurs in peaks around 4.5V.

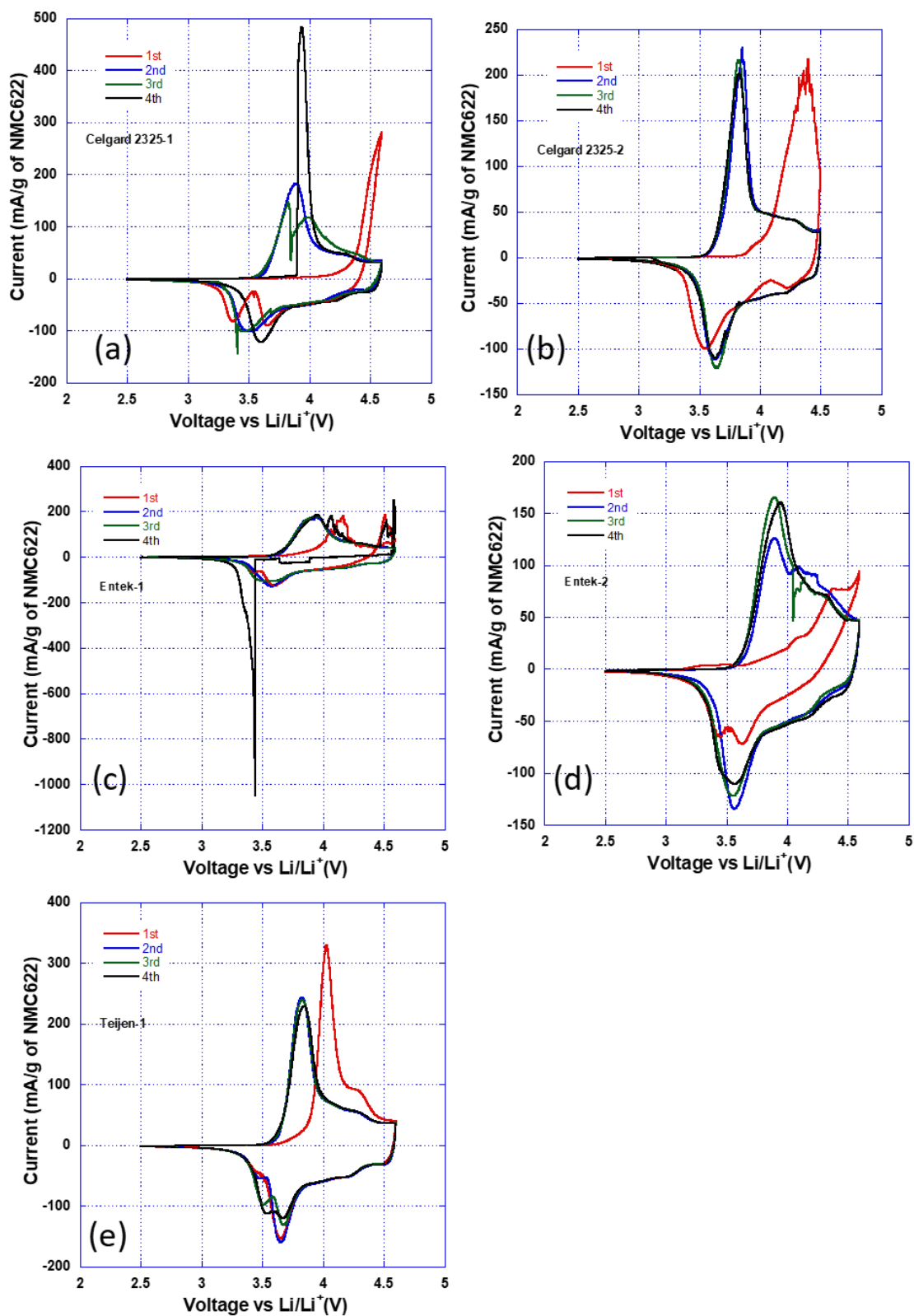


Figure 92. Cyclic voltammety curves of NMC 622 half coin cells with various separators: (a) and (b) Celgard 2325, (c) and (d) Entek and (e) Teijen. Source: ORNL

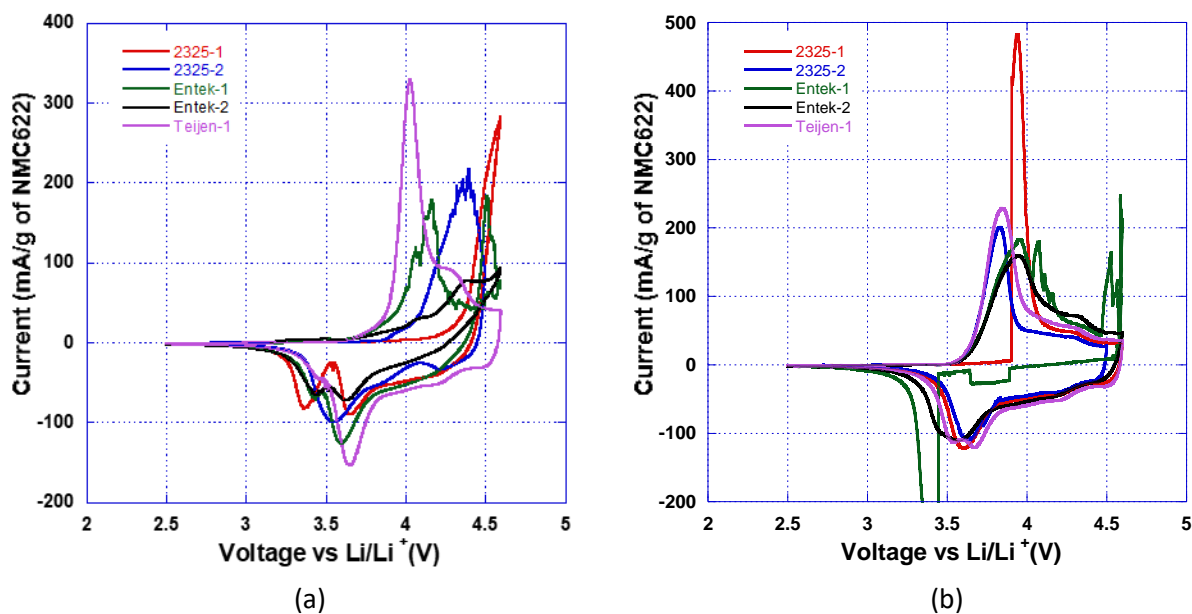


Figure 93. Comparison of cyclic voltammetry curves with various separators: (a) 1<sup>st</sup> cycle and (b) 4<sup>th</sup> cycle. Source: ORNL

### Morphology of Separators

SEM was used to characterize the morphology of the separators as shown in Figure 94 (a) and (b) for Entek and Teijin respectively. The ceramic coating was clearly observed with dramatic different particle size and shape.

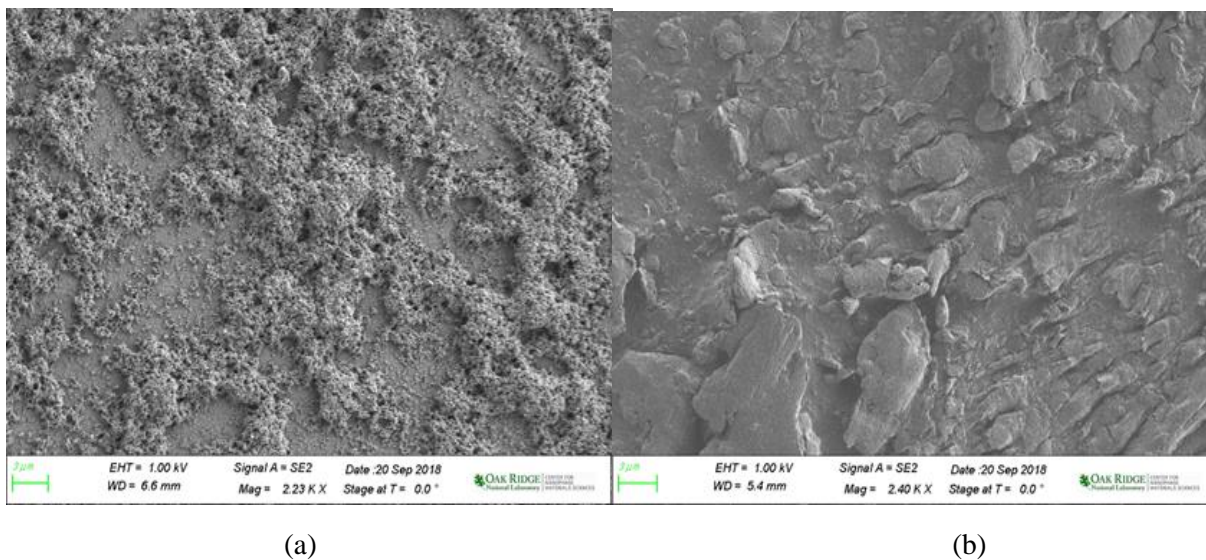
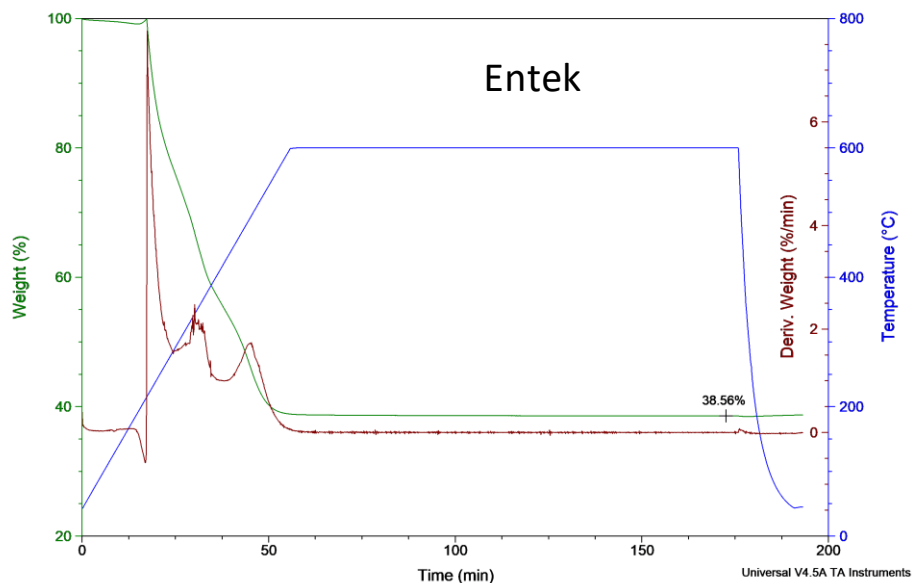


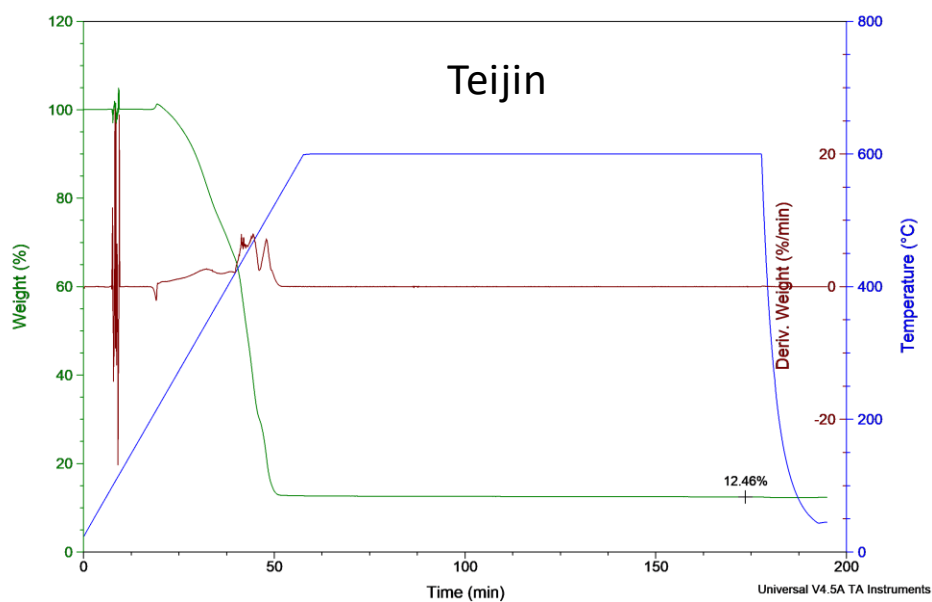
Figure 94. SEM images of (a) Entek and (b) Teijin separators. Source: ORNL

## Composition and Content of the Ceramic Coating

Thermogravimetric analysis (TGA), x-ray photoelectron spectroscopy (XPS) and FTIR were performed to determine the composition and content of the ceramic coating on the separators. The TGA experiment was performed in air from room temperature to 600°C with 10°C/min ramp rate and 2 hrs dwell time at 200°C. From the TGA results shown in Figure 95 (a) and (b), the ceramic contents were determined to be 38.56 wt% and 12.46 wt% for the Entek and Teijin, respectively.



(a)



(b)

Figure 95. Ceramic contents were determined from TGA experiment at (a) 38.56 wt% for Entek and (b) 12.46 wt% for Teijin.  
Source: ORNL

The ceramic composition was characterized by XPS on the separator samples and energy-dispersive x-ray spectroscopy on the powder left from TGA experiment. As shown in Figure 96 (a) and (b) and Figure 97 (a) and (b), the ceramics were determined to be  $\text{Al}_2\text{O}_3$  and  $\text{MgO}$  for Entek and Teijin, respectively. The fluorine is most likely from binder which was confirmed from the FTIR results as shown in Figure 98. They are a good match for a fluorocarbon like PVDF. Teijin has strong -OH absorption around  $3700\text{ cm}^{-1}$ . Broad absorbance below  $1000\text{ cm}^{-1}$  could come from metal oxides.

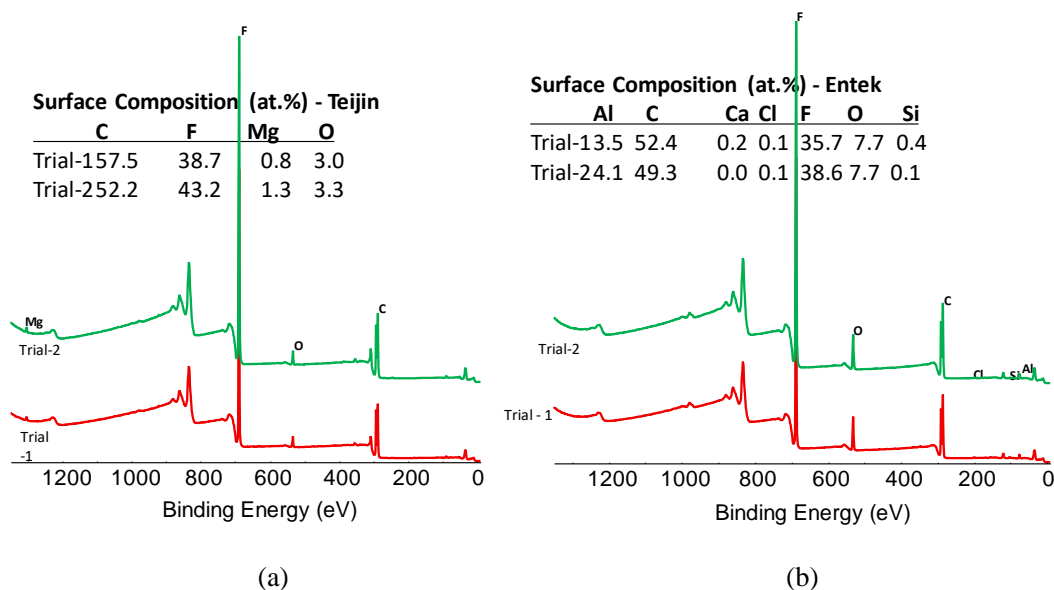
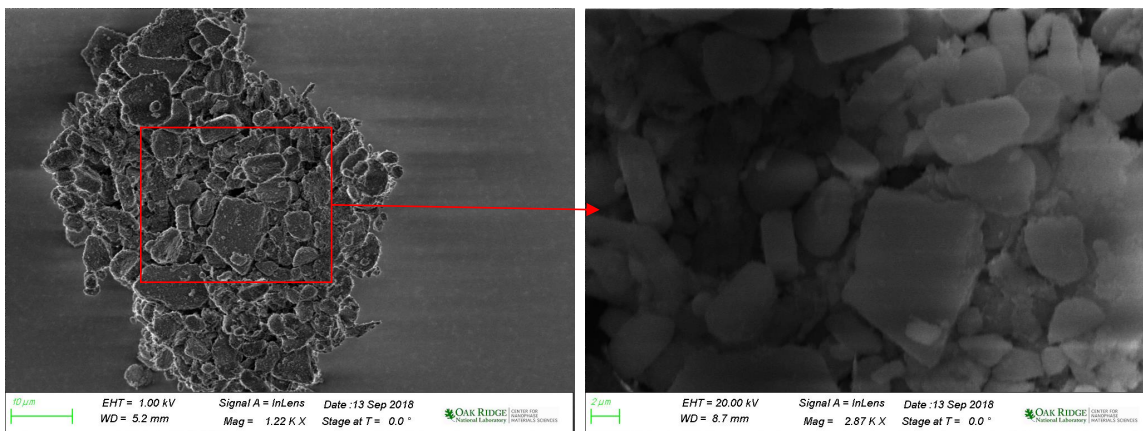


Figure 96. XPS results for (a) Teijin and (b) Entek separators. Source: ORNL

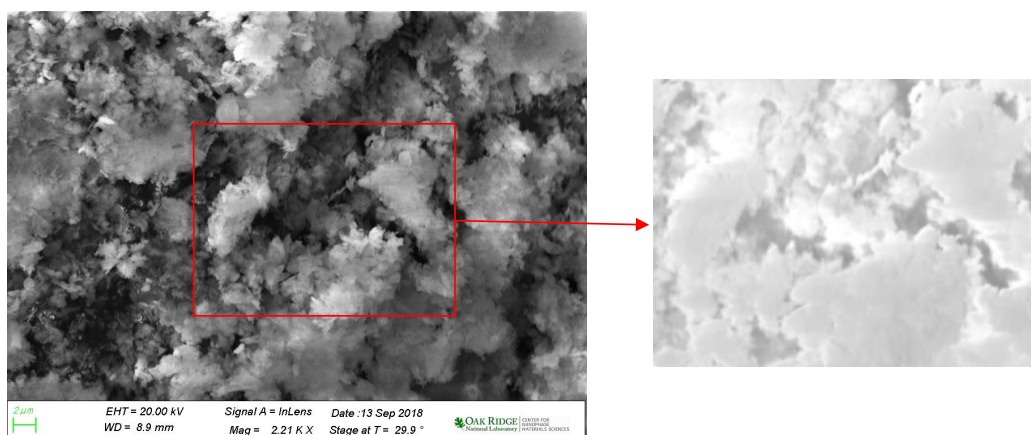


Entek

Element	Series	unn. C [wt.%]	norm. C [wt.%]	Atom. C [at.%]	Error (1 Sigma) [wt.%]
Carbon	K-series	3.95	4.74	7.81	2.42
Oxygen	K-series	36.92	44.25	54.75	6.61
Aluminium	K-series	42.58	51.02	37.44	2.15
Total:		83.45	100.00	100.00	

(a)





Teijin

Element	Series	unn. C [wt.%]	norm. C [wt.%]	Atom. C [at.%]	Error (1 Sigma) [wt.%]
Carbon	K-series	8.43	7.08	11.12	2.28
Oxygen	K-series	27.39	23.01	27.13	4.08
Fluorine	K-series	41.09	34.52	34.28	5.87
Magnesium	K-series	42.12	35.39	27.47	2.37
-----					
Total:		119.04	100.00	100.00	

(b)

Figure 97. Energy-dispersive x-ray spectroscopy results on the powder left from TGA experiments to determine ceramic composition for (a) Entek and (b) Teijin. Source: ORNL

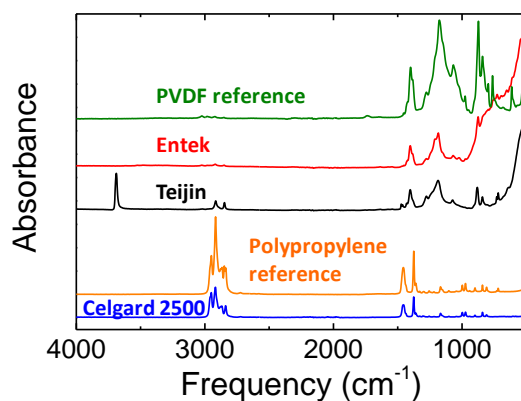


Figure 98. Binder was determined to be PVDF by FTIR. Source: ORNL

#### Electrolyte Wettability Evaluated by Contact Angle Measurements

Water and Gen II electrolyte (1.2 M LiPF<sub>6</sub> in EC/EMC, 3/7 wt) were used to collect contact angle measurements of Entek and Teijin. Given the hydrophobic nature of the samples, the water droplets stuck to the surface while the electrolyte droplet was rapidly consumed. This called for two different measurement approaches; the five water droplets were collected and measured on the surface of the



separator, while one droplet of electrolyte was dropped on the surface and images were rapidly taken at a rate of 0.1 s<sup>-1</sup>. As shown in Figure 99 (a), the average of the contact angles with water for Teijin sample (110.6°) was slightly less than that of the Entek sample (115.0°) (Figure 99 (b)). When switching to Gen II electrolyte, the contact angles were 22.5° and 9.5° for Teijin and Entek, respectively.

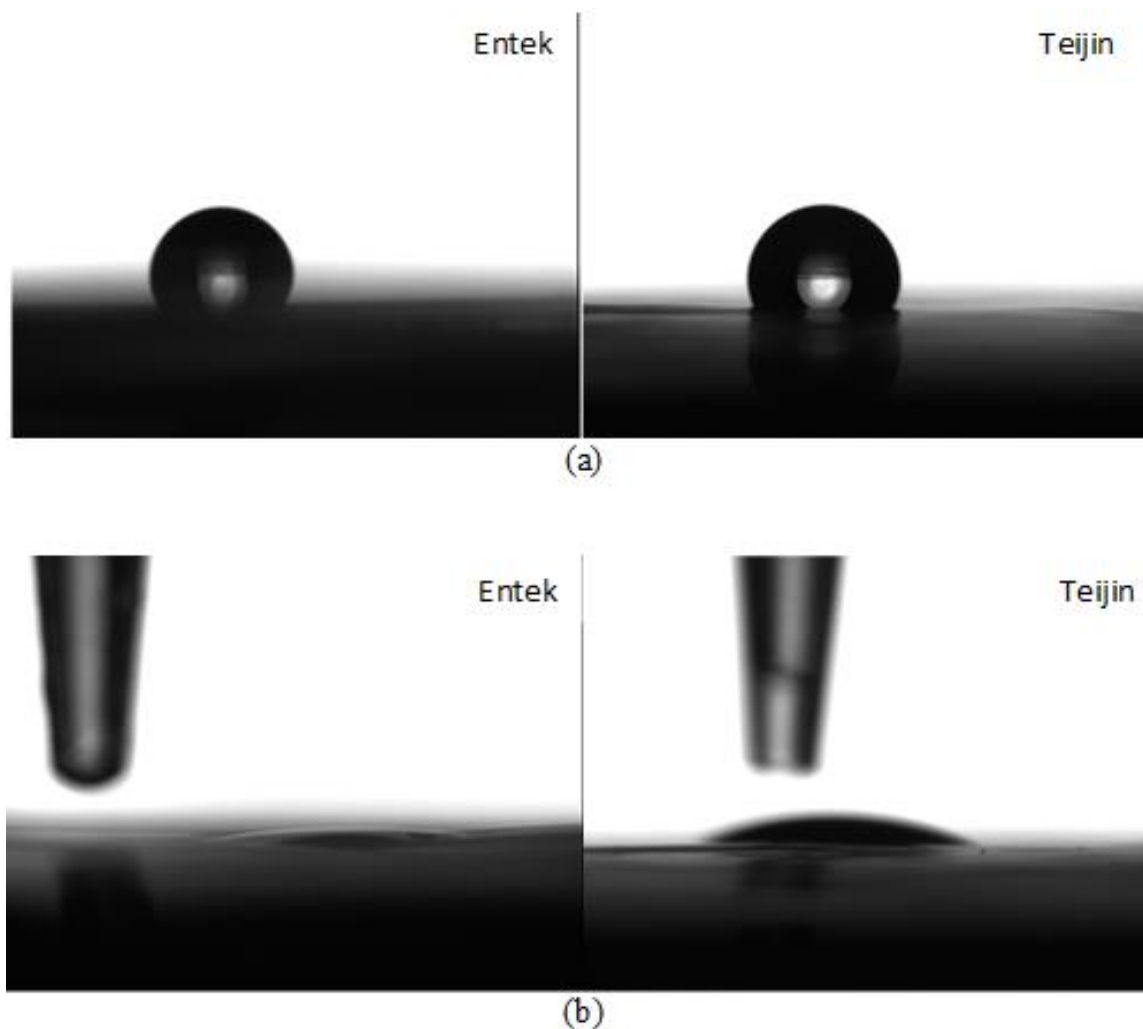


Figure 99. Contact angles (a) with water and (b) with Gen II electrolyte for Entek and Teijin. Source: ORNL

### Electrolyte Uptake

Electrolyte uptake was characterized by thoroughly soaking the separator in Gen II electrolyte for one hour. The mass of the separators was measured before and after electrolyte exposure. Electrolyte uptake was presented in three ways: 1) mass percentage (%) where the absorbed electrolyte mass was normalized by the mass of separators; 2) volumetric weight (g/cm<sup>3</sup>) where the absorbed electrolyte mass was normalized by the volume of separators prior to electrolyte exposure; and 3) volume ratio where the absorbed electrolyte volume was normalized by the volume of separators prior to electrolyte exposure. As shown in Figure 100, both separators demonstrate significant electrolyte uptake, especially for Teijin.

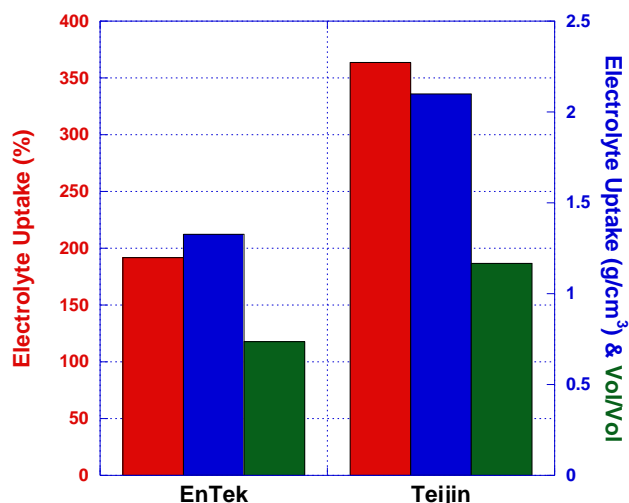


Figure 100. Electrolyte uptake of EnTek and Teijin separators with Gen II electrolyte and one-hour exposure. Source: ORNL

### Thermal Stability

Separator samples were placed on a baking dish and placed in an evacuated oven with various temperatures and dwell times. Dimensional change was defined as the change in separator area divided by the area prior to heat treatment. As shown in Figure 101(a), the Entek separator showed outstanding thermal stability and little shrinkage when exposed to 200°C for 20 min. It was stable even at 225°C for 35 min. Teijin separator also demonstrated very good thermal stability although much lower when compared to the Entek (Figure 101(b)). There seems a transition temperature between 140°C and 160°C. When looking into more details, the shrinkage started at 5 min and 160°C.

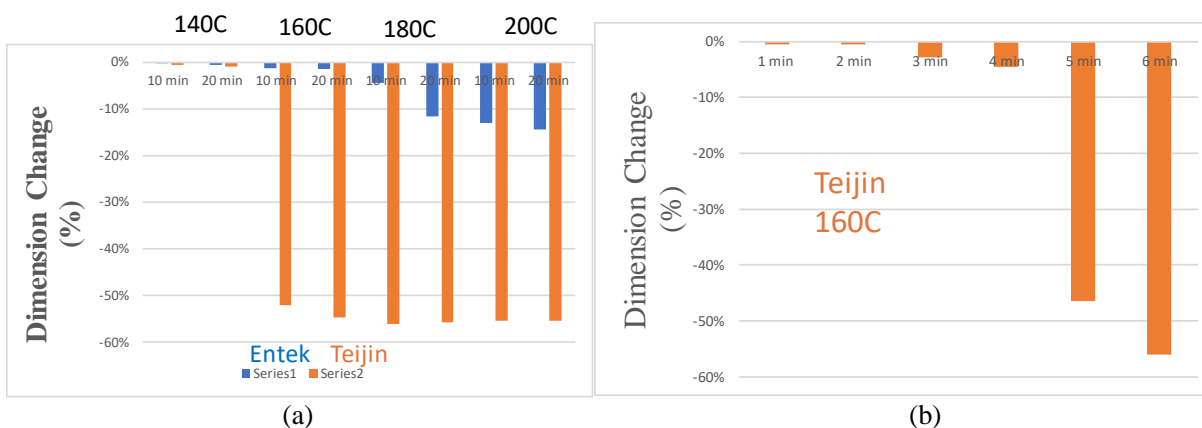


Figure 101. Dimension changes of the separators over temperatures for (a) Entek-Teijin comparison and (b) Teijin at 160°C. Source: ORNL

### SolarWindow Technologies, Inc.

SolarWindow Technologies, Inc. has partnered with NREL and ANL to demonstrate diffractive multiplexing for high-throughput R2R laser patterning of flexible organic PV modules. NREL worked closely with SWT to move the project forward through several correspondences and teleconferences in addition to SWT visiting NREL to discuss the project status and near- and long-term planning.

For the optics part of this project we are working with HOLO/OR, a custom optics design and fabrication company, and consulting with HOLO/OR to aid with the design of our diffractive optical element (DOE) system, which will multiplex the laser into many lines for simultaneous materials processing.

The project is comprised of the following four tasks:

Task 1: Select a R2R AMM DOE Laboratory Collaboration Webline

Task 2: Design a Diffractive Optics-based Laser (DOL) Multiplexing Scribing Station

Task 3: Select/Design the Diffractive Optical Elements (DOE)

Task 4: Fabricate DOL Multiplexing Scribing Station

Progress in FY 2018 for each task is discussed below.

Select a R2R AMM DOE Laboratory Collaboration Webline

The NREL R2R metrology line was selected as the system for integration of the R2R multiplex scribing technology in the third quarter of FY 2018. Figure 102 shows the part of this web-line and the proposed locations of the laser system and the area on the web line where materials processing/scribing will occur.

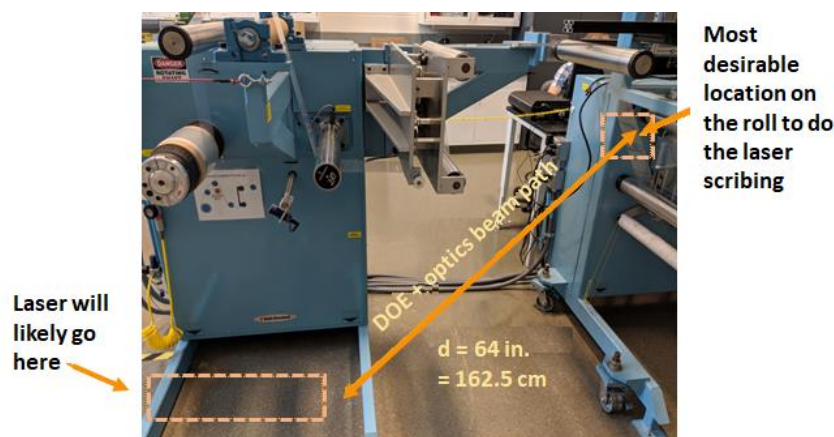


Figure 102. NREL R2R metrology line with planned location for the laser system. Source: NREL

The design for the multiplex scribing station occurred early in the project. ANL will analyze samples once the system is operational. Some additional scribing experiments were performed with the three-spot optical element and ANL performed some advanced characterization on those samples. This aided in determining the best characterization steps needed for the samples that will ultimately be created with the fully operational R2R multiplexing scribing station.

Design a Diffractive Optics-based Laser (DOL) Multiplexing Scribing Station

Discussions were held with NREL's Environmental Health and Safety team to ensure that all required safety precautions are included in the final design. As part of the design phase, possible components were tested to determine the best operational procedure. Design of the scribing station is dependent on the final DOE component design as described in Task 3 below.

Select/Design the DOE

A three-spot beam splitting element was acquired from HOLO/OR and initial tests were performed on the laser scribing system located in one of the processing glove boxes from the atmospheric processing platform in the

Process Development and Integration Laboratory. The HOLO/OR DOE was successfully tested and could split a laser beam in three equal intensity beams and scribe one of the materials that is being considered for scribing. The test showed that the DOE worked according to specifications and it was successfully used to demonstrate three parallel scribes on a coated rigid substrate in our single scribe system. To design the final optics for the multi-beam scribe for the web system, we enlisted the help of HOLO/OR to evaluate various DOL multiplexing designs. A feasibility study from HOLO/OR commenced in September 2018 and was completed in FY 2018. In their initial report, HOLO/OR compared three conceptual options for the optical design of a telecentric solution for material processing with multiple beams split by a diffractive beam splitter. Each concept adhered to our specified parameters of having multiple, focused (355 nm wavelength) laser beam spots at our sample plane, with a separation distance of 10 cm between each spot, as well as less than 15% uniformity contrast between spots. The report included a comparison of different optical approaches as shown in Table XVII with the positives and negatives of each design with regards to such characteristics as design elements, alignment complexity, uniformity, and overall cost.

**Table XVII. Comparison of Different Optical Approaches for Beam Splitting**

Feature	Simplest Model	Enhanced Model	Mirrors Model
Key Element	No	DOE Expander	Mirrors
Common Elements	Spherical Lens Array		
Special Element(s)	Collimation Lens	Beam Expander, DOE Expander, Collimating Lens	Mirrors
Alignment Complexity	Simple	Complex	Most Complex
Estimated Cost For Optical Elements	Lowest	Highest	Average
Estimated Cost For Mechanical Parts	Lowest	Average	Highest (Mirrors Alignment)
Uniformity Between Spots 13 Spots/ 14 Spots	< 15 % / 5 %	< 5 % / 3 %	< 15 % / 5 %
Zeroth Order Relative To Average Of Others 13 Spots/ 14 Spots	50-170 % / 15 %	80-120 % / 10 %	50-170 % / 15 %
Efficiency	Highest	Lower	Highest
Option To Add Top Hat Functionality Potential	Highest	Lowest (Optical Aberrations)	Average
Optical Aberrations	Low	Many	Low
Telecentricity	Good	Good	Best

Legend: Good Fair Poor

After deliberations with SWT and HOLO/OR, NREL decided to focus on the “Simplest Model”. HOLO/OR will evaluate and optimize the DOL multiplexing design with “real” optical components. Testing will continue for this element and for the other materials that need scribing. NREL will continue working with HOLO/OR to determine the best optic element for a 25+ spot beam splitter for the R2R system.

#### Fabricate DOL Multiplexing Scribing Station

Fabrication for the multiplexing scribing station will begin immediately after the completion and acceptance of the design. The design of the DOE optics is currently the “bottleneck” for moving forward. A working design

has been identified but fabrication is awaiting analysis and optimization. Once the DOE design is completed, we can move forward with fabrication of the supporting structures, e.g., scribing station and laser safety enclosures.

### **Proton OnSite**

This CRADA project had not been initiated at the end of FY 2018. Progress toward the CRADA execution included defining the following four tasks:

Task 1: Perform Electrode Ink Development and Characterization

Task 2: Demonstrate Direct R2R Coating of Electrode Ink onto Selected Membrane.

Task 3: Perform In Situ Testing of MEAs with Direct-coated Electrodes (Proton)

Task 4: Perform QC Development for the Direct-coated Electrodes

Coordination of efforts with researchers, technology transfer and business contacts at NREL, ORNL, ANL, and Proton OnSite continued on the detailed CRADA project workplan, which was approved by AMO and FCTO (including an external review for the latter). The detailed workplan was incorporated into a joint work statement and integrated into the overall multi-lab collaboration CRADA document. This document has been provided to all parties for laboratory, company, and DOE field office signatures. Also, as Proton has recently been purchased by a foreign company, additional DOE foreign engagement forms have been completed for this aspect of the DOE review.

## **Workforce Development/Educational Outreach**

The consortium expanded its workforce development and educational outreach efforts in FY 2018.

ANL supported Firat Cetinbas, a University of Delaware PhD student with experience in modeling and optimization of the PEMFC catalyst layers, to work on the Fuel Cell project.

At ORNL, Anand Parejiya, a University of Tennessee Bredesen Center PhD student, worked on the Fuel Cell project approximately 50% time.

NREL supported one undergraduate intern, one graduate intern, and two post-doctoral researchers in part via this activity during FY 2018.

At LBNL, post-doctoral researcher Fuduo Ma completed his post-doctoral training and was hired by PPG Paints. Project scientist Kenny Higa joined the project in Q3 to complete FY 2018 tasks and to begin FY 2019 planning.

## **Challenges/Contingencies**

Although all efforts for FY 2018 were completed, there were some areas identified where further research and development is needed.

The FY 2018 efforts for structured electrode materials concluded that, when a simple particle-size modification was made with an emphasis on materials processing and coating deposition methodology, substantial improvements were realized in rated capacity discharge rates. There have been several studies over the past

four years that have provided different results for determining if size grading in structured electrodes can boost performance. Since both particle sizing and porosity play an important role in electrode fabrication, more research is needed to achieve higher rated capacities over those obtained in the FY 2018 study.

The fuel cell study, as originally envisioned and planned, the FY 2018 efforts were not completed and were not intended to be completed in FY 2018. Work at NREL ceased due to lack of funding; however, all FY 2018 milestones were addressed. The major focus for future research is recommended for investigating the physics, methodologies, and equipment for multi-layer coatings as they relate to continuous processing with potential applications in fuel cells.

For functional materials, the AMO-funded project was completed in FY 2018; however, development of similar computational models to understand the synthesis of NMC cathode particles will be continued with other research opportunities.

The AMO-funded project for R2R water membranes was completed in FY 2018. A successful fabrication of stable resin wafers using a liquid ionomer binder using a semi-automated assembly manufacturing process provided a transformational improvement for R2R manufacture of the material for water purification and desalination applications. If funding were made available, a full-scale automated assembly line for R2R manufacture of resin wafers for water applications can be developed.

For modeling and simulation of slurries, the AMO funded project for battery materials was redirected to address fuel cells. In the high shear-rate regime, variation of the effective aggregate volume fraction in the battery model should explain the dependence of viscosity on shear rate. The microrheological model used as a basis for the battery model proposes a relationship to calculate this volume fraction. However, this form cannot produce the observed viscosity behavior. Further efforts should focus on revising the hydrodynamic sub-model used in the battery model to describe the fuel cell inks, which will require incorporating new theory.

For the data mining and machine learning, machine reading can accurately accomplish where the synthesis is described in a paper. Further improvements in the machine learning model could be achieved by determining what specific reactions go with each data set, developing a larger dataset on synthesis of oxide materials that would be accessible online, providing an interactive map which overviews how multiple materials can be synthesized, and developing predictive algorithms for synthesis of novel cathode materials or compositionally-modified existing cathode materials.

## **Risks and Risk Handling**

At the beginning of FY 2018, some risks were identified for two of the projects. For the Fuel Cell Study, the electrode porosity diagnostic will not be sensitive to relevant variations in anode properties (as opposed to the sensitivity we have demonstrated for cathode properties), and the concepts for phase-segregation to enable a single-layer electrode coating with an ionomer-rich surface layer will not be successful. For the R2R Water Membranes project, the commissioning of the SAAL that involves multiple steps of unit operation will be delayed because of dispenser issues that could affect the process and result in damaging the quality of the porous resin wafer material. All risks were mitigated during FY 2018.

## **Project Ratings**

Project performance assessments are determined through quantitative and qualitative methods in accordance with DOE O 413.3B Program and Project Management for the Acquisition of Capital Assets. Programs are assessed by definitions: green – project is expected to meet its current performance baseline; yellow – project is potentially at risk of not meeting an element of the current performance baseline; red – project is highly at



risk of requiring a change to the performance baseline by the Acquisition Executive or is not being executed within the acquisition strategy and Project Execution Plan.

Table XX provides an overview of project performance for each of the Consortium laboratories and for the overall project at the end of FY 201.

**Table XVIII. R2R AMM Laboratory Consortium Project Ratings**

**ANL**

Key Performance Indicator	Rating (red/green/yellow)	Status/Corrective Action
Performance	●	All performance targets are being met.
Cost	●	Project cost was within FY 2018 budget.
Schedule	●	All tasks and milestones were met on schedule.

**ORNL**

Key Performance Indicator	Rating (red/green/yellow)	Status/Corrective Action
Performance	●	All performance targets are being met.
Cost	●	Project cost was within FY 2018 budget.
Schedule	●	All tasks and milestones were met on schedule.




**NREL**

Key Performance Indicator	Rating (red/green/yellow)	Status/Corrective Action
Performance	●	All performance targets are being met.
Cost	●	Project cost was within FY 2018 budget.
Schedule	●	All tasks and milestones were met on schedule.

**LBNL**

Key Performance Indicator	Rating (red/green/yellow)	Status/Corrective Action
Performance	●	All performance targets are being met.
Cost	●	Project cost was within FY 2018 budget with carryover.
Schedule	●	All tasks and milestones were met on schedule.

## OVERALL PROJECT

Key Performance Indicator	Rating (red/green/yellow)	Status/Corrective Action
Performance		All performance targets are being met.
Cost		Project cost was within FY 2018 budget.
Schedule		All tasks and milestones were met on schedule.

## Conclusions

For structured electrodes, substantial improvements were realized in rated capacity at 2C discharge rates when a simple particle-size modification was made and combined with a thick (4 mAh/cm<sup>2</sup>) bilayer approach, with an emphasis on materials processing and coating deposition methodology (dual slot-die and dual-pass). This technology enables simultaneous high energy and power density. The best overall combination was the all small particle baseline cathode with the mixed particle anode, which showed 82% capacity retention after 950 cycles. Interestingly, the mixed particle cathode with the dual-pass anode containing small particles on the bottom also showed very good capacity retention (83% after 830 cycles), even though it was not one of the top performing combinations in the rate performance testing.

In the fuel cell study, it was demonstrated that IRS GDEs fabricated with a R2R process showed the same trends as earlier fabricated Mayer-rod electrodes. R2R fabricated electrodes without additional ionomer overlayer produced equivalent mass activity to spray-coated electrodes with an ionomer overlayer. Oxygen-limiting current measurements can be utilized to elucidate oxygen mass transport, which can be further optimized. The solvent alcohol to water ratio can be tuned to control ionomer distribution. Certain alcohols can be used to significantly reduce the ionomer needed to achieve baseline mass activity. Water-rich solvents produce a more dispersed ink which results in better high-current density performance. The improved high current-density performance is due to a lower non-Fickian resistance for oxygen transport measured in limiting current measurements. NREL developed, licensed and published an Open Source Impedance Fitter (OSIF), which assists the community in electrochemical impedance analysis. The software provides a graphics-based tool to allow the user to fit impedance spectra from PEMFCs to a commonly accepted model. The benefit over other available tools is expanded flexibility and ease of use.

In the modeling of slurries, it was concluded that colloidal interactions largely determine the rheological properties of the battery slurries. A combination of attractive and repulsive interactions leads to a secondary minimum of potential energy. The particle pair interaction potential is used to represent all particle-particle interactions connected to effective slurry viscosity. These include steric (elastic and osmotic) and Van der Waals forces. Both polymer brush length and fractal dimension were used as fitting parameters for the microrheological model of a whole slurry. The model that was developed suggests that PEM elongation and aggregate morphology reasonably explain carbon black slurry viscosity. Full electrode slurry with graphite particles can be reasonably modeled as graphite particles in a carbon black network.

Machine reading can accurately accomplish where the synthesis is described in a paper; the type of synthesis method, e.g. solid state synthesis, hydrothermal, sol-gel, thin film deposition, etc.; precursors (reagents) used in the reaction; the target of the synthesis; and the conditions of the synthesis (e.g. firing temperature, atmosphere, etc.) The major product for this effort was the preparation of the dataset of reactions for public release.

Research in functional materials demonstrated that, even though synthesis of cathode active particles involves two steps, namely coprecipitation and calcination, size of the secondary particles is actually determined during the coprecipitation step. Both experimental and computational analysis reveals that dynamics of particle growth involves two steps, where the first one is limited by reaction kinetics, and transport processes control the second step. Along with nucleation, growth and aggregation of the primary and secondary particles, breakage of secondary particles because of fluid shear-induced force must also be considered. Particles with a larger size and lower aspect ratio are prone to rupture. Formation of a dense distribution of primary particles can be attributed to the calcination step where sintering of the secondary particle helps to remove pores. Presence of a few internal pores can be explained from the distribution of primary particles after coprecipitation and sintering process.

Resin wafer technology is capable of providing greater than 35 % energy efficiency for water desalination compared to 15 % for the current state-of-the-art technologies. RW-EDI technology was demonstrated in a pilot-scale R2R semi-automated assembly line. Experiments confirmed that wafers fabricated with this continuous process were as efficient for water separation applications as wafers made from a manual hot-press method. Application of this advanced manufacturing technology has the potential to improve separation energy efficiency and processing costs (95% for labor and 90% production time) for multiple industrial sectors.

## Key Publications

Barai, P., Feng, Z., Kondo, H., Srinivasan, V. “Simplified Computational Model for Evolution of Particle Morphology during Co-precipitation.” Presented at Electro Chemical Society 2018 Spring Meeting, Seattle, WA May 13 – 17, 2018.

Barai, P., Feng, Z., Kondo, H., Srinivasan, V. “Multiscale Computational Model for Particle Size Evolution during Coprecipitation of Li-ion Battery Cathode Precursors.” Submitted for publication to *Journal of Physical Chemistry B* (in review).

Feng, Z., Barai, P., Gim, J., Yuan, K., Wu, Y.A., Xie, Y., Liu, Y., Srinivasan, V. “In Situ Monitoring of the Growth of Nickel, Manganese, and Cobalt Hydroxide Precursors during Co-Precipitation Synthesis of Li-Ion Cathode Materials.” *Journal of The Electrochemical Society*, **165** (13) A3077-A3083 (2018)

Feng, Z., Barai, P., Gim, J., Ge, L., Gao, H., Srinivasan, V. “Evolution of Nickel, Manganese and Cobalt Hydroxide Precursor for Li-Ion Battery Cathode Materials in Co-precipitation Reactions.” Presented at the Electro Chemical Society 2018 Spring Meeting, Seattle, WA May 13 – 17, 2018.

Khandavalli S., Stickel J., Hurst K., Kariuki N.N., Park J.H., Myers D.J., Neyerlin K.C., Ulsh M.J., Mauger S.A. “Rheological investigation of catalyst inks for roll-to-roll processing of fuel cell electrodes.” Poster presentation at the Fuel Cells Gordon Research Conference; July 2018.

Khandavalli S., Stickel J.J., Hurst K., Kariuki N.N., Park J.H., Myers D.J., Neyerlin K.C., Ulsh M., Mauger S.A. “Rheological investigation of catalyst inks for roll-to-roll processing of fuel cell electrodes.” oral presentation at the International Symposium of Coating Science and Technology, Long Beach, CA; September 2018.

Khandavalli S., Park J.H., Kariuki N.N., Myers D.J., Stickel J.J., Hurst K., Neyerlin K.C., Ulsh M., Mauger S.A. “Rheological investigation of fuel cell catalyst inks.” Presentation at the Society of Rheology meeting, Houston, TX; October 2018.

Mauger, S.A., Cetinbas C.F., Park J.H., Neyerlin K.C., Ahluwalia R.K., Myers D.J., Khandavalli S., Hu L., Litster S., Ulsh M. “Control of ionomer distribution and porosity in roll-to-roll coated fuel cell catalyst layers.” Poster presentation at the Fuel Cells Gordon Research Conference; July 2018.

Mauger S.A., Cetinbas C.F., Ahluwalia R.K., Myers D.J., Park J., Neyerlin K.C., Hu L., Litster S., Ulsh M. “Control of ionomer distribution and porosity in roll-to-roll coated fuel cell catalyst layers.” oral presentation at the International Symposium of Coating Science and Technology, Long Beach, CA; September 2018.

Park, J., N. Kariuki, D. J. Myers, S. A. Mauger, K. C. Neyerlin, and M. Ulsh, “In Situ X-Ray Scattering Characterization of PEMFC Catalyst Ink Microstructure during Ink Processing”, 233rd ECS Meeting, 2018, MA2018-01 1794.

Rupnowski, P., M. Ulsh, B. Sopori, B.G. Green, D.L. Wood III, J. Li, Y. Sheng. “In-line monitoring of Li-ion battery electrode porosity and areal loading using active thermal scanning – modeling and initial experiment.” *J. Power Sources*, 375, p.138-148, 2018.

Wood, D.L. III, Wood, M., Li, J. Du, Z., Daniel, C., Dunlop, A., Polzin, B., Jansen, A.; Krumdick, G., Rupnowski, P., Ulsh, M.; Ma, F., Battaglia, V. Prasher, R. “AMO R2R Advanced Materials Manufacturing (AMM) Consortium and Structured Electrodes for Lithium-Ion Batteries.” 19th International Coating Science and Technology Symposium, Abstract No. ISCST- 20180917AM-AB-PL1, Long Beach, California, September 16-19, 2018.

Wood, D.L. III, Wood, M., Du, Z., Li, J. “Electrode Structuring and Processing Challenges of Advanced Lithium Secondary Batteries with Ultra-High Energy Densities.” Beyond Lithium-Ion XI, Cleveland, OH, July 26, 2018.

Wood, D.L. III, Wood, M. Li, J., Du, Z., Smyrek, P., Zheng, Y., Rakebrandt, J-H., Pfleging, W., Rao, R., Solberg, S. “Novel R2R Manufacturing Approaches for Lithium Ion Battery Electrodes.” 2018 ASME Power and Energy Conference and Exhibition, Orlando, Florida, June 28, 2018.

## References

1. Howell, D. “Vehicle Technologies Office Electrochemical Energy Storage R&D Overview”. (2017), The 2017 U.S. Department of Energy (DOE) Fuel Cell Technologies Office (FCTO) and Vehicle Technologies Office (VTO) Annual Merit Review and Peer Evaluation Meeting (AMR), Washington, DC, June 6, 2017. [https://www.energy.gov/sites/prod/files/2017/06/f34/es000\\_howell\\_2017\\_o.pdf](https://www.energy.gov/sites/prod/files/2017/06/f34/es000_howell_2017_o.pdf)
2. Garland, N. “Manufacturing R&D Program Area - Plenary Presentation”. (2017), The 2017 U.S. Department of Energy (DOE) Fuel Cell Technologies Office (FCTO) and Vehicle Technologies Office (VTO) Annual Merit Review and Peer Evaluation Meeting (AMR), Washington, DC, June 6, 2017. [https://www.hydrogen.energy.gov/pdfs/review17/mn000\\_garland\\_2017\\_o.pdf](https://www.hydrogen.energy.gov/pdfs/review17/mn000_garland_2017_o.pdf)
3. Macknick, J.; Newmark, R.; Heath, G.; Hallett, KC. “A Review of Operational Water Consumption and Withdrawal Factors for Electricity Generating Technologies”. (2011) Technical Report NREL/TP-6A20-50900, March 2011. <https://www.nrel.gov/docs/fy11osti/50900.pdf>
4. Chockalingam et al. (Comput. Methods Appl. Mech. Engrg. 312 (2016) 492–508)
5. The Battery University, BU-402: What Is C-rate. [http://www.batteryuniversity.com/learn/article/what\\_is\\_the\\_c\\_rate](http://www.batteryuniversity.com/learn/article/what_is_the_c_rate)
6. Wikipedia – Calendering, [www.en.wikipedia.org/wiki/Calendering](http://www.en.wikipedia.org/wiki/Calendering)
7. The Free Dictionary. [www.encyclopedia2.thefreedictionary.com/Coin+cell](http://www.encyclopedia2.thefreedictionary.com/Coin+cell)
8. ITW Dynatec® <https://www.itwdynatec.com/products/adhesive-applicators/slot-die-applicators/twincoat-non-contact-dual-slot-die>
9. FreedomCAR Battery Test Manual For Power-Assist Hybrid Electric Vehicles, U.S. Department of Energy, Energy Efficiency and Renewable Energy, Idaho Operations Office, October 2003.

10. "A Simple Way to Make Lithium ion Battery Electrodes that Protect Themselves" SLAC Press Release on January 11, 2016. <https://www6.slac.stanford.edu/news/2016-01-11-simple-way-make-lithium-ion-battery-electrodes-protect-themselves.aspx>
11. HMKTest® website. [www.aimsizer.com/faqs-What-is-D50.html](http://www.aimsizer.com/faqs-What-is-D50.html)
12. Lastoskie, C; Keith E. Gubbins, K.E.; Quirk, N. 1993. "Pore Size Distribution Analysis of Microporous Carbons: A Density Functional Theory Approach." J. Phys. Chem., 97: 4786-4796
13. Definitions and Translations. <http://www.definitions.net/definition/porosimetry>
14. The Battery University, BU-301a: Types of Battery Cells. [http://www.batteryuniversity.com/learn/article/types\\_of\\_battery\\_cells](http://www.batteryuniversity.com/learn/article/types_of_battery_cells)
15. Wikipedia – Roll-to-Roll Processing. [https://en.wikipedia.org/wiki/Roll-to-roll\\_processing](https://en.wikipedia.org/wiki/Roll-to-roll_processing)
16. Miller, M.D. 'Slot Die Coating Technology' Extrusion Dies Industries, LLC, Chippewa Falls, WI. <https://www.pstc.org/files/public/Miller09.pdf>
17. Wikipedia – Roll-to-Roll Processing. [https://en.wikipedia.org/wiki/Roll-to-roll\\_processing](https://en.wikipedia.org/wiki/Roll-to-roll_processing)
18. Miller, M.D. 'Slot Die Coating Technology' Extrusion Dies Industries, LLC, Chippewa Falls, WI. <https://www.pstc.org/files/public/Miller09.pdf>

## Glossary

1C, 2C, C/3, C/5, C/10, C/20	Charge and discharge rates of a battery are governed by C-rates. The capacity of a battery is commonly rated at 1C, meaning that a fully charged battery rated at 1Ah should provide 1A for one hour. The same battery discharging at 0.5C should provide 500mA for two hours, and at 2C it delivers 2A for 30 minutes. Losses at fast discharges reduce the discharge time and these losses also affect charge times. [5]
Calendering	A finishing process used on cloth, paper, or plastic film. A calender is employed, usually to smooth, coat, or thin a material. [6]
Coin cell	A single-cell battery that is used to power wristwatches, computer clocks, hearing aids and other small devices. Also called a "coin cell," button cells look like small, squat silver cans from five to 25mm in diameter. [7]
Dual slot	A process that allows splitting of the required amount of material into two layers and then applying them simultaneously on a substrate. [8]
Hybrid Pulse Power Characterization (HPPC)	Test procedure whose results are used to calculate pulse power and energy capability under specific operating conditions. [9]
NMC particles	Cathodes made of nickel manganese cobalt oxide, or NMC, are an especially hot area of battery research because they can operate at the relatively high voltages needed to store a lot of energy in a very small space. [10]
Particle size distribution, D50	The value of the particle diameter at 10%, 50% and 90% in the cumulative distribution for a group of particles expressed as D10, D50, D90, etc. Particle size distribution of D50 is also known as the median diameter or the medium value of the particle size distribution, it is the value of the particle diameter at 50% in the cumulative distribution. It is one of many important parameters characterizing particle size. For example, if D50=5.8 $\mu$ m, then 50% of the particles in the sample are larger than 5.8 $\mu$ m, and 50% smaller

	than 5.8 um. D50 is usually used to represent the particle size of group of particles. [11]
Pore size distribution	The distribution of the size of the various pores in a material. The range of pore sizes is divided into the groups according to IUPAC Classification of pore sizes: macro-pore >500 Angstroms, mesopore 20 to 500 Angstroms, supermicropore 7 to 20 Angstroms, and ultra-micropore ,7 Angstroms. [12]
Porosimetry	An analytical technique used to determine various quantifiable aspects of a material's porous nature, such as pore diameter, total pore volume, surface area, and bulk and absolute densities [13]
Pouch cell	Instead of a metallic cylinder and glass-to-metal electrical feed-through, conductive foil-tabs are welded to the electrodes and brought to the outside in a fully sealed way with the end product resembling a pouch. [14]
Roll-to-roll	Any process of applying coatings, printing, or performing other processes starting with a roll of a flexible material and re-reeling after the process to create an output roll. [15]
Slot coating die	A slot coating die is a device that is capable of holding a fluid's temperature, distributing a fluid uniformly and defining a coating width. The die is comprised of steel body sections that house the fluid flow chamber. A dual slot coating die would use an upper and lower section. [16]
Weblines	During the sheet printing process, after each sheet has been printed, the press table needs to be hand-wiped to ensure the ink will not smear and ruin the printed circuit. In weblines printing, the machine has a wiper mechanism, automating the process. Using weblines printing increases production speeds and creates a more streamlined printing process. [17]
Word2vec	A group of related shallow two-layer neural network models used to produce word embeddings and trained to reconstruct linguistic contexts of words. [18]



